Université Lille 1 - Sciences et Technologies
Laboratoire de Mécanique de Lille (UMR CNRS 8107)

THESE
pour l'obtention du diplôme de

DOCTEUR
de
L'UNIVERSITE DES SCIENCES ET TECHNOLOGIES DE LILLE
Discipline : Génie-Civil

présentée par

Zheng HE

Sujet de la thèse :

Quelques contributions à la modélisation micromécanique de l'argilite du Callovo-Oxfordien

soutenue à Lille, le 11 décembre 2012
devant le jury composée de :

M. Albert Giraud	Professeur, INPL-ENSG	Rapporteur
M. Laurent Jeannin	Ingénieur de Recherche HDR, GDF-SUEZ	Rapporteur
M. Renald Brenner	Chargé de recherche CNRS 1, Université Pierre et Marie Curie	Examinateur
M. Vincent Monchiet	Maitre de conférence HDR, Université Paris-Est	Examinateur
M. Darius Seyedi	Ingénieur de Recherche, ANDRA	Examinateur
M. Jian-Fu Shao	Professeur, Université de Lille 1	Examinateur
M. Djimedo Kondo	Professeur, Université Pierre et Marie Curie	Directeur de thèse
M. Luc Dormieux	Professeur, ENPC	Co-directeur de thèse

Remerciements

Ce travail de thèse a été réalisé entre l'équipe Micromécanique et Calcul des Structures du Laboratoir Navier de l'Ecole des Ponts ParisTech et le Laboratoire de Mécanique de Lille(LML). Je souhaite donc d'abord adresser toute ma sincère reconnaissance à mes directeurs de thèse M.Djimédo Kondo et M.Luc Dormieux pour ses grandes patiences et soutiens qu'ils m'ont apportés tout au long de thèse. Ses connaissances, ses rigueurs scientifiques m'ont permis de mener à bien les différents sujets abordés dans ce mémoire. Surtout, je remercie M.Djimédo Kondo pour sa grande disponibilité et ses conseils pertinents qui ont contribué à ma formation scientifique et égalment M.Luc Dormieux pour son accueil chaleureux au sein de son équipe pour découvrir le domaine passionnant qu'est la micromécanique.

Ensuite, je voudrais exprimer ma gratitude envers M.Jian-Fu Shao pour m'avoir accueilli dans son équipe pour un stage poste d'ingenieur et pour avoir éveillé ma curiosité scientifique. Je le remercie également pour avoir participé à l'évaluation de ce travail.

Je souhaite remercier M.Albert Giraud et M.Laurant Jeannin qui ont accepté la lourde tâche d'être rapporteurs de cette thèse. Je tiens également à remercier M.Renald Brenner, M.Darius SEYEDI M.Vincent Mochiet pour avoir pris part au jury en tant qu'examinateurs. J'en profit pour remercier l'ANDRA qui a financé ce travail.

Mes remerciements s'adressent également à M.Weiya XU pour ses soutiens et ses conseils depuis mes études en master de recherche à l'Université de Hohai en Chine. Je voudrais remercier M.Eric Lemarchand, dont l'aide et les discussions m'ont été tès précieux. Je remercie également à l'ensemble de l'équipe Micromécanique et Calcul des Structures du Lavoratoire Navier et ER4 LML pour leur aide et leur amitié: Patrick, Eric, Denis, Ghazi, Sébastien, Min Tuan, Grégory, Maged, Francois, Vanh Tuan, Marie-Francoise, Shouyi Xie, Yun Jia, Jean, Wanqing Shen, Liang Yue, Anne-Marie... Un grand merci particulier à He Yang, Yun Huang, Tao Zeng pour leur amitié et leurs encouragements.

Enfin, je remercie sincèrement mes parents Yongchun HE, Yuzhu BAI et ma femme Li CHEN pour leur patience et leurs encouragements tout au long de ce travail.

Contents

Introduction

Ce travail, réalisé principalement au Laboratoire Navier et Laboratoire de Mécanique de Lille et en collaboration avec l'ANDRA (Agence nationale pour la gestion des déchets radioactifs), est lié à la problématique du stockage des déchets radioactifs à haute activité et à vie longue. La couche d'argilite du Callovo-Oxfordien a été choisie comme matériau constitutif de la barrière géologique vis à vis des radioéléments des colis de déchets.

En tant que roches argileuses dures, l'argilite du Callovo-Oxfordien est un matériau poreux multi-échelle comprenant des agrégats d'argile structurés, des phases minérales telles que le quartz, la calcite, etc et des pores. Plus précisément, deux échelles différentes peuvent être identifiées. A l'échelle dite mésoscopique, l'argilite peut être considérée comme consitituée une matrice d'argile dans laquelle des inclusions de quartz ou de silice sont noyées. La taille typique de ces inclusions minérales est de quelques dizaines de μm. A cette échelle, la matrice d'argile apparaît comme un matériau homogène. A une échelle fine, dite microscopique, la phase argileuse peut être décrite comme un matériau poreux avec des pores noyés dans une phase solide. La taille typique des pores est de quelques dizaines de nm, ce qui légitime une hypothèse de séparation d'échelles.

Dans l'objectif de formuler un modèle prédictif du comportement d'argilite, diverses recherches ont été réalisées depuis quelques années sur ces matériaux [Kaarsberg,59], [Hornby et al.,94], [Hornby,98], [Sayers,94], [Sayers,99], [Chiarelli et al.,03], [Conil et al.,03], [Ulm et al.,05], [Draege et al.,06], [Bobko08], [Abou-ChakraGuery et al.,08]. Dans une vision purement macroscopique, [Chiarelli et al.,03], [Conil et al.,03] ont développé une modélisation qui couple une plasticité cohésive-frottante et endommagement. Les modèles proposés sont capables de décrire les caractéristiques principales de l'argilite, la sensibilité de la réponse mécanique à la pression de confinement, la dilatance volumique, la dégradation des propriétés élastiques et l'anisotropie induite. Ils conduisent à de bonnes prévisions en termes de la relation macroscopique de contrainte-déformation. Cependant, ils ne sont pas en mesure de prendre en compte les mécanismes de déformation liés à des hétérogénités variables avec la profondeur sur le site au sein du matériau et en particulier sa composition minéralogique.

Pour surmonter cette difficulté, [Abou-ChakraGuery et al.,08] ont adopté une formulation incrémentale pour la modélisation d'un matériau triphasé, constitué d'inclusions minérales élastiques ou endommageables (grains de quartz, de calcite) plongés dans une matrice plastique d'argile. Une plasticité non-associée et dilatante de type Drucker-Prager a été considérée pour la matrice d'argile. Plus récemment, à plus petite échelle, l'analyse minéralogique

[Robinet,08] permis de montrer que la matrice d'argile est elle même constituée de particules d'argile et de micropores[1]. Sur la base de travaux de [Abou-ChakraGuery et al.,08] et afin de prédire de façon plus pertinente le comportement macroscopique de l'argilite (fortement sensible à la presence de micropores), [Shen et al.,12] ont proposé une procédure d'homogénéisation en deux étapes: l'homogénéisation de type 'micro-méso' à laquelle l'argile est décrite comme une phase solide de type Drucker-Prager contenant des micropores sphériques; ensuite une homogénéisation de type 'méso-macro' considérant les effets des inclusions minérales. Toutefois, ces recherches ignoront la microstructure de la matrice d'argile et en particulier des feuillets qui jouent un rôle très important dans l'anisotropie de l'argilite. La microstructure des particules argileuses sous form de feuillets a été prise en compte dans modèles élastiques indiquant l'orientation de particules solides [Hornby et al.,94] [Sayers,94] [Draege et al.,06] ou par des modèles macroscopiques décrivant l'orientation des espaces interstitiels entre des particules [Ulm et al.,05] [Bobko08]. Néanmoins, le comportement élasto-plastique n'a pas encore été modélisé dans le cadre d'une approche micromécanique.

Le point de départ de cette thèse est une tentative de formuler une description des propriétés élasto-plastiques et isotropes transverses de la matrice argileuse qui est sythetisée comme un medium granulaire comprenant des sphères composites (grains sphériques feuilletés entourés par des interfaces) et des pores. Plus concrètement, au **chapitre 1** nous nous sommes concentrés sur la modélisation de la matrice d'argile en s'appuyant sur un changement d'échelle 'micro-méso' (Voir Fig.1.1 du niveau I au niveau II) tenant compte des mécanismes de glissement plastique intragranulaire et de glissement d'interface intergranulaire. Le problème d'homogénéisation de la matrice d'argile et de phases d'inclusion du niveau supérieur (du niveau II au niveau macro) peut alors être résolu suivant la démarche developée par [Abou-ChakraGuery et al.,08] puis [Shen,11]. Cet aspect ne sera pas discuté dans mémoire de thèse.

Pour l'étude du chapitre 1, nous avons eu recours à un critère de plasticité proposée de type Tresca, Le comportement d'interface est apparu important pour améliorer la modélisation. Un certain nombre de questions scientifiques liées au probleme d'interface se sont ainsi poées. *Comment rendre compte d'une dilatance volumique dans le comportement de la matrice argileuse, alors que le modèle ne prévoit que de la contractance volumique? Puisque la matrice d'argile a une microstructure granulaire, comment établir un modèle pour matériau granulaire*

---

[1] On notera que ces micropores constituent le volume principal de pores de l'argilite [Andra,05].

tenant compte d'une interface cohésive-frottante. Les chapitre 2 et chapitre 3 traitent de ces questions.

La matrice de l'argilite étant constituée de grains en interaction le long de leurs interfaces, les propriétés mécaniques effectives sont fortement affectées par ces interfaces. Compte tenu de l'insuffisance du critère de Tresca pour expliquer le comportement des géomateriaux, on se propose d'établir un modèle de matériaux granulaires tenant compte d'une interface cohésive-frottante. A cette fin, on propose tout d'abord au **chapitre 2** un modèle poro-élastique pour les matériaux granulaires fluide-saturés avec effets d'interface imparfaite. Ce modèle est dérivé de la solution d'un problème d'Eshelby généralisé incorporant deux caractéristiques spécifiques: couches minces molles entourantes les grains rigides et la pression interstitielle dans l'espace des pores. En s'appuyant sur des résultats issus du modèle poro-élastique, on construit au **chapitre 3** dans le cadre des methodes d'homogénéisation non-linéaire, un critère de résistance macroscopique d'un milieu granulaire avec interfaces imparfaites entre des grains rigides. L'interface cohésive-frottante est caractérisée par un critère de rupture de Mohr-Coulomb et une règle d'écoulement associée.

Pour la transition 'micro-macro' complète en vue de l'application à l'argilite du Callovo-Oxfordien, au **chapitre 4**, nous proposons un modèle de prédiction de la résistance de l'argilite du Callovo-Oxfordien sous l'hypothèse que la phase solide de l'argile est un matériau de Drucker-Prager parfaitement plastique. Comme mentionné précédemment, l'argilite du Callovo-Oxfordien [Andra,05] est un matériau poreux multi-échelle (Porosité à l'échelle microscopique, inclusion à l'échelle mésoscopique). En conséquence, l'homogénéisation 'micro-macro' peut être réalisée en deux étapes. La première étape est le passage 'micro-méso' dans lequel la matrice argileuse décrite comme un matériau poreux, doit être homogénéisée. La deuxième étape traite la transition 'méso-macro' où la matrice d'argile apparaît comme un matériau homogène et les inclusions solides peuvent être considérées rigides par rapport à l'argile. On notera que pour la premieѐre étape, nous avons eu recours à des résultats d'homogénéisation non linéaire sous la forme d'un critère analytique elliptique ([Barthelemy et al.,03] [Maghous et al.,09]). Nous nous concentrons donc sur la deuxième étape. Cette question a été abordée récemment dans le cadre de l'homogénéisation non linéaire à l'aide de la méthode sécante modifiée [Shen et al.,12]. Le présent chapitre explore une approche alternative qui peut être considérée comme une extension du modèle de Gurson original. Au lieu d'une cavité sphérique entourée d'une matrice, on adopte le modèle de cellule sphère avec noyau rigide composé d'un noyau rigide sphérique entouré par la matrice homogénéisée déterminée à partir de la première étape (voir Fig. 4.2). Ainsi, au lieu d'un matériau de von Mises, la coquille est une phase compressible (voir aussi [Shen,11]). Le critère de rupture est issu de ce modèle dans le cadre de la méthode cinématique de l'analyse limite. De plus, il est important de souligner que le mécanisme de rupture retenu est susceptible d'inclure une concentration de déformation à l'interface de noyau-matrice. Il peut-être décrit mathématiquement à l'aide d'une discontinuité de vitesse.

Bibliography

[Abou-ChakraGuery et al.,08] Abou-Chakra Guery A., et al., *A micromechanical model of elastoplastic and damage behavior of a cohesive geomaterial*, International Journal of Solids and Structures **45** (2008), 1406–1429.

[Andra,05] Andra, *Referentiel du site meuse-haute marne*, (2005), Report.

[Barthelemy et al.,03] Barthelemy J.-F. and Dormieux L., *Determination du critere de rupture macroscopique d'un milieu poreux par homogeneisation non lineaire*, C.R.Mecanique., **331** (2003),271–276.

[Bobko08] Bobko,C., Ulm F-J, *The nano-mechanical morphology of shale*, Mechanics of Materials **40** (2008), 318–337.

[Chiarelli et al.,03] Chiarelli A.S., Shao J.F., Hoteit N., *Modeling of elastoplastic damage behavior of a claystone*, International Journal of Plasticity **19** (2003), 23–45.

[Conil et al.,03] Conil N., Djeran-Maigre I., Cabrillac R., Su K., *Poroplastic damage model for claystones*, Appl. Clay Sci. **26** (2004), 473–487.

[Draege et al.,06] Draege A., Jakobsen M., Johansen T.A., *Rock physics modelling of shale diagenesis*, Petroleum Geoscience **12** (2006), 49–57.

[Hill,65] Hill R., *Continuum micro-mechanics of elastoplastic polycrystals*, J. Mech. Phys. Solids **13** (1965), 89–101.

[Hornby et al.,94] Hornby B., Schwartz L.,Hudson J., *Anisotropic effective medium modeling of the elastic properties of shales*, Geophysics **59** (1994), 1570–1583.

[Hornby,98] Hornby B., *Experimental laboratory determination of the dynamic elastic properties of wet, drained shales*, Journal of Geophysical Research **103** (1998), 29945–29964.

[Kaarsberg,59] Kaarsberg E.A., *Introductory studies of natural and artificial argillaceous aggregates by sound-propagation and X-ray diffraction methods*, Journal of Geology **67** (1959), 447–472.

[Maghous et al.,09] Maghous S., Dormieux L., and Barthelemy J., *Micromechanical approach to the strength properties of frictional geomaterials*, European Journal of Mechanics A/Solids., **28** (2009), 179–188.

[Robinet,08] Robinet, J., Mineralogie, *Porosite et diffusion des solutes dans l'argilite du callovo-oxfordien de bure (meuse/haute-marne, france) de l'echelle centimetrique a micrometrique*, (2008), Phd.thesis, Universite de poitiers, France.

[Sayers,94] Sayers C.M., *The elastic anisotropy of shales*, Journal of Geophysical Research **99** (1994), 767–774.

[Sayers,99] Sayers C.M., *Stress-dependent seismic anisotropy of shales*, Geophysics **64** (1999), 93–98.

[Shen,11] W.Q. Shen, *Modelisations micro-macro du comportementmecanique des materiaux poreux ductiles: application a l'argilite du Callovo-Oxfordien*, (2011), Phd. thesis, Universite de Lille 1, France.

[Shen et al.,12] W.Q. Shen, J.F. Shao, D. Kondo, B. Gatmiri., *A micro-macro model for clayey rocks with a plastic compressible porous matrix*, International Journal of Plasticity, **36** (2012), 64–85

[Ulm et al.,05] Ulm F.-J., Constantinides, G., Delafargue, A., Abousleiman, Y.,Ewy, R., Duranti, L., McCarty, D.K., *Material invariant poromechanics properties of shales*, 3rd Biot Conference on Poromechanics (Norman, Oklahoma, USA.2005), Balkema Publishers, London, (2005), 37–644.

Chapter 1

Nonlinear homogenization of a porous polycrystal with interfaces: clay

Contents

Rappels du contenu

L'argilite est un milieu poreux complexe dont la matrice est composée d'une phase argileuse et de pores. Il comprend également des matières solides minérales, tels que le quartz et la calcite principalement. Le présent chapitre se limite à la formulation d'un modèle du comportement mécanique de la matrice argileuse poreuse. Plus précisément, il s'agit d'établir un modèle 'micro-macro' permettant d'écrire la réponse élasto-plastique et isotrope transverse en s'appuyant sur l'approche incrémentale de [Hill,65] pour l'homogénéisation non linéaire. Il convient de souligner que le modèle tient compte de la structure feuilletée des particules, de la distribution des orientations des grains, et bien entendu des interfaces au sein de l'assemblés conformément à données microstructurales disponibles micrographie en microscope électronique à balayage [Hornby et al,94] [Hornby,98] [sammartino,01] [Ulm et al.,05] (see Fig.1.2).

En effet, sur la base de ces observations de la microstructure de la matrice argileuse et l'expérience de la nanoindentation [Bobko et al.,08], un modèle morphologique est proposé qui considère que la matrice argileuse est un milieu granulaire en deux phases comprenant des sphères composites (grains sphériques feuilletés entourés par des interfaces) et des pores. Avec l'objectif de proposer une modélisation polycristalline poreuse avec des effets d'interfaces, en s'appuyant sur des travaux de [Dormieux et al.,07] [Fritsch et al.,07] [Maalej et al.,09] [Dormieux et al.,10], on se propose d'étudier dans ce chapitre la réponse élasto-plastique en considérant simultanément deux mécanismes de plasticité: les déformations plastiques des cristaux et les glissements le long des interfaces intercristallines.

A cette fin, le critère d'activation des cristaux est décrit par une loi de comportement de type Schmid. Un critére de type Tresca est utilisé pour décrire la résistance de l'interface. Dans le cadre de l'approche incrémentale, un premier modèle anisotrope est proposé en appliquant le schéma auto-cohérent classique; ce modèle ne tient pas compte de l'effet de l'interface. Ensuite, le problème d'inclusion généralisé d'Eshelby est revisité afin d'y intégrer les interfaces. Dans ce cadre, une solution originale numérique du problème d'une sphère feuilletée entourée d'une interface imparfaite est développée. Sur la base de cette solution, un deuxième modèle auto-cohérent qui considère l'évolution simultanée des deux mécanismes locaux de plasticité est développé. Enfin, des prédictions numériques de ces deux modèles sont comparées et permettent de démontrer la validité du modèle auto-cohérent proposé avec prise en compte des effects d'interface.

Les simulations numériques des essais de compression uniaxiale suggèrent que la rupture macroscopique ne peut pas être expliquée uniquement à l'aide du seul mécanisme de glissement intracristallin (feuillet sur feuillet). Néanmoins, le comportement macroscopique élasto-plastique et la rupture peuvent être prédits avec succès en les interprétant comme la conséquence d'une destruction successive des cristaux d'argile et des interface.

1.1 Introduction

Shales are complex porous media composed of pores and the plate- or sheet like structured clay mineral phases. Shales also include lots of mineral solids, such as quartz, calcite, feldspar and pyrite. To formulate a predictive constitutive model of shale to understand how shales behave mechanically, various researches have been realized in the past for this kind of materials [Kaarsberg,59], [Hornby et al,94], [Sayers,94], [Hornby,98], [Sayers,99], [Chiarelli et al.,03], [Conil et al,03], [Ulm et al.,05], [Draege et al,06], [Abou-Chakra et al.,08], [Bobko et al.,08]. Macroscopically, [Chiarelli et al.,03], [Conil et al,03] developed a modeling approach which couples typical cohesive-frictional plasticity model and damage model. The proposed model is able to describe the main features of the shale such as non associated plastic flow, dilatancy, degradation of elastic properties and induced anisotropy, and to provide good predictions in terms of macroscopic stress-strain relations for the Callovo-Oxfordian argillites. But these models are not able to take into account deformation mechanisms related to material heterogeneities (mineralogical compositions).

To overcome this shortcoming, [Abou-Chakra et al.,08] adopt an incremental formulation for the modeling of a three-phase material which is constituted of elastic or damaged mineral inclusions (quartz and calcite grains) and a plastic clay matrix. A non-associated and dilatant Drucker-Prager plasticity is considered for the clay matrix. More recently, at smaller scale, the mineralogical analysis [Robinet,08] shows that the clay matrix is constituted of clay particles and micro-pores, and in fact these micro-pores constitutes the main pores volume of the argillite [Andra,05]. On the basis of [Abou-Chakra et al.,08], in order to predict the macroscopic behavior of argillite which is sensitive to such micro-pores, [Shen et al.,12] proposed a two-step homogenization procedure, from microscopic scale to mesoscopic scale considering a Drucker-Prager plastic solid phase containing spherical micropores, then from mesoscopic scale to macroscopic scale considering the effects of mineral inclusions. However, these multiscale researches ignored the impacts of the plate- or sheet like microstructure of clay matrix which play a very important role in the anisotropic property of shales. The plate- or sheet like structure commonly attributed to clay has been captured by models describing the orientation of these solid particles [Hornby et al,94], [Sayers,94], [Draege et al,06] or by models describing the orientation of the pore spaces between particles [Ulm et al.,05]. But anisotropic elastoplastic behaviors have been rarely modeled in the framework of a micromechanical approach.

In order to formulate an effective model describing the transversely istropic elastoplastic behavior of clay-like material, we focused on modeling the clay matrix at the micro to mesoscopic scale (See Fig.1.1 level I to level II), without consideration of the inclusion phases. The higher level (level II to level Macro) homogenization problem of clay matrix and inclusion phases may be solved in the way of [Abou-Chakra et al.,08] which will not be discussed in this paper. We consider clay matrix is composed of two-phase composite including pores and composite sphere (laminated spherical grains surrounded by interfaces). More concretely, the methodology in this paper consists in considering the pure clay matrix as a porous polycrystal. The sheet-like structured solid particles are regarded as crystals with a fixed slip plan for each. In addition, an important improvement is to capture the influence of the mechanical interaction between crystals through the interfaces. Readers are referred to the rencent litteratures concerning the predictions of effective strength of granular material taking acount of interface effects [Dormieux et al.,07], [Fritsch et al.,07], [Maalej et al.,09], [Dormieux et al.,10]. These studies are realized by using a self-consistent scheme approach including pores and composite spheres (elastic isotropic solid sphere surrounded by an elastic interface); then the effective strength criterion is predicted then by the modified secant method for which the nonlinear local behavior of each phase is described by considering a secant stiffness corresponding to an appropriate effective deformation [Berveiller et al.,79],[Tandon et al.,88],[Ponte Castaneda et al.,98].

In this research, we propose a new model to describe the macroscopic elastoplastic stress-strain behavior of clay matrix in the principle of incremental approach [Hill,65], with simultaneous evolution of two mechanisms of plasticity: intragranular slips between the sheets and intergranular slips along the interfaces. To begin with, based on the microstructures and mechanisms identified in literatures, a morphological model is synthesized in section 1.2. Then the principles of incremental approach with a self-consistent scheme to simulate the elastoplastic behavior for polycrystal without considerations of interface effects in section 1.3. Then, in this incremental approach framework, to deal with the nonlinear homogenization of polycrystalline solid with imperfect interfaces, a revisit of the generalized Eshelby problem is provided in section 1.4. Subsequently, a new Eshebly problem of laminated solid grain surrounded by imperfect interface is solved numerically. By comparing two different models which are proposed respectively in section 1.3 and 1.4, a validation of the two models is performed in section 1.5.1. Finally, the macroscopic elastoplastic stress-strain behavior is

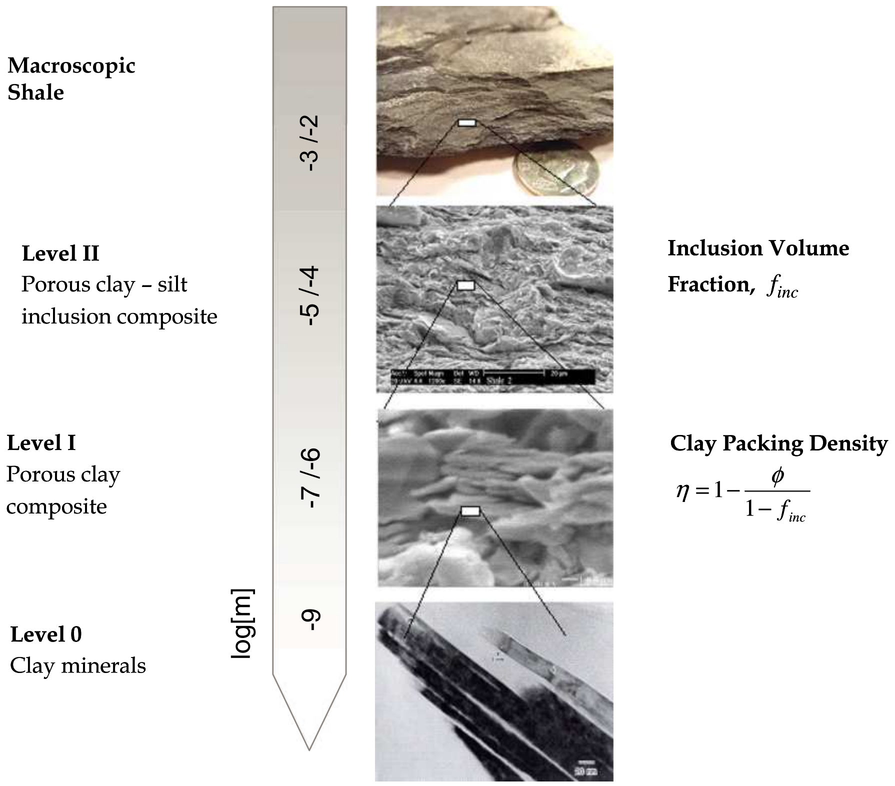

Figure 1.1: Multiscale model for shale, adapted from [Ulm et al.,05]

predicted by considering two deformation mechanisms of grain and interface which are taking place simultaneously at the microscopic scale (see section 1.5.2).

Notations: $\mathbb{J}$ and $\mathbb{K}$ the spherical and deviatoric operators, respectively. $\mathbb{J} = 1/3(\mathbf{1} \otimes \mathbf{1})$ and $\mathbb{K} = \mathbb{I} - \mathbb{J}$. The terms $\mathbf{1}$ and $\mathbb{I}$ denote the second and fourth order symmetric identity tensor, respectively.

1.2 Morphological Model

1.2.1 Morphology of clay matrix

The scanning electron microscope (SEM) microphotography imaging [Hornby et al,94], [Hornby,98],[sammartino,01],[Ulm et al.,05] shows that solid phase of clay matrix is composed by many aleatoricly distributed clay particles with disordered orientation of contact surfaces between the clay particles (see Fig.1.2). Especially based on the nanoindentation results of shale provided by [Bobko et al.,08] summarized as follows:

> by defining a so-called 'clay packing density' $\eta = 1 - \frac{f}{1-f_{inc}}$, where f is the porosity and f_{inc} is the non-clay volume fraction of shale, a percolation threshold of $\eta_0 = 0.5$ is observed in the indentation results.
>
> a so-called 'nano-mechanical elementary building block' of shales is founded transversely isotropic in stiffness, and isotropic and frictionless in strength.

a model of the porous clay morphology has been synthesized which leads to a sphere-like mechanical morphology for visibly plate- or sheet-like clay particles. Moreover, in order to take account of mechanical effects of the contact surfaces between the clay particles, it's assumed that the composite spheres of clay matrix are organized in the form of laminated spherical grains surrounded by interfaces (discontinuity of displacement) with an isotropic distribution orientation. The morphological model of clay matrix is sketched in Fig.1.3.

1.2.2 Rotated Configuration

The laminated spherical clay particles are considered as crystals. Any single crystal (or any crystal coordinate system) is related to the global coordinate system $(\underline{e}_1, \underline{e}_2, \underline{e}_3)$, in which the sheets' normal orientation is defined as $\underline{e}_r$ by using the Euler angles θ and ϕ (see Fig.1.4).

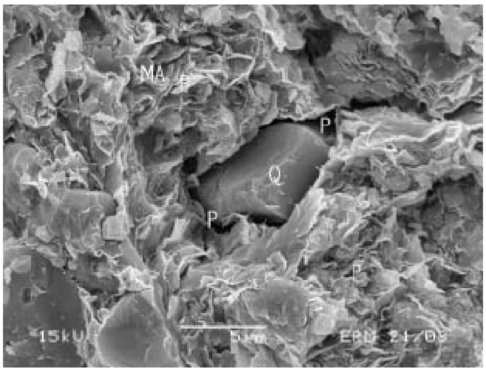

Figure 1.2: a SEM image showing the microstructure of Callovo-Oxfordian shale [sammartino,01]

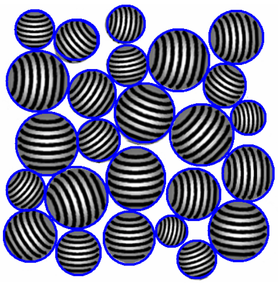

Figure 1.3: Morphological model of pure clay matrix

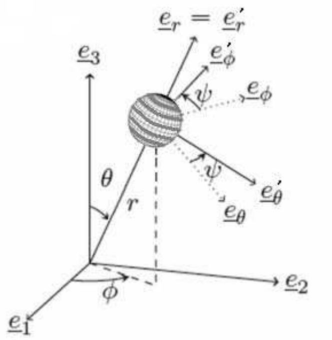

Figure 1.4: Orientation of composite sphere, defined by the direction of its axis of symmetry by means of the two Euler angles θ and ϕ (ψ is equal to zero) in the Cartesian system $O\underline{e}_1, \underline{e}_2, \underline{e}_3$

Therefore, the orientation vectors $\underline{e}_r$ and $\underline{e}_\theta$ can be expressed as:

$$\begin{aligned} \underline{e}_r &= \sin\theta\cos\phi\underline{e}_1 + \sin\theta\sin\phi\underline{e}_2 + \cos\theta\underline{e}_3 \\ \underline{e}_\theta &= \cos\theta\cos\phi\underline{e}_1 + \cos\theta\sin\phi\underline{e}_2 - \sin\theta\underline{e}_3 \end{aligned} \tag{1.1}$$

A crystal orientation matrix $Q(\theta,\phi,\psi)$ in the form of Voigt is introduced here to define the crystal (local) coordinate system with respect to the material co-rotational coordinate system (see Appendix A, [Zamiri et al.,07],[Bunge,82],[Kocks et al.,00]). According to the definitions of axes shown in Fig.1.4, the orientation matrix $Q(\theta,\phi,\psi)$ and the matrix components l_i, m_i, n_i (i=1...3) can be expressed as follows:

$$\begin{bmatrix} e_r \\ e_\theta \\ e_\phi \end{bmatrix} = Q(\theta,\phi,\psi) \begin{bmatrix} e_1 \\ e_2 \\ e_3 \end{bmatrix} \tag{1.2}$$

$$Q(\theta,\phi,\psi) = \begin{bmatrix} l_1 & m_1 & n_1 \\ l_2 & m_2 & n_2 \\ l_3 & m_3 & n_3 \end{bmatrix} = \begin{bmatrix} \cos\theta\cos\phi & \cos\theta\sin\phi & -\sin\theta \\ -\sin\theta & -\cos\theta & 0 \\ \sin\theta\cos\phi & \sin\theta\sin\phi & \cos\theta \end{bmatrix} \tag{1.3}$$

With the components l_i, m_i, n_i ($i = 1...3$) of $Q(\theta,\phi,\psi)$, another useful orientation matrix $T(\theta,\phi,\psi)$, in the form of Voigt, is defined as:

$$T(\theta,\phi,\psi) = \begin{bmatrix} l_1^2 & m_1^2 & n_1^2 & 2m_1n_1 & 2l_1n_1 & 2l_1m_1 \\ l_2^2 & m_2^2 & n_2^2 & 2m_2n_2 & 2l_2n_2 & 2l_2m_2 \\ l_3^2 & m_3^2 & n_3^2 & 2m_3n_3 & 2l_3n_3 & 2l_3m_3 \\ l_2l_3 & m_2m_3 & n_2n_3 & m_2n_3+m_3n_2 & l_2n_3+l_3n_2 & l_2m_3+l_3m_2 \\ l_1l_3 & m_1m_3 & n_1n_3 & m_1n_3+m_3n_1 & l_1n_3+l_3n_1 & l_1m_3+l_3m_1 \\ l_1l_2 & m_1m_2 & n_1n_2 & m_1n_2+m_2n_1 & l_1n_2+l_2n_1 & l_1m_2+l_2m_1 \end{bmatrix} \tag{1.4}$$

Thus, a second order tensor (stress or strain tensor) in the crystal (local) coordinate system can be transformed into the corresponding tensor in the material co-rotational (global) coordinate system by the following relation,

$$\boldsymbol{\varepsilon}(\theta,\phi,\psi)_{(\underline{e}_1,\underline{e}_2,\underline{e}_3)} = Q^T \boldsymbol{\varepsilon}_{(\underline{e}_r,\underline{e}_\theta,\underline{e}_\phi)} Q \tag{1.5}$$

So does the fourth order tensors, for example:

$$\mathbb{C}(\theta,\phi,\psi)_{(\underline{e}_1,\underline{e}_2,\underline{e}_3)} = T^{-1}\mathbb{C}_{(\underline{e}_r,\underline{e}_\theta,\underline{e}_\phi)} T \tag{1.6}$$

1.3 Plastic behavior of the polycrystal with perfect interfaces

To begin with, perfect interfaces between the single crystals constituting the polycrystal model of the clay are assumed. The plasticity mechanism is assumed to take place in the single crystals according to a Schmid-type model described hereafter.

1.3.1 Single crystal plasticity

Considering that a typically advanced mechanism to interpret the plastic behavior of clay particles is a slip between sheets at the microscopic scale, a Schmid failure criterion of single crystals is adopted. It relates the local shear stress expressed in the global coordinate system $(\underline{e}_1, \underline{e}_2, \underline{e}_3)$ to a critical stress: a slip system becomes activated once the effective shear stress reaches a critical given value on the slip system,

$$f^{(\alpha)} = \left|\tau^{(\alpha)} - \chi^{(\alpha)}\right| - \tau_{cr}^{(\alpha)} \tag{1.7}$$

where $\tau^{(\alpha)}$ and $\chi^{(\alpha)}$ represent the shear stress and back stress on αth slip system, and $\tau_{cr}^{(\alpha)}$ is the critical shear stress. To simplify our model, it's assumed that each crystal has a unique slip system; moreover, the strain hardening of the crystal is not considered. Then, the local criterion can be expressed in a generic form:

$$f = |\tau| - \tau_{cr} \leq 0 \tag{1.8}$$

$$\tau = \boldsymbol{\sigma} : \boldsymbol{p} \tag{1.9}$$

with

$$\boldsymbol{p} = \frac{1}{2}\left(\underline{n} \otimes \underline{t} + \underline{t} \otimes \underline{n}\right) = \frac{1}{2}\left(\underline{e}_r \otimes \underline{e}_\theta + \underline{e}_\theta \otimes \underline{e}_r\right) \tag{1.10}$$

the orientation tensor, the normal direction to the slip plane being $\underline{e}_r = \underline{t}$, and the orientation vector of the slip line $\underline{e}_\theta = \underline{n}$.

The rate form of the constitutive equations, obtained through time derivation of the stress tensor $\boldsymbol{\sigma}$, takes then the following form:

$$\dot{\boldsymbol{\sigma}} = \mathbb{L} : \dot{\boldsymbol{\varepsilon}} = \mathbb{L} : (\dot{\boldsymbol{\varepsilon}} - \dot{\boldsymbol{\varepsilon}}^p) \tag{1.11}$$

where $\mathbb{L}$ denotes the fourth-order local tangent stiffness operator. The plastic strain $\dot{\boldsymbol{\varepsilon}}^p$ is determined by the normality rule:

$$\dot{\boldsymbol{\varepsilon}}^p = \dot{\lambda}\left(\frac{\partial f}{\partial \boldsymbol{\sigma}}\right) \tag{1.12}$$

This is completed by the standard consistency condition:

$$\dot{f} = \frac{\partial f}{\partial \boldsymbol{\sigma}} : \dot{\boldsymbol{\sigma}} = 0 \tag{1.13}$$

The tangent modulus $\mathbb{L}$ readily reads then:

$$\mathbb{L} = \begin{cases} \mathbb{C}^{el} & \text{if} \quad f(\boldsymbol{\sigma}) < 0 \quad \text{or} \quad f = 0 \quad \text{and} \quad \dot{f} < 0 \\ \mathbb{C}^{el} - \frac{(\mathbb{C}^{el}:\frac{\partial f}{\partial \boldsymbol{\sigma}})\otimes(\mathbb{C}^{el}:\frac{\partial f}{\partial \boldsymbol{\sigma}})}{(\frac{\partial f}{\partial \boldsymbol{\sigma}}:\mathbb{C}^{el}:\frac{\partial f}{\partial \boldsymbol{\sigma}})} & \text{if} \quad f(\boldsymbol{\sigma}) = 0 \quad \text{and} \quad \dot{f} = 0 \end{cases} \tag{1.14}$$

the tensor $\frac{\partial f}{\partial \boldsymbol{\sigma}} = \frac{1}{2}\left(\underline{e}_r \otimes \underline{e}_\theta + \underline{e}_\theta \otimes \underline{e}_r\right)$ which defines the direction of plastic flow contains the orientation information of each crystal grain.

According to the expression (1.14), one can note that the components of the tangent stiffness tensor $\mathbb{L}$ is identical to $\mathbb{C}^{el}$, except that the component $L_{r\theta r\theta}$ is equal to 0 when the Schmid criterion is attained. In other words, the shear stiffness disappears only in the intragranular laminated directions for $(\underline{e}_r, \underline{e}_\theta)$ once the crystal is plastified.

1.3.2 Polycrystalline plasticity of the clay

The elastoplastic response of the clay matrix is induced by two types of crystal properties: an anisotropy once when plasticity occurs (see Fig.1.3), and isotropic grains keeping their initial isotropy. Once the strength criterion is reached, the intrinsic anisotropic property of the crystal is activated. For elastic grains, the slip system is inactivated, and the crystal keeps its isotropic property.

Since we aim at applying the modeling to an uniaxial compressive loading, to describe the distribution of crystal orientations which are symmetric to the axis of revolution $\underline{e}_3$, it is necessary to introduce a critical orientation θ_c in the local plan of ($\underline{e}_r$,U). The crystals with this orientation is thus at *boundary of activation* (see Fig.1.5(a)). It can be concluded from (1.1),(1.9),(1.10) that in uniaxial compression test, the first critical crystal (first activated crystal) is oriented at the direction $\theta = 45^o$. With the increasing load, the orientations of plastified crystals will generate a cone with a symmetric axis $\theta = 45^o$. The area inside this cone represents orientations of plastified crystals with anisotropic properties, namely *Cone of plastified crystals*, while the area outside the cone represents the non-activated crystals having their elastic isotropic properties (*Cone of elastic crystals* on Fig.1.5(b)). The cone of activated crystals will become larger with an increasing load, until 90^o which corresponds to a complete plastification of the crystals. It must be emphasized that each plastified crystal has a different property according to its respective orientation (θ, ϕ, ψ).

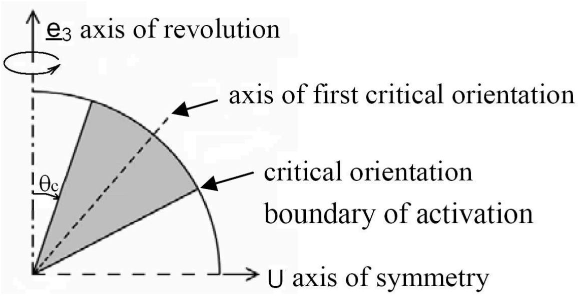

(a) Denomination of different axis

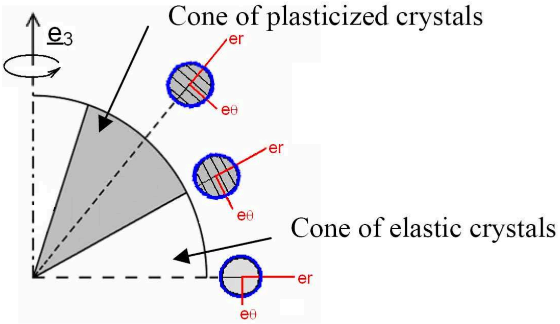

(b) Denomination of different areas

Figure 1.5: Orientation Distribution of activated and inactivated crystals

With progressively increasing number of activated crystal, the orientations of the plastified crystals vary, and the distribution of the orientations is not isotropic any more. In particular, it is important to note that the overall behavior of the homogenized medium composed by the above two types of grains becomes transversely isotropic.

1.3.3 Principle of incremental method with self-consistent scheme

In this section, the Hill's incremental formulation [Hill,65] is briefly reviewed and applied by corresponding self-consistent scheme.

1.3.3.1 Incremental method

Let us consider the representative volume element (RVE), defined by a geometrical domain Ω, this RVE is subjected on its boundary surface $\partial\Omega$ to a uniform strain rate field:

$$\dot{\underline{\xi}}(\underline{z}) = \dot{\mathbf{E}} \cdot \underline{z}, \underline{z} \in \partial\Omega \tag{1.15}$$

where $\underline{z}$ is the position vector defining the location in the RVE, and the tensor $\dot{\mathbf{E}}$ is the macroscopic strain rate. The RVE of heterogeneous material is composed of r $(r = 1, N)$

phases of solid. Here Ω_r and φ_r are the volume and the volume fraction of the phase r, respectively. The notations $\overline{a}$ and $\overline{a}_r$ will be used to denote the average of a field $a(\underline{z})$ in the entire RVE Ω and that in each phase Ω_r.

$$\overline{a} = \langle a \rangle = \sum_{r=1}^{N} \varphi_r \overline{a}_r \quad ; \quad \overline{a}_r = \langle a \rangle_r = \frac{1}{\Omega_r} \int_{\Omega_r} a\left(\underline{z}\right) d\underline{z} \tag{1.16}$$

As in (1.11), at the microscopic scale, the local nonlinear constitutive models are expressed in the following incremental form.

$$\dot{\boldsymbol{\sigma}}\left(\underline{z}\right) = \mathbb{L}\left(\underline{z}\right) : \dot{\boldsymbol{\varepsilon}}\left(\underline{z}\right) \tag{1.17}$$

Having in mind the classical Eshelby-based homogenization procedures [Eshelby,57] can be reused for the resolution of the nonlinear problem associated to (1.17), a tangent strain localization tensor $\mathbb{A}$ is introduced:

$$\dot{\boldsymbol{\varepsilon}}\left(\underline{z}\right) = \mathbb{A}\left(\underline{z}\right) : \dot{\mathbf{E}} \tag{1.18}$$

The macroscopic stress rate is derived from the local stress average rule:

$$\dot{\boldsymbol{\sigma}} = \overline{\dot{\boldsymbol{\sigma}}\left(\underline{z}\right)} \tag{1.19}$$

and reads:

$$\dot{\boldsymbol{\sigma}} = \mathbb{L}^{\text{hom}} : \dot{\mathbf{E}} = \overline{\mathbb{L}\left(\underline{z}\right) : \dot{\boldsymbol{\varepsilon}}\left(\underline{z}\right)} \tag{1.20}$$

where the macroscopic tangent operator $\mathbb{L}^{\text{hom}}$ is determined as:

$$\mathbb{L}^{\text{hom}} = \overline{\mathbb{L}\left(\underline{z}\right) : \mathbb{A}\left(\underline{z}\right)} \tag{1.21}$$

From the formula (1.21), the determination of macroscopic tangent operator is related to the local tangent localization tensor and local tangent stiffness at each point inside the RVE. Due to the nonlinearity, and the resulting strain heterogeneity, the tangent stiffness is approximated in each phase r by assuming that each phase has a uniform modulus, related to the average value of local strain field in phase r.

$$\forall \underline{z} \in (r), \qquad \dot{\boldsymbol{\sigma}}\left(\underline{z}\right) = \mathbb{L}_r : \dot{\boldsymbol{\varepsilon}}\left(\underline{z}\right) \tag{1.22}$$

With this hypothesis, the relation between microscopic and macroscopic strain rates for each phase and the tangent operator $\mathbb{L}^{\text{hom}}$ takes the form:

$$\dot{\boldsymbol{\varepsilon}}_r = \mathbb{A}_r : \dot{\mathbf{E}} \tag{1.23}$$

$$\mathbb{L}^{\text{hom}} = \overline{\mathbb{L}_r : \mathbb{A}_r} \tag{1.24}$$

where $\mathbb{A}_r$ represents the tangent strain localization tensor for each phase r with the averaged strain state.

1.3.3.2 Self-consistent scheme with laminated spheres

According to the morphology of clay matrix, a self-consistent approach is considered. Each particle of a given phase r reacts as if it is embedded in the equivalent homogeneous medium which is looked for. For this approach allowing to study materials with polycrystal-like granular morphology, the reader may refer for instance to [Kroner,78],[Suquet et al.,97],[Zaoui,02],[Dormieux et al.,06]. The tangent strain localization tensor reads in this case as:

$$\mathbb{A}_r = \left(\mathbb{I} + \mathbb{P}^0_I : \left(\mathbb{L}_r - \mathbb{L}^{\text{hom}}\right)\right)^{-1} : \left[\sum_{s=0}^{N} \varphi_s \left(\mathbb{I} + \mathbb{P}^0_I : \left(\mathbb{L}_s\left(\theta, \phi\right) - \mathbb{L}^{\text{hom}}\right)\right)^{-1}\right]^{-1} \tag{1.25}$$

The self-consistent has been modified due to the anisotropic characteristic of the laminated spherical particles which varies with orientations defined by (θ, ϕ) in the coordinate system (see section 1.2.2). Therefore, we assumed that the average strain rate in the domain of laminated sphere is obtained through the angular average. Here, the laminated particles being assumed isotropically distributed, one has:

$$\bar{\dot{\varepsilon}}_r = \int_{\phi=0}^{2\pi} \int_{\theta=0}^{\pi} \dot{\varepsilon}_r\left(\theta, \phi\right) \frac{\sin\theta}{4\pi} d\theta d\phi \tag{1.26}$$

With this hypothesis, the tangent strain localization tensor of self-consistent scheme can be rewritten as:

$$\begin{aligned} \mathbb{A}_r = \quad & \int_{\phi=0}^{2\pi} \int_{\theta=0}^{\pi} \left(\mathbb{I} + \mathbb{P}^0_I : \left(\mathbb{L}_r\left(\theta, \phi\right) - \mathbb{L}^{\text{hom}}\right)\right)^{-1} \frac{\sin\theta}{4\pi} d\theta d\phi \\ & : \left[\sum_{s=0}^{N} \varphi_s \int_{\phi=0}^{2\pi} \int_{\theta=0}^{\pi} \left(\mathbb{I} + \mathbb{P}^0_I : \left(\mathbb{L}_s\left(\theta, \phi\right) - \mathbb{L}^{\text{hom}}\right)\right)^{-1} \frac{\sin\theta}{4\pi} d\theta d\phi\right] \end{aligned} \tag{1.27}$$

where the tangent modulus $\mathbb{L}_r(\theta, \phi)$ of phase r depends on the orientation defined by (θ, ϕ). Introducing the (1.27) in (1.24) gives expression of the tangent operator:

$$\mathbb{L}^{\text{hom}} = \sum_{r=1}^{N} \varphi_r \mathbb{L}_r : \mathbb{A}_r \tag{1.28}$$

If distribution of the laminated spheres is not isotropic, the tangent strain localization tensor and the tangent operator is thus obtained by appropriately integrating the angle θ on the ranges of cones of plastified crystals and cones of elastic crystals (defined in Fig.1.5). It is important to note that for materials with inclusions of a same form and an isotropic orientation distribution of inclusions, one has:

$$\sum_{s=0}^{N} \varphi_s \int_{\phi=0}^{2\pi} \int_{\theta=0}^{\pi} \left(\mathbb{I} + \mathbb{P}_I^0 : \left(\mathbb{L}_s\left(\theta, \phi\right) - \mathbb{L}^{\text{hom}}\right)\right)^{-1} \frac{\sin\theta}{4\pi} d\theta d\phi = \mathbb{I} \tag{1.29}$$

However, this condition (1.29) is not satisfied in each self-consistent step until the end of the iterations.

$\mathbb{P}_I^0$ in (1.25) is the so-called Hill tensor which depends on both the geometry of the inclusions r (be considered here as spheres) and on the tangent operator of the matrix. Alternatively, the Hill tensor can be replaced by the equivalent Eshelby's tensor.

$$\mathbb{S}^{esh}\left(\mathbb{L}\right) = \mathbb{P}_I^0 : \mathbb{L} \tag{1.30}$$

As mentioned in section 1.3.2, the macroscopic behavior of the clay matrix becomes transversely isotropic once the grains begin to be plastified. So, a Hill polarization tensor problem for a spherical inclusion in a transversely isotropic medium is needed to be solved.

To this end, [Ghahremani,77],[Gavazzi and Lagoudas,90] have generated the numerical evaluation of Hill's tensor and Eshelby's tensor for ellipsoidal inclusions in anisotropic media. For transversely isotropic matrix containing spherical voids, closed-form expression of $\mathbb{P}$-tensor (or equivalently available Eshelby tensor) can be found in [Withers,89].

1.3.4 Numerical simulations

This section is devoted to assess the performance of this first level modelling for mesoscopic features of the elastoplastic behavior of clay matrix-like materials whose morphological model has been analyzed in the section 1.2. The mechanical behavior of the grains with perfect interfaces are predicted and analyzed according to different porosities.

The above model is applied to simulate uniaxial compression tests under strain rate-controlled condition. The model contains four parameters: two elastic constants for initial state of grains: E_s, υ_s, the critical value of the shear stress for grains τ_{cr}, and the porosity φ. The parameter values used for numerical simulations are: $E_s = 3000MPa$, $\nu_s = 0.3$, $\tau_{cr} = 1.5MPa$, $\varphi = 0.2, 0.3, 0.4, 0.45$ respectively. The predicted stress-strain curves for clay matrix are provided in Fig.1.6 for different porosities.

As commonly observed, the curves appear as bilinear, thus stress-strain curve can be divided into two phases. In the first phase, the material has an elastic behavior. We note that the elastic stiffness and the yield stress become much stronger when porosity is lower. The same phenomenon is also observed in the second plastic phase, where the tangent stiffness increases as the porosity is lower.

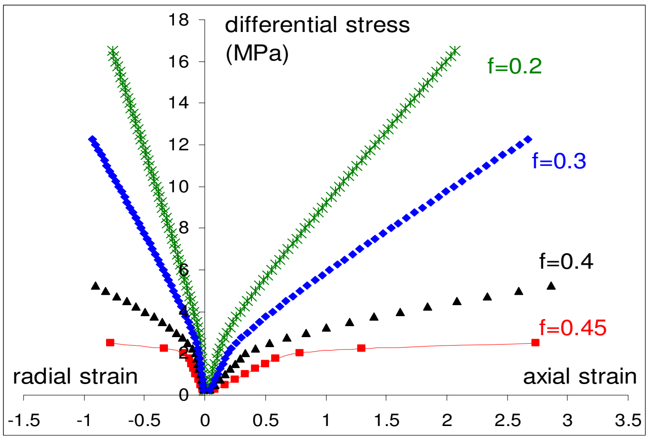

Figure 1.6: Axial and lateral strains versus deviatoric stress curves in numerical uniaxial compression tests with four different porosities $\varphi = 0.2, 0.3, 0.4, 0.45$

Despite its simplicity, the micromechanical model without consideration of interface leads to the conclusion that porosity has an important role in the interpretation of the failure mechanism of clays matrix. More specifically, only in the case of a high porosity about 0.45, the macroscopic rupture of laminated porous materials can be explained by the single local plastic mechanism which is the intra-particle slip between sheets. However, based on experimental data reported in [Alberto Ortega et al.,07] (for dozen samples of several different shales collected from open literatures [Dewhurst and siggins,06], [Domnesteanu et al.,02], [Jakobsen and Johansen.,00], [Jones and Wang,94], [Hornby,98]), it can be concluded that the clay matrix porosities φ are about from 0.12 to 0.37 which are much less than 0.45. That is why a second model which can take account of the second deformation mechanism of interface is due.

1.4 Plastic behavior of the polycrystal with imperfect interfaces

The classical based self-consistent scheme has been described above, and needs to be completed by consideration of the interfacial mechanical effects. In this section, a nonlinear homogenization problem will be solved by the following incremental method, for the problem of laminated spherical inclusion surrounded by imperfect interfaces (see section 1.4.3).

In order to capture the mechanical interactions at the contact surface between the crushing crystals during the deformation process, a displacement rate jump taking place at the contact surface I_{ij} between the solid grains $\mathcal{G}_i$ and $\mathcal{G}_j$ is introduced.

$$[\![\underline{\dot{\xi}}]\!] = \underline{\dot{\xi}}_j - \underline{\dot{\xi}}_i \tag{1.31}$$

Then, the overall interface surface in the RVE is defined as $\Gamma = \cup I_{ij}$, noting that $2|\Gamma| = \sum_i |\partial \mathcal{G}_i^s|$ where $\partial \mathcal{G}_i^s$ is the solid-to-solid contact boundary of constituent $\mathcal{G}_i$. Moreover, in order to implement the interface effects in homogenization methods, the idea is to represent the heterogeneous solid phase by a composite sphere $\mathcal{G} \cup \Gamma$. The composite sphere is made up of a homogeneous solid (isotropic or laminated) grain surrounded by an interface with normal tangential stiffness coefficients K_n and K_t. where a displacement rate jump of this kind of interface taking place at the boundary $\partial \mathcal{G}_i$ of the grain $\mathcal{G}_i$ reads:

$$\left[\underline{\dot{\xi}}\right]_i = \underline{\dot{\xi}}\left(R^+\right)_i - \underline{\dot{\xi}}\left(R^-\right)_i \tag{1.32}$$

$\underline{\dot{\xi}}(R^+)_i$ (resp. $\underline{\dot{\xi}}(R^-)_i$) denotes the displacement rate of the external (resp. internal) boundary $\partial \mathcal{G}_i^+$ (resp. $\partial \mathcal{G}_i^-$). Recalling (1.31) and considering identical composite spheres, we have:

$$[\![\underline{\dot{\xi}}]\!] = \left[\underline{\dot{\xi}}\right]_i - \left[\underline{\dot{\xi}}\right]_j = 2\left[\underline{\dot{\xi}}\right] \tag{1.33}$$

The nonlinear relation between the stress vector rate $\underline{\dot{T}}$ and the displacement rate jump $\left[\underline{\dot{\xi}}\right]$ can be expressed as:

$$\underline{\dot{T}} = \mathbf{K}^{tan} \cdot \left[\underline{\dot{\xi}}\right] \tag{1.34}$$

$$\mathbf{K}^{tan} = K_n^{tan} \underline{n} \otimes \underline{n} + K_t^{tan} \left(\mathbf{1} - \underline{n} \otimes \underline{n}\right) \tag{1.35}$$

where $\underline{n}$ is the outwards unit normal to the boundary of composite sphere, K_n^{tan} and K_t^{tan} are the normal and the tangential tangent stiffness of the interface, respectively. The component of the displacement rate jump and the stress vector rate can be expressed as follows:

$$\begin{aligned} \dot{T}_n &= \underline{\dot{T}} \cdot \underline{n} = K_n^{tan} \dot{\xi}_n \\ \underline{\dot{T}}_t &= \underline{\dot{T}} - \dot{T}_n \underline{n} = K_t^{tan} \left[\underline{\dot{\xi}}\right]_t \end{aligned} \tag{1.36}$$

with

$$\begin{aligned} \dot{\xi}_n &= \left[\underline{\dot{\xi}}\right] \cdot \underline{n} \\ \left[\underline{\dot{\xi}}\right]_t &= \left[\underline{\dot{\xi}}\right] - \dot{\xi}_n \cdot \underline{n} \end{aligned} \tag{1.37}$$

The average strain rate field of the solid is defined as a generalized strain rate filed $\dot{\varepsilon}^{gen}$ [Dormieux et al.,10] which is the sum of the smooth strain rate field $\dot{\varepsilon}$ in the solid grains and the contribution of the displacement rate jumps.

$$\dot{\varepsilon}^{gen}\left(\underline{z}\right) = \dot{\varepsilon}\left(\underline{z}\right) + \sum_i \left[\dot{\underline{\xi}}\right]_i \overset{s}{\otimes} \underline{n}_i\left(\underline{z}\right)\delta_{\partial\mathcal{G}_i^s} \tag{1.38}$$

$\delta_{\partial\mathcal{G}_i^s}$ being the Dirac distribution. The macroscopic strain rate then can be rewritten as:

$$\dot{\mathbf{E}} = \frac{1}{\Omega}\left(\sum_i \int_{\mathcal{G}_i} \dot{\varepsilon} dV + \sum_i \int_{\partial\mathcal{G}_i^s} \left[\dot{\underline{\xi}}\right]_i \overset{s}{\otimes} \underline{n}_i dS + \int_{\mathcal{G}_p} \dot{\varepsilon} dV\right) \tag{1.39}$$

1.4.1 Self-consistent scheme for generalized Eshelby problem

The Generalized Eshelby problem for the isotropic grains with interfaces is presented in Fig.1.7. An auxiliary macroscopic strain rate $\dot{\mathbf{E}}_0$ is applied on the RVE boundary surface $\partial\Omega$ at infinity.

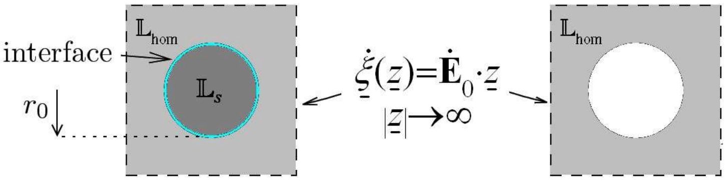

Figure 1.7: Generalized Eshelby problem for an isotropic grain surrounded by interface and for spherical pore

For the problem of a pore as an inclusion embedded in the infinite medium with stiffness $\mathbb{L}_{\text{hom}}$, the average strain rate can be readily written as:

$$\overline{\dot{\varepsilon}}^p = \left(\mathbb{I} - \mathbb{S}_{sph}^{\text{hom}}\right)^{-1} : \dot{\mathbf{E}}_0 \tag{1.40}$$

For the problem of a spherical inclusion of radius r_0 having an isotropic tangent stiffness $\mathbb{L}_s$ and surrounded by an interface embedded in the infinite medium with stiffness $\mathbb{L}_{\text{hom}}$, the following Eshelby problem needs to be solved:

$$\begin{cases} r < r_0, & \dot{\boldsymbol{\sigma}} = \mathbb{L}_s : \dot{\varepsilon} \\ r = r_0, & \dot{\boldsymbol{\sigma}} \cdot \underline{e}_r = \mathbf{K}^{tan} \cdot \left[\dot{\underline{\xi}}\right] \\ r > r_0, & \dot{\boldsymbol{\sigma}} = \mathbb{L}_{\text{hom}} : \dot{\varepsilon} \\ \underline{z} \rightarrow \infty, & \dot{\underline{\xi}} = \dot{\mathbf{E}}_0 \cdot \underline{z} \end{cases} \tag{1.41}$$

Based on definitions (1.32) and (1.33), the average stress rate $\overline{\dot{\boldsymbol{\sigma}}}^{S\cup I}$ attached to the entire grain and the interface reads:

$$\overline{\dot{\boldsymbol{\sigma}}}^{S\cup I} = \frac{1}{\Omega}\int_{r=r_0} \dot{\boldsymbol{\sigma}}^{esh} dV = \frac{3}{4\pi r_0^2}\int_{r=r_0} \underline{e}_r \otimes \dot{\boldsymbol{\sigma}}^{esh} \cdot \underline{e}_r dS \tag{1.42}$$

where superscript of $S \cup I$ (resp. s) represents the solid sphere with interface (resp. spherical solid). The average strain rate $\overline{\dot{\boldsymbol{\varepsilon}}}^{s}$ and the average strain rate $\overline{\dot{\boldsymbol{\varepsilon}}}^{S\cup I}$ can be written as follows:

$$\overline{\dot{\boldsymbol{\varepsilon}}}^{s} = \frac{1}{\Omega}\int_{r=r_0^-} \underline{\dot{\xi}}^{esh}\left(r_0^-\right) \overset{s}{\otimes} \underline{e}_r dS \tag{1.43}$$

$$\overline{\dot{\boldsymbol{\varepsilon}}}^{S\cup I} = \frac{1}{\Omega}\int_{r=r_0^+} \underline{\dot{\xi}}^{esh}\left(r_0^+\right) \overset{s}{\otimes} \underline{e}_r dS \tag{1.44}$$

where $\dot{\boldsymbol{\sigma}}^{esh}$, $\underline{\dot{\xi}}^{esh}$ are the solutions of (1.41) which have been obtained in [Hashin,91], [Herve and Zaoui,93], [Sanahuja,08] for the case of isotropic grain. $r = r_0^+$ (resp. $r = r_0^-$) represents the external lip face (resp. internal lip face) of the interface $r = r_0$.

Then, according to (1.23), the micro-macroscopic strain rate relation reads:

$$\begin{aligned} \overline{\dot{\boldsymbol{\varepsilon}}}^{s} &= \mathbb{A}^{s} : \dot{\mathbf{E}}_0 \\ \overline{\dot{\boldsymbol{\varepsilon}}}^{S\cup I} &= \mathbb{A}^{S\cup I} : \dot{\mathbf{E}}_0 \\ \overline{\dot{\boldsymbol{\sigma}}}^{S\cup I} &= \mathbb{B}^{S\cup I} : \dot{\mathbf{E}}_0 \end{aligned} \tag{1.45}$$

where $\mathbb{A}^{S\cup I}$ is the strain localization tensor, while $\mathbb{B}^{S\cup I}$ represents the stress localization tensors. Both have to be determined. $\overline{\dot{\boldsymbol{\varepsilon}}}^{S\cup I}$ (resp. $\overline{\dot{\boldsymbol{\sigma}}}^{S\cup I}$) is the average strain rate (resp. stress rate) of the whole solid composite sphere. The solid space (resp. pore space) in the RVE Ω is denoted by Ω_s (resp. Ω_p). φ is the pore volume fraction. According to (1.16), the relation between $\dot{\boldsymbol{\sigma}}$ and $\dot{\mathbf{E}}_0$ reads:

$$\dot{\boldsymbol{\sigma}} = (1-\varphi)\,\overline{\dot{\boldsymbol{\sigma}}}^{S\cup I} = (1-\varphi)\,\mathbb{B}^{S\cup I} : \dot{\mathbf{E}}_0 \tag{1.46}$$

We have now to link the auxiliary strain rate $\dot{\mathbf{E}}_0$ to the macroscopic strain rate $\dot{\mathbf{E}}$ by adopting (1.40) and applying the strain rate average rule, the macroscopic strain then reads:

$$\dot{\mathbf{E}} = \varphi\overline{\dot{\boldsymbol{\varepsilon}}}^{p} + (1-\varphi)\,\overline{\dot{\boldsymbol{\varepsilon}}}^{S\cup I} = \left(\varphi\left(\mathbb{I} - \mathbb{S}^{\text{hom}}_{sph}\right)^{-1} + (1-\varphi)\,\mathbb{A}^{S\cup I}\right) : \dot{\mathbf{E}}_0 \tag{1.47}$$

Combining (1.46) with (1.47) readily yields the macroscopic stress rate-strain rate relation:

$$\dot{\boldsymbol{\sigma}} = (1-\varphi)\,\mathbb{B}^{S\cup I} : \left(\varphi\left(\mathbb{I} - \mathbb{S}^{\text{hom}}_{sph}\right)^{-1} + (1-\varphi)\,\mathbb{A}^{S\cup I}\right)^{-1} : \dot{\mathbf{E}} \tag{1.48}$$

which shows that the generalised self-consistent estimate of the effective tangent stiffness operator can be written as:

$$\mathbb{L}^{\text{hom}} = (1-\varphi)\,\mathbb{B}^{S\cup I} : \left(\varphi\left(\mathbb{I}-\mathbb{S}^{\text{hom}}_{sph}\right)^{-1} + (1-\varphi)\,\mathbb{A}^{S\cup I}\right)^{-1} \tag{1.49}$$

where $\mathbb{A}^{S\cup I}$ and $\mathbb{B}^{S\cup I}$ will be determined in the following for the case of isotropic sphere and the case of laminated sphere respectively.

1.4.2 Solution for isotropic grains with imperfect interfaces

In the case of isotropic grains with imperfect interfaces, the problem (1.41) in 3D context will be solved successively by considering a spherical strain rate-controlled loading $\dot{\mathbf{E}}_0 = \dot{E}_0\mathbf{1}$ and a deviatoric strain rate-controlled loading $\dot{\mathbf{E}}_0 = \dot{E}_0(\underline{e}_1 \otimes \underline{e}_1 - \underline{e}_2 \otimes \underline{e}_2)$.

1.4.2.1 Isotropic loading

For the isotropic loading $\dot{\mathbf{E}}_0 = \dot{E}_0\mathbf{1}$, owing to the spherical symmetry and the boundary condition at infinity, the displacement rate field is looked for in the form

$$\dot{\underline{\xi}}^{esh}_i(\underline{z}) = \left(a_i r + \frac{b_i}{r^2}\right)\underline{e}_r \tag{1.50}$$

where $i = s$ (resp. $i = \text{hom}$) represents the medium inside the inclusion (resp. the medium outside the inclusion). The micro-macro strain rate relation (1.45) can be then written as,

$$\begin{aligned}
\dot{\bar{\boldsymbol{\varepsilon}}}^{s}_{sph} &= \alpha^{s}_{sph}\dot{\mathbf{E}}_0 = \alpha^{s}_{sph}\dot{E}_0\mathbf{1}\\
\dot{\bar{\boldsymbol{\varepsilon}}}^{S\cup I}_{sph} &= \alpha^{S\cup I}_{sph}\dot{\mathbf{E}}_0 = \alpha^{S\cup I}_{sph}\dot{E}_0\mathbf{1}\\
\dot{\bar{\boldsymbol{\sigma}}}^{S\cup I}_{sph} &= \beta^{S\cup I}_{sph}\dot{\mathbf{E}}_0 = \beta^{S\cup I}_{sph}\dot{E}_0\mathbf{1}
\end{aligned} \tag{1.51}$$

By taking into account boundary conditions and continuity conditions on the interface $r = r_0$, one can find the required coefficients of a_i and b_i to express the solutions of $\dot{\underline{\xi}}^{esh}$, $\dot{\boldsymbol{\sigma}}^{esh}$ according to (1.50), where $i = s$ (resp. $i = \text{hom}$) which represents the medium inside the inclusion (resp. outside the inclusion). The components α^{s}_{sph}, $\alpha^{S\cup I}_{sph}$, $\beta^{S\cup I}_{sph}$ of the spherical parts of the tensors $\mathbb{A}^{s}$, $\mathbb{A}^{S\cup I}$ and $\mathbb{B}^{S\cup I}$ can then be deduced according to (1.51). After some analytical calculations, one obtains,

$$\begin{aligned}
\alpha^{s}_{sph} &= \frac{\left(3k^{\text{hom}}+4\mu^{\text{hom}}\right)K_n^{tan}r_0}{\left(3k^{s}+4\mu^{\text{hom}}\right)K_n^{tan}r_0+12k^{s}\mu^{\text{hom}}}\\
\alpha^{S\cup I}_{sph} &= \frac{\left(3k^{\text{hom}}+4\mu^{\text{hom}}\right)\left(K_n^{tan}r_0+3k^{s}\right)}{\left(3k^{s}+4\mu^{\text{hom}}\right)K_n^{tan}r_0+12k^{s}\mu^{\text{hom}}}\\
\beta^{S\cup I}_{sph} &= \frac{3\left(3k^{\text{hom}}+4\mu^{\text{hom}}\right)K_n^{tan}r_0k^{s}}{4\mu^{\text{hom}}K_n^{tan}r_0+3k^{s}K_n^{tan}r_0+12k^{s}\mu^{\text{hom}}}
\end{aligned} \tag{1.52}$$

for which, the grain being isotropic, the tangent stiffness tensors read:

$$\begin{aligned} \mathbb{L}^{\text{hom}} &= 3k^{\text{hom}}\mathbb{J} + 2\mu^{\text{hom}}\mathbb{K} \\ \mathbb{L}^{s} &= 3k^{s}\mathbb{J} + 2\mu^{s}\mathbb{K} \end{aligned} \tag{1.53}$$

1.4.2.2 Deviatoric loading

Let us consider the deviatoric loading $\dot{\mathbf{E}}_0 = \dot{E}_0(\underline{e}_1 \otimes \underline{e}_1 - \underline{e}_2 \otimes \underline{e}_2)$ expressed in the orthonormal system $(\underline{e}_1, \underline{e}_2, \underline{e}_3)$. Based on [Love,44], the displacement rate field is sought in the form (spherical coordinate system (r, θ, ϕ) is considered):

$$\dot{\underline{\xi}}_i^{esh}(\underline{z}) = \dot{\xi}_r^{esh}(r) \sin^2\theta \cos 2\phi \underline{e}_r + \dot{\xi}_\theta^{esh}(r) \sin\theta \cos\theta \cos 2\phi \underline{e}_\theta + \dot{\xi}_\phi^{esh}(r) \sin\theta \sin 2\phi \underline{e}_\phi \tag{1.54}$$

With the components of $\dot{\xi}_r^{esh}(r)$, $\dot{\xi}_\theta^{esh}(r)$, $\dot{\xi}_\phi^{esh}(r)$ written in the following form:

$$\begin{aligned} \dot{\xi}_r^{esh}(r) &= a_i r - \tfrac{6\upsilon_i}{1-2\upsilon_i} b_i r^3 + 3\tfrac{c_i}{r^4} + \tfrac{5-4\upsilon_i}{1-2\upsilon_i}\tfrac{d_i}{r^2} \\ \dot{\xi}_\theta^{esh}(r) &= a_i r - \tfrac{7-4\upsilon_i}{1-2\upsilon_i} b_i r^3 - 2\tfrac{c_i}{r^4} + 2\tfrac{d_i}{r^2} \\ \dot{\xi}_\phi^{esh}(r) &= -\dot{\xi}_\theta^{esh}(r) \end{aligned} \tag{1.55}$$

where $\dot{E}^i$, υ^i denotes the tangent modulus and the Poisson's ratio; a_i, b_i, c_i, d_i are the coefficients, with $i = s$ (resp. $i = \text{hom}$) which represents the medium inside the inclusion (resp. outside the inclusion). As in (1.50), by taking into account the boundary conditions and continuity conditions at the interface $r = r_0$, (1.45) can be written as:

$$\begin{aligned} \bar{\dot{\varepsilon}}_{dev}^{s} &= \alpha_{dev}^{s}\dot{\mathbf{E}}_0 = \alpha_{dev}^{s}\dot{E}_0(\underline{e}_1 \otimes \underline{e}_1 - \underline{e}_2 \otimes \underline{e}_2) \\ \bar{\dot{\varepsilon}}_{dev}^{S\cup I} &= \alpha_{dev}^{S\cup I}\dot{\mathbf{E}}_0 = \alpha_{dev}^{S\cup I}\dot{E}_0(\underline{e}_1 \otimes \underline{e}_1 - \underline{e}_2 \otimes \underline{e}_2) \\ \bar{\dot{\sigma}}_{dev}^{S\cup I} &= \beta_{dev}^{S\cup I}\dot{\mathbf{E}}_0 = \beta_{dev}^{S\cup I}\dot{E}_0(\underline{e}_1 \otimes \underline{e}_1 - \underline{e}_2 \otimes \underline{e}_2) \end{aligned} \tag{1.56}$$

with the deviatoric components α_{dev}^{s}, $\alpha_{dev}^{S\cup I}$, $\beta_{dev}^{S\cup I}$ of the tensors $\mathbb{A}^{S\cup I}$, $\mathbb{B}^{S\cup I}$ which read,

$$\begin{aligned} \alpha_{dev}^{s} &= \left(a_s - \tfrac{21}{5(1-2\nu^s)} b_s r_0^2\right)\tfrac{1}{\dot{E}_0} \\ \alpha_{dev}^{S\cup I} &= \left(a_{\text{hom}} + \tfrac{4\left(4-\nu^{\text{hom}}\right)}{5\left(1-2\nu^{\text{hom}}\right)}\tfrac{d_{\text{hom}}}{r_0^3}\right)\tfrac{1}{\dot{E}_0} \\ \beta_{dev}^{S\cup I} &= \left(\tfrac{a_s}{(1+2\nu^s)} - \tfrac{21 b_s r_0^2}{5(1+2\nu^s)(1-2\nu^s)}\right)\tfrac{\dot{E}^s}{\dot{E}_0} \end{aligned} \tag{1.57}$$

However, the corresponding expressions of a_i, b_i, c_i, d_i are too heavy to be written here.

1.4.3 Solution for laminated grains with imperfect interfaces

The problem of spherical laminated grains (composed of parallel sheets) surrounded by interfaces will be solved in this section. The behavior of the interface is still the same as that described in (1.34) and (1.35) in order to implement homogenization methods. The mechanical property in each layer of the grain is considered to be isotropic and can be characterized by $\mathbb{L}^s = 3k^s\mathbb{J} + 2\mu^s\mathbb{K}$. The equivalent homogenized medium which plays the role of the reference medium showed in the Fig.1.8 has a transversely isotropic property $\mathbb{L}^{\text{hom}}$.

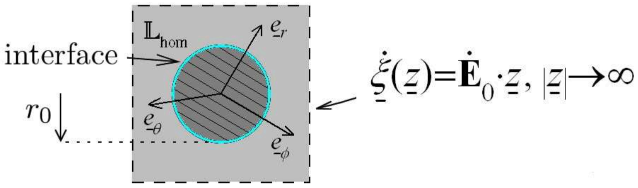

Figure 1.8: Eshelby Problem for laminated grain surrounded by interface

It turns out that the corresponding generalized Eshelby problem appears to be complicated to be solved analytically in the 3D context. Here a numerical way is proposed to solve this problem. To this end, an isotropization technique applied to $\mathbb{L}^{\text{hom}}$ is proposed as follows,

$$\begin{aligned} k^{\text{hom}}_{approx} &= \tfrac{1}{3}\left(L^{\text{hom}}_{rrrr} + L^{\text{hom}}_{rr\theta\theta} + L^{\text{hom}}_{rr\phi\phi}\right) \\ \mu^{\text{hom}}_{approx} &= L^{\text{hom}}_{\theta\phi\theta\phi} \\ \mathbb{L}^{\text{hom}}_{approx} &= 3k^{\text{hom}}_{approx}\mathbb{J} + 2\mu^{\text{hom}}_{approx}\mathbb{K} \end{aligned} \tag{1.58}$$

That is to say, the transversely isotropic tangent stiffness is approximated by an isotropic one at each iteration of the self-consistent procedure. The solution of the problem for laminated grain with imperfect interface in 3D context will be sought, as the procedure in section 1.4.2, by considering successively the different strain rate-controlled loading directions. Owing to that the shear stiffness disappears only in laminated directions for $(\underline{e}_r, \underline{e}_\theta)$ and the structure presents an axis of revolution $\underline{e}_3$, 5 representative loading directions can be selected as follows:

$$\begin{aligned} &\dot{\mathbf{E}}_0 = \dot{E}_0\mathbf{1}, \\ &\dot{\mathbf{E}}_0 = \dot{E}_0\left(-\underline{e}_r\otimes\underline{e}_r + \underline{e}_\theta\otimes\underline{e}_\theta\right), \quad \dot{\mathbf{E}}_0 = \dot{E}_0\left(\underline{e}_\theta\otimes\underline{e}_\phi + \underline{e}_\phi\otimes\underline{e}_\theta\right) \\ &\dot{\mathbf{E}}_0 = \dot{E}_0\left(\underline{e}_r\otimes\underline{e}_\theta + \underline{e}_\theta\otimes\underline{e}_r\right), \quad \dot{\mathbf{E}}_0 = \dot{E}_0\left(\underline{e}_r\otimes\underline{e}_\phi + \underline{e}_\phi\otimes\underline{e}_r\right) \end{aligned} \tag{1.59}$$

It is important to note that the resolution for this problem is realized in the local coordinate system $(\underline{e}_r, \underline{e}_\theta, \underline{e}_\phi)$.

For the spherical strain rate-controlled loading $\dot{\mathbf{E}}_0 = \dot{E}_0\mathbf{1}$ and the deviatoric strain rate-controlled loading of $\dot{\mathbf{E}}_0 = \dot{E}_0(-\underline{e}_r\otimes\underline{e}_r + \underline{e}_\theta\otimes\underline{e}_\theta), \dot{\mathbf{E}}_0 = \dot{E}_0(\underline{e}_\theta\otimes\underline{e}_\phi + \underline{e}_\phi\otimes\underline{e}_\theta), \dot{\mathbf{E}}_0 = \dot{E}_0(\underline{e}_r\otimes\underline{e}_\phi + \underline{e}_\phi\otimes\underline{e}_r)$, the laminated sphere can be considered as an isotropic medium since the only sliding happens in the direction of $(\underline{e}_r, \underline{e}_\theta)$. By using the isotropization technique (1.58), the anisotropic tangent stiffness has been replaced by an isotropic one. Therefore, the results (1.52)(1.57) can be still considered. The components of the tensors $\mathbb{A}^s$, $\mathbb{A}^{S\cup I}$ and $\mathbb{B}^{S\cup I}$ read then:

$$\begin{aligned}
\alpha^s_{rr\theta\theta} = \alpha^s_{\theta\phi\phi\theta} = \alpha^s_{r\phi\phi r} &= \left(a_s - \tfrac{21}{5(1-2\nu^s)} b_s r_0^2\right) \tfrac{1}{\dot{E}_0} \\
\alpha^{S\cup I}_{rr\theta\theta} = \alpha^{S\cup I}_{\theta\phi\phi\theta} = \alpha^{S\cup I}_{r\phi\phi r} &= \left(a_{\text{hom}} + \tfrac{4\left(4-\nu^{\text{hom}}_{approx}\right)}{5\left(1-2\nu^{\text{hom}}_{approx}\right)} \tfrac{d_{\text{hom}}}{r_0^3}\right) \tfrac{1}{\dot{E}_0} \\
\beta^{S\cup I}_{rr\theta\theta} = \beta^{S\cup I}_{\theta\phi\phi\theta} = \beta^{S\cup I}_{r\phi\phi r} &= \left(\tfrac{a_s}{(1+2\nu^s)} - \tfrac{21 b_s r_0^2}{5(1+2\nu^s)(1-2\nu^s)}\right) \tfrac{\dot{E}^s}{\dot{E}_0}
\end{aligned} \tag{1.60}$$

In the loading direction $\dot{\mathbf{E}}_0 = \dot{E}_0(\underline{e}_\theta \otimes \underline{e}_r + \underline{e}_r \otimes \underline{e}_\theta)$ where the sliding occurs, the inhomogeneous solid deforms as a pore. Therefore, the stress rate filed in this direction will be zero. The components α and β read then:

$$\begin{aligned}
\alpha^{S\cup I}_{r\theta\theta r} &= \left(1 - \tfrac{6\left(k^{\text{hom}}_{approx} + 2\mu^{\text{hom}}_{approx}\right)}{5\left(3k^{\text{hom}}_{approx} + 4\mu^{\text{hom}}_{approx}\right)}\right)^{-1} \tfrac{1}{\dot{E}_0} \\
\beta^{S\cup I}_{r\theta\theta r} &= 0
\end{aligned} \tag{1.61}$$

1.4.4 Determination of the localization tensor

Until now, all the components of the tensors $\mathbb{A}^{S\cup I}, \mathbb{B}^{S\cup I}$ have been determined by applying the different loading directions. Owing to symmetry properties, the micro-macro strain rate relation can be summarized as follow, with $i = S \cup I$ or s,

$$\bar{\dot{\varepsilon}} = \begin{cases}
\alpha^i_{sph} \dot{\mathbf{E}}_0 & if \quad \dot{\mathbf{E}}_0 = \dot{E}_0 \mathbf{1} \\
\alpha^i_{rr\theta\theta} \dot{\mathbf{E}}_0 & if \quad \dot{\mathbf{E}}_0 = \dot{E}_0(-\underline{e}_r \otimes \underline{e}_r + \underline{e}_\theta \otimes \underline{e}_\theta) \\
\alpha^i_{\theta\phi\phi\theta} \dot{\mathbf{E}}_0 & if \quad \dot{\mathbf{E}}_0 = \dot{E}_0(\underline{e}_\theta \otimes \underline{e}_\phi + \underline{e}_\phi \otimes \underline{e}_\theta) = \dot{E}_0(\underline{e}_\theta \otimes \underline{e}_\theta - \underline{e}_\phi \otimes \underline{e}_\phi) \\
\alpha^i_{r\phi\phi r} \dot{\mathbf{E}}_0 & if \quad \dot{\mathbf{E}}_0 = \dot{E}_0(\underline{e}_r \otimes \underline{e}_\phi + \underline{e}_\phi \otimes \underline{e}_r) \\
\alpha^i_{r\theta\theta r} \dot{\mathbf{E}}_0 & if \quad \dot{\mathbf{E}}_0 = \dot{E}_0(\underline{e}_r \otimes \underline{e}_\theta + \underline{e}_\theta \otimes \underline{e}_r)
\end{cases} \tag{1.62}$$

The tangent localization tensor of the laminated grain with interface, in form of Voigt matrix $\mathrm{A}^i_{layer}(\underline{e}_r, \underline{e}_\theta, \underline{e}_\phi)$, can be written in the coordinate system of $(\underline{e}_r, \underline{e}_\theta, \underline{e}_\phi)$ as follow:

$$\mathrm{A}^{i}_{\left(\underline{e}_r,\underline{e}_\theta,\underline{e}_\phi\right)} = \frac{1}{3}\cdot$$
$$\begin{bmatrix} \alpha^i_{sph}+2\alpha^i_{rr\theta\theta} & \alpha^i_{sph}-\alpha^i_{rr\theta\theta} & \alpha^i_{sph}-\alpha^i_{rr\theta\theta} & & & \\ \alpha^i_{sph}-2\alpha^i_{rr\theta\theta}+\alpha^i_{\theta\phi\phi\theta} & \alpha^i_{sph}+\alpha^i_{rr\theta\theta}+\alpha^i_{\theta\phi\phi\theta} & \alpha^i_{sph}+\alpha^i_{rr\theta\theta}-2\alpha^i_{\theta\phi\phi\theta} & & & \\ \alpha^i_{sph}-\alpha^i_{\theta\phi\phi\theta} & \alpha^i_{sph}-\alpha^i_{\theta\phi\phi\theta} & \alpha^i_{sph}+2\alpha^i_{\theta\phi\phi\theta} & & & \\ & & & 3\alpha^i_{\theta\phi\phi\theta} & & \\ & & & & 3\alpha^i_{r\phi\phi r} & \\ & & & & & 3\alpha^i_{r\theta\theta r} \end{bmatrix} \tag{1.63}$$

which gives rise to micro-macro strain rate relation (1.45) in Voigt notation:

$$\begin{bmatrix} \dot{\varepsilon}_{0rr} \\ \dot{\varepsilon}_{0\theta\theta} \\ \dot{\varepsilon}_{0\phi\phi} \\ \dot{\varepsilon}_{0\theta\phi} \\ \dot{\varepsilon}_{0r\phi} \\ \dot{\varepsilon}_{0r\theta} \end{bmatrix}_{\left(\underline{e}_r,\underline{e}_\theta,\underline{e}_\phi\right)} = \mathrm{A}^{i}_{layer}\left(\underline{e}_r,\underline{e}_\theta,\underline{e}_\phi\right) \begin{bmatrix} \dot{\mathbf{E}}_{0rr} \\ \dot{\mathbf{E}}_{0\theta\theta} \\ \dot{\mathbf{E}}_{0\phi\phi} \\ \dot{\mathbf{E}}_{0\theta\phi} \\ \dot{\mathbf{E}}_{0r\phi} \\ \dot{\mathbf{E}}_{0r\theta} \end{bmatrix}_{\left(\underline{e}_r,\underline{e}_\theta,\underline{e}_\phi\right)} \tag{1.64}$$

The tensor $\mathbb{B}^{S\cup I}$ can be readily constructed by replacing α^i in $\mathbb{A}^{S\cup I}$ by β^i.

As mentioned earlier in section 1.2, each plastified crystal in the clay matrix has a different property depending on its particular orientation (θ, ϕ, ψ). Therefore, the rotation matrix (1.4) and the relation (1.6) are considered in order to modify the tangent localization tensor (1.63) into the material co-rotational coordinate system $(\underline{e}_1, \underline{e}_2, \underline{e}_3)$. The tangent localization tensor in this global system $(\underline{e}_1, \underline{e}_2, \underline{e}_3)$ is written as,

$$\mathrm{A}^{i}_{layer}\left(\theta,\phi,\psi\right)_{\left(\underline{e}_1,\underline{e}_2,\underline{e}_3\right)} = T^{-1}\left(\theta,\phi,\psi\right)\mathrm{A}^{i}_{layer\left(\underline{e}_r,\underline{e}_\theta,\underline{e}_\phi\right)}T\left(\theta,\phi,\psi\right) \tag{1.65}$$

Therefore, according to (1.65) the average effective tangent stiffness operator (1.49) in the case of an isotropic distribution of laminated grains with imperfect interfaces can be rewritten as:

$$\left\langle \mathbb{L}^{\text{hom}} \right\rangle = (1-\varphi)\left\langle \mathbb{B}^{S\cup I}\right\rangle : \left(\varphi\left(\mathbb{I}-\mathbb{S}^{\text{hom}}_{sph}\right)^{-1} + (1-\varphi)\left\langle \mathbb{A}^{S\cup I}\right\rangle\right)^{-1} \tag{1.66}$$

where by still using the notation $\left\langle \mathbb{A}^{S\cup I}\right\rangle$, $\left\langle \mathbb{B}^{S\cup I}\right\rangle$ can be expressed as:

$$\begin{aligned} \left\langle \mathrm{A}^{S\cup I}\right\rangle &= \textstyle\int_{\phi=0}^{2\pi}\int_{\theta=0}^{\pi} T^{-1}\left(\theta,\phi,\psi\right)\mathrm{A}^{i}_{layer\left(\underline{e}_r,\underline{e}_\theta,\underline{e}_\phi\right)}T\left(\theta,\phi,\psi\right)\frac{\sin\theta}{4\pi}d\theta d\phi \\ \left\langle \mathrm{B}^{S\cup I}\right\rangle &= \textstyle\int_{\phi=0}^{2\pi}\int_{\theta=0}^{\pi} T^{-1}\left(\theta,\phi,\psi\right)\mathrm{B}^{i}_{layer\left(\underline{e}_r,\underline{e}_\theta,\underline{e}_\phi\right)}T\left(\theta,\phi,\psi\right)\frac{\sin\theta}{4\pi}d\theta d\phi \end{aligned} \tag{1.67}$$

Finally, the tangent localization tensors in form of Voigt matrix, of the isotropic grain with imperfect interface which do not depend on its orientation, can be obtained directly by simplifying the matrix (1.63):

$$\mathrm{A}^i_{iso(\underline{e}_1,\underline{e}_2,\underline{e}_3)} = \frac{1}{3}\begin{bmatrix} \alpha^i_{sph}+2\alpha^i_{dev} & \alpha^i_{sph}-\alpha^i_{dev} & \alpha^i_{sph}-\alpha^i_{dev} & & & \\ \alpha^i_{sph}-\alpha^i_{dev} & \alpha^i_{sph}+2\alpha^i_{dev} & \alpha^i_{sph}-\alpha^i_{dev} & & & \\ \alpha^i_{sph}-\alpha^i_{dev} & \alpha^i_{sph}-\alpha^i_{dev} & \alpha^i_{sph}+2\alpha^i_{dev} & & & \\ & & & 3\alpha^i_{dev} & & \\ & & & & 3\alpha^i_{dev} & \\ & & & & & 3\alpha^i_{dev} \end{bmatrix} \quad (1.68)$$

1.5 Validation and numerical simulations

The second model described in section 1.4 which can consider the effect of imperfect interface will be assessed by comparing its predictions to that of the first model corresponding to perfect interface (see section 1.5.1). In section 1.5.2, the second model is implemented with the consideration of the two local plastic mechanisms simultaneously to predict the elastoplastic stress-strain responds of porous clay matrix. The predicted behaviors in this section are not compared to the laboratory results which are still not available from traditional tests. The main objective of these predictions is to understand the macroscopic elastoplastic behavior stemming from a point of view of the microscopic scale.

1.5.1 Comparison of the two proposed models

In order to demonstrate the validity of the second model, comparisons of numerical predictions between the two methods are performed in this section. To this end, we keep the same parameters for both two models. Here, additional parameter values used in the second model are: $r_0 = 1\times10^{-6}$ and K^{tan}_n, K^{tan}_t equal to infinity for the case of perfect interface predictions. The predictions of the stress-strain behavior by the two models are provided in Fig.1.9 for two porosities: $\varphi = 0.2, 0.3$.

It is readily seen that the predictions of the two different models are similar. However, it must be emphasized that the first model has required an isotropization procedure. The difference brought by such isotropization technique is clearly shown in Fig.1.10 for two porosities:

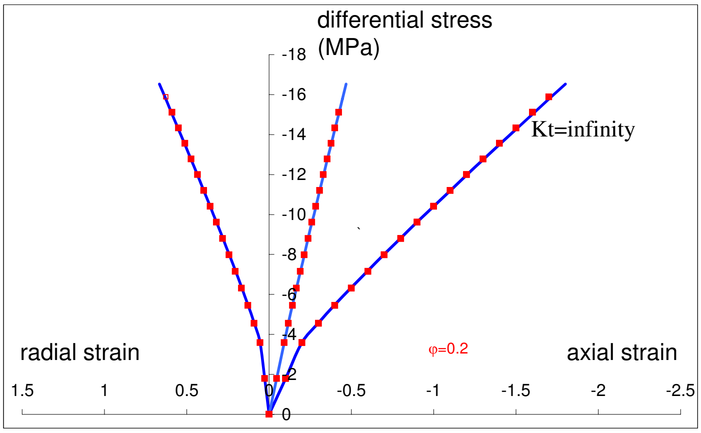

(a) Uniaxial compression test with $\varphi = 0.2$

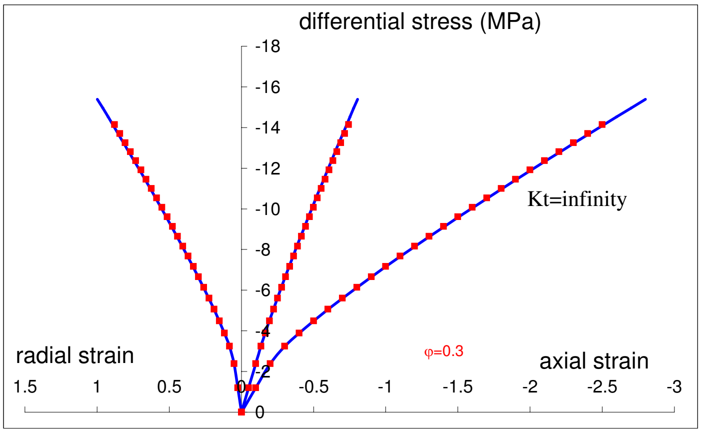

(b) Uniaxial compression test with $\varphi = 0.3$

Figure 1.9: Axial and lateral strains versus deviatoric stress curves in uniaxial compression tests - Comparison between predictions of the model without interface (solid lines) and that with interface

$\varphi = 0.2, 0.3$.

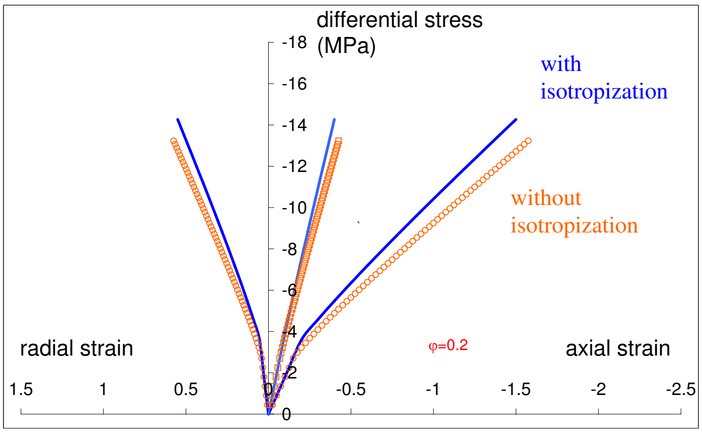

(a) Uniaxial compression test with $\varphi = 0.2$

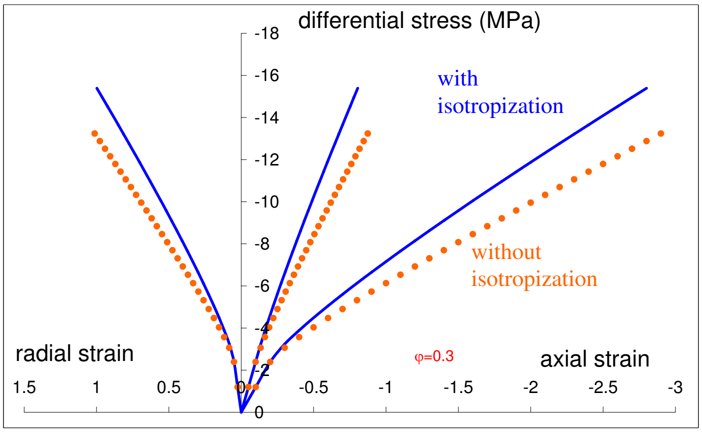

(b) Uniaxial compression test with $\varphi = 0.3$

Figure 1.10: Axial and lateral strains versus deviatoric stress curves in numerical uniaxial compression tests - comparison between predictions of first model with/without isotropization technique

1.5.2 Predictions by the second model

The proposed model in section 1.4 is now applied to simulate uniaxial compression tests. We still consider the same parameter values as before: $E_s = 3000MPa$, $\upsilon_s = 0.3$, $\tau_{cr} = 1.5MPa$, $K_n^{tan} \to \infty$.

1.5.2.1 Influence of interface imperfection

The predictions are obtained by applying different values of K_t^{tan}. In this case, K_t^{tan} reflects the degree of imperfection of interfaces. The effect is shown in Fig.1.11. It is seen that the more adherent the interface between grains is, the more ductile the macroscopic behavior becomes.

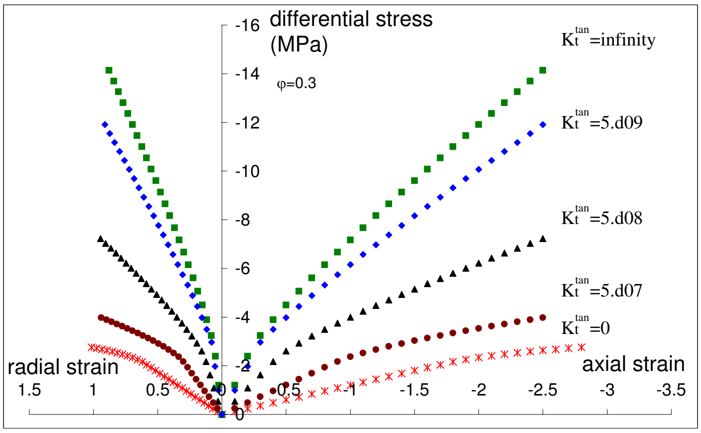

Figure 1.11: Axial and lateral strains versus deviatoric stress curves in uniaxial compression tests for different values of K_t^{tan} with $\varphi = 0.3$ (tangential tangent stiffness at the interface)

1.5.2.2 Simulation by considering two plastic mechanisms

Based on the above prediction, we found that the interface strongly affects the macroscopic behavior of the polycrystal. Now we aim at discussing the failure mechanism of the clay matrix by considering simultaneously the two plastic mechanisms yet introduced. Let us recall that the first mechanism is controlled by the Schmid failure criterion for grains which has been discussed in section 1.3. The second is a Tresca's failure criterion $\sigma_T < \sigma_{cr}$ for the tangential tangent stiffness of interfaces. The interface is considered to be failed once the value of critical stress σ_{cr} is reached in the tangential direction. The parameters $K_t^{tan} = 0$ is taken for the interface failure. i.e. The tangential stiffness of interfaces has a perfect plastic behavior described in Fig.1.12.

We must therefore seek for the maximal tangential stress value of $\{\sigma_T\}$, when all the orientations (θ_s, ϕ_s) are considered, at each loading step. The normal and tangential components

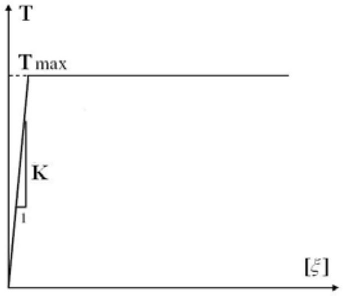

Figure 1.12: Perfect plasticity model of interface

of the stress $\boldsymbol{\sigma}^{\underline{N}}$ are defined as follows,

$$\begin{cases} \sigma_N = \underline{u}_r \cdot \boldsymbol{\sigma}^{\underline{N}} \cdot \underline{u}_r \\ \sigma_T = \boldsymbol{\sigma}^{\underline{N}} \cdot \underline{u}_r - \sigma_N \cdot \underline{u}_r \end{cases} \tag{1.69}$$

where $\underline{N}$ is the normal direction to the layers of the considered grain, and $\underline{u}_r = \sin\theta_s \cos\phi_s \underline{u}_1 + \sin\theta_s \sin\phi_s \underline{u}_2 + \cos\theta_s \underline{u}_3$ is a local arbitrary orientation vector on the external surface of grain and depending on the angles (θ_s, ϕ_s) defined in the local Cartesian coordinates system, $O\underline{u}_1\underline{u}_2\underline{u}_3$ of each grain.

According to (1.45),(1.64),(1.65), the average stress $\boldsymbol{\sigma}^{\underline{N}}$ of each family of oriented plastified grains at the $(n+1)^{th}$ loading step can be written as:

$$\boldsymbol{\sigma}^{\underline{N}}_{n+1}(\theta,\phi) = \boldsymbol{\sigma}^{\underline{N}}_{n}(\theta,\phi) + \triangle\, \overline{\boldsymbol{\sigma}}^{\underline{N}}_{n+1}(\theta,\phi) = \boldsymbol{\sigma}^{\underline{N}}_{n} + \mathbb{B}^{S\cup I}_{layer\,n+1}(\theta,\phi) : \dot{\mathbf{E}}_0 \tag{1.70}$$

And for isotropic grains, $\underline{N}$ is indifferent. According to (1.68), $\boldsymbol{\sigma}^{\underline{N}}_{n+1}$ reads:

$$\boldsymbol{\sigma}^{\underline{N}}_{n+1} = \boldsymbol{\sigma}^{\underline{N}}_{n} + \triangle\, \overline{\boldsymbol{\sigma}}^{\underline{N}}_{n+1} = \boldsymbol{\sigma}^{\underline{N}}_{n} + \mathbb{B}^{S\cup I}_{iso\ \, n+1} : \dot{\mathbf{E}}_0 \tag{1.71}$$

From (1.69) and (1.70) that the maximal tangential stress value of $\{\sigma_T\}$ is in function of (θ,ϕ). This means that the property of interface varies with the orientation of the laminated grain which it surrounds. Therefore, the value $\sup\{\sigma_T\}$ has been monitored and recorded in order to link the two mechanisms of grain and interface together with respect to the grain's orientation θ. Owing to the symmetry around the axis $\underline{e}_3$, the $\sup\{\sigma_T\} - \theta$ relation curves at each incremental loading are provided in Fig.1.13.

Accordingly, the $\sup\{\sigma_T\}$ are located at $\theta = 90^o$ and 0^o; and the $\inf\{\sigma_T\}$ at $\theta = 45^o$. It follows that the orientation distribution of crystals with intact or failed interface is provided in Fig.1.14(a), where the *Cone of intact interface* (white) will become smaller with the increasing

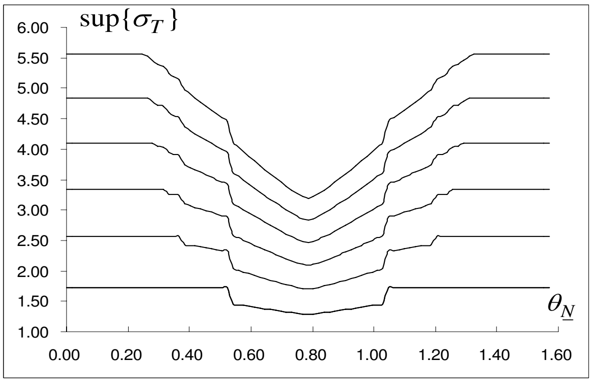

Figure 1.13: $\sup\{\sigma_T\} - \theta$ relation curves

of the load, until all the interfaces are plastified. By comparing Fig.1.14(a) to Fig.1.5, the scenario of the evolution of the two mechanisms function of θ is illustrated in Fig.1.14(b). The elastic limits of grain and interface divide the range $\theta \in [0, 90^o]$ into 5 different zones as follows:

zones 1 and 5 : elastic isotropic grains and failed interfaces

zones 2 and 4 : laminated grains and failed interfaces

zones 3 : laminated grains and intact interfaces

Based on the above discussions, the numerical simulations taking account simultaneously the two mechanisms has been performed by choosing the critical stress value of grains $\tau_{cr} = 1.5MPa$ and the value of interfaces $\sigma_{cr} = 1.5MPa$. It is assumed that $K_n^{tan} \to \infty$, $K_t^{tan} \to \infty$ when the interface is intact, and $K_n^{tan} \to \infty$, $K_t^{tan} = 0$ when the interface is failed. The comparison between predictions of the two different models is shown in Fig.1.15 for two porosities $\varphi = 0.2$ and $\varphi = 0.3$.

As expected, the curves predicted by the two models present great differences: i) the two predictions are identical in the elastic regime of the stress-strain curves where the interfaces are perfect; ii) a severe softening phenomenon occurs by considering the crushed interfaces; iii) in the second model, when the stress achieves a limit strength at the end of the stress-strain curves, where the tangent stiffness operator $\mathbb{L}$ attains to zero, the material failed. In summary, the stress-strain curve can be divided into three phases: an elastic regime, a plastic regime caused by plasticization of grain, and a softening regime due to the multiple deformation mechanisms of grains and in particular of interfaces. However, we found that the

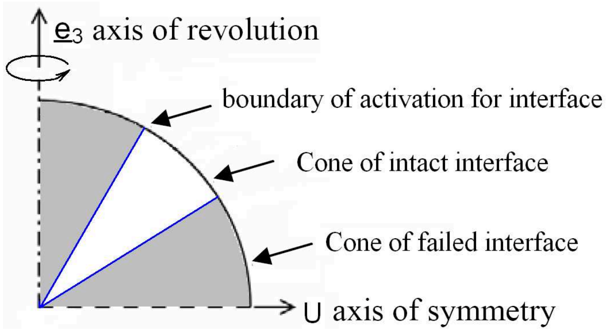

(a) Orientation distribution of intact and ruptured interfaces

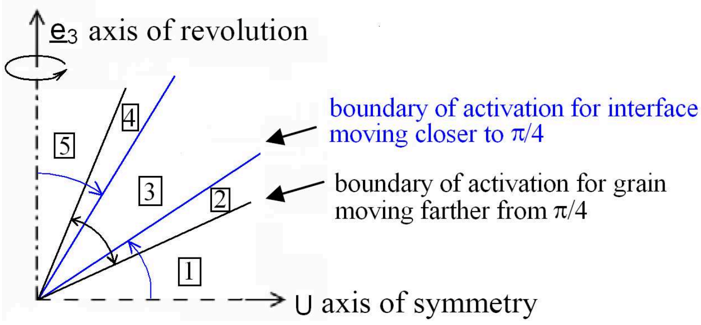

(b) Scenario of evolution of two mechanisms in function of θ

Figure 1.14: Orientation distribution of interfaces and scenario of evolution

model considering two plastic mechanisms produces irreversible contractancy in the softening domain due to a rearrangement of the material microstructure after shearing degradation of interfaces.

1.6 Conclusion

The transversely isotropic elastoplastic behavior of a porous polycrystal with damaging interfaces, such as clay matrix of an argillite, is investigated by means of a nonlinear homogenization approach. The formulation of the model is basically based on the microstructures and mechanisms identified in literatures. It was retained that the clay matrix can be considered as an assemblage of solid composite spheres and pores. The composite spheres are described as spherical sheet-like grains surrounded by interfaces (with displacement jumps) having an isotropic distribution of orientations. Intragranular slips between sheets and intergranular slips on interfaces are considered as the two local plastic mechanisms at the microscopic scale. Therefore we considered that the spherical sheet-like grain behaves as an

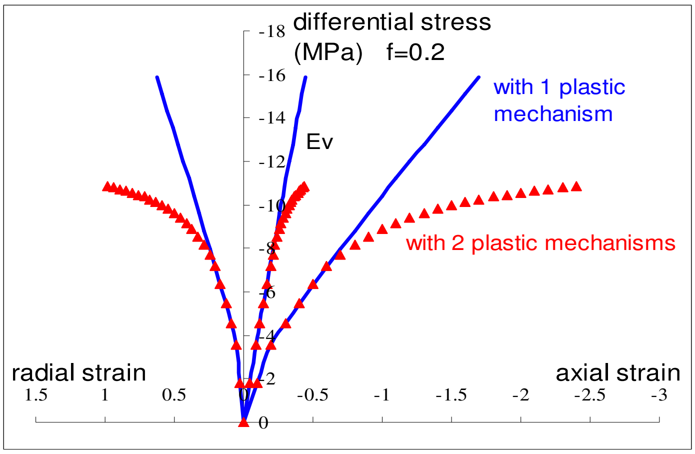

(a) Uniaxial compression test with $\varphi = 0.2$

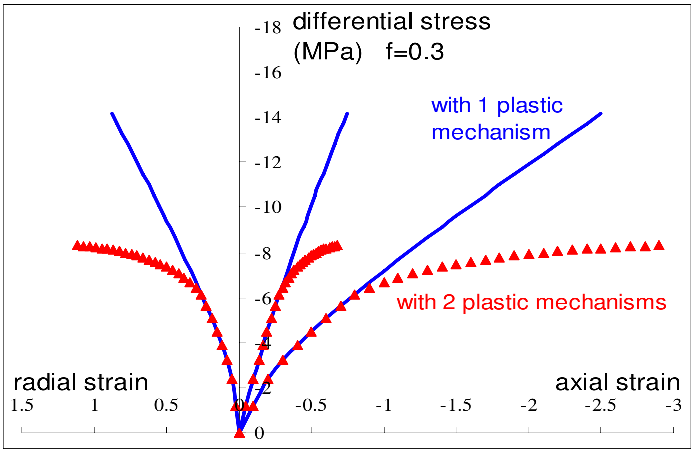

(b) Uniaxial compression test with $\varphi = 0.3$

Figure 1.15: Axial and lateral strains versus deviatoric stress curves in numerical uniaxial compression tests - comparison between predictions of first model (solid lines) and of second model

elastic isotropic medium when it is inactivated while it exhibits an anisotropic behavior when activated, the activation criterion is described by means of a Schmid law. A Tresca criterion is used for the interface strength.

Based on a rotated configuration of coordinate systems, in the framework of incremental approach, a first anisotropic formulation of self-consistent model which does not consider the interface effects is developed. To this end, the generalized Eshelby problem is revisited in order to incorporate the role of interfaces. Especially, an original numerical solution of laminated grains surrounded by interfaces is developed further. Appling this solution, a second self-consistent model which considers simultaneous evolution of the two local plastic mechanisms is also developed.

Finally, comparisons of numerical predictions of these two models are performed and have demonstrated the validity of the second proposed self-consistent model which takes account of the influence of interfaces. Numerical simulations of uniaxial compression tests allow showing that the macroscopic failure can not be explained only by single intragranular sheet-to-sheet slip mechanism. In contrast, the macroscopic elastoplastic behavior and failure have been successfully predicted by considering two local plastic mechanisms that take place simultaneously at microscopic scale. The corresponding scenario is described.

Appendix A

Three different conventions have been used to define the three Euler angles according to the resume summerized in [Zamiri et al.,07]. Thus, the crystal orientation Voigt matrix $Q(\theta,\phi,\psi)$ which is used to define the orientation of the crystal coordinates system with respect to the material co-rotational coordinates system can be written in three ways. Based on the Bunge system (see [Bunge,82]), the matrix can be defined by the three Euler angles φ_1,ϕ,φ_2 as:

$$Q\left(\varphi_1,\phi,\varphi_2\right)=$$
$$\begin{bmatrix} \cos\varphi_1\cos\varphi_2-\sin\varphi_1\sin\varphi_2\cos\phi & \sin\varphi_1\cos\varphi_2+\cos\varphi_1\sin\varphi_2\cos\phi & \sin\varphi_2\sin\phi \\ -\cos\varphi_1\sin\varphi_2-\sin\varphi_1\cos\varphi_2\cos\phi & -\sin\varphi_1\sin\varphi_2+\cos\varphi_1\cos\varphi_2\cos\phi & \cos\varphi_2\sin\phi \\ \sin\varphi_1\sin\phi & -\cos\varphi_1\sin\phi & \cos\phi \end{bmatrix} \tag{1.72}$$

Based on Kocks system [Kocks et al.,00], this matrix reads as dunction of Euler angles ϕ,Ψ,Θ as:

$$Q\left(\phi,\Psi,\Theta\right)=$$
$$\begin{bmatrix} -\sin\Psi\sin\phi-\cos\Psi\cos\phi\cos\Theta & \cos\Psi\sin\phi-\sin\Psi\cos\phi\cos\Theta & \cos\phi\sin\Theta \\ \sin\Psi\cos\phi-\cos\Psi\sin\phi\cos\Theta & -\cos\Psi\cos\phi-\sin\Psi\sin\phi\cos\Theta & \sin\phi\sin\Theta \\ \cos\Psi\sin\Theta & -\sin\Psi\sin\Theta & \cos\Theta \end{bmatrix} \tag{1.73}$$

The Roe system, the matrix leads to:

$$Q\left(\Psi,\phi,\theta\right)=$$
$$\begin{bmatrix} -\sin\Psi\sin\phi+\cos\Psi\cos\phi\cos\theta & \cos\Psi\sin\phi+\sin\Psi\cos\phi\cos\theta & -\cos\phi\sin\theta \\ -\sin\Psi\cos\phi-\cos\Psi\sin\phi\cos\theta & \cos\Psi\cos\phi-\sin\Psi\sin\phi\cos\theta & \sin\phi\sin\theta \\ \cos\Psi\sin\theta & \sin\Psi\sin\theta & \cos\theta \end{bmatrix} \tag{1.74}$$

Bibliography

[Abou-Chakra et al.,08] Abou-Chakra Guery A., et al., *A micromechanical model of elastoplastic and damage behavior of a cohesive geomaterial*, International Journal of Solids and Structures, **45** (2008), 1406–1429.

[Alberto Ortega et al.,07] Alberto Ortega J., Ulm F.-J, Abousleiman Y, *The effect of the nanogranular nature of shale on their poroelastic behavior*, Acta Geotechnica **2** (2007), 155–182.

[Andra,05] Andra, 2005. Referentiel du site meuse-haute marne. Report.

[Bunge,82] Bunge H.-J., *Texture analysis in materials science*, Butterworth, Reading, 1982.

[Berveiller et al.,79] Berveiller, Zaoui A., *An extension of the self-consistent scheme to plastically-flowing polycrystals*, J.Mech.Phys.Solids **26** (1979), 325-344.

[Bobko et al.,08] Bobko,C., Ulm F-J, *The nano-mechanical morphology of shale*, Mechanics of Materials **40** (2008), 318–337.

[Chiarelli et al.,03] Chiarelli A.S., Shao J.F., Hoteit N., *Modeling of elastoplastic damage behavior of a claystone*, International Journal of Plasticity **19** (2003), 23–45.

[Conil et al,03] Conil N., Djeran-Maigre I., Cabrillac R., Su K., *Poroplastic damage model for claystones*, Appl. Clay Sci. **26** (2004), 473–487.

[Dewhurst and siggins,06] Dewhurst DN, Siggins AF, *Impact of fabric, microcracks and stress field on shale anisotropy*, Geophys J. Int. **165** (2006), 135–148.

[Domnesteanu et al.,02] Domnesteanu P, McCann C, Sothcott J, *Velocity anisotropy and attenuation of shale in under- and overpressured conditions*, Geophys Prosp **50** (2002), 487–503.

[Dormieux et al.,06] Dormieux L., Kondo D., Ulm F.-J., *Microporomechanics*, Wiley, Reading, 2006.

[Dormieux et al.,07] Dormieux L., Sanahuja J., Maalej Y., *Strength of a polycrystal with imperfect intergranular interfaces*, Comptes Rendus Mecanique **335** (2007), 25–31.

[Dormieux et al.,10] Dormieux L., Jeannin L., Bemer E., et al., *Micromechanical models of the strength of a sandstone*, International Journal of Numerical and Analytical Methods in Geomechanics **34** (2010), 249–271.

[Draege et al,06] Draege A., Jakobsen M., Johansen T.A., *Rock physics modelling of shale diagenesis*, Petroleum Geoscience **12** (2006), 49–57.

[Eshelby,57] Eshelby J., *The determination of the elastic field of an ellipsoidal inclusion, and related problems*, Proc. R. Soc. Ser. **A241** (1957), 376–396.

[Fritsch et al.,07] Fritsch A., Dormieux L., Hellmich C., et al., *Micromechanics of crystal interfaces in polycrystalline solid phases of porous media: fundamentals and application to strength of hydroxyapatite biomaterials*, Journal of Materials Science **42** (2007), 8824–8837.

[Gavazzi and Lagoudas,90] Gavazzi A., Lagoudas D., *On the numerical evaluation of Eshelby's tensor and its application to elastoplastic fibrous composites*, Comp. Mech. **7** (1990), 13–19.

[Ghahremani,77] Ghahremani F., *Numerical evaluation of the stresses and strains in ellipsoidal inclusions in an anisotropic elastic material*, Mech. Res. Commun. **7** (1977),89–91.

[Hashin,91] Hashin Z., *The spherical inclusion with imperfect interface*, J. Appl. Mech. **58** (1991), 444–449.

[Hellmicha et al.,04] Hellmicha C., Barthelemy J-F., Dormieux L., *Mineral-collagen interactions in elasticity of bone ultrastructure-a continuum micromechanics approach*, European Journal of Mechanics-A/Solids **22** (2004), 783–810.

[Herve and Zaoui,93] Herve E.,Zaoui A., *n-Layered inclusion-based micromechanical modelling*, Internat. J. Engr. Sci. **31** (1993), 1–10.

[Hill,65] Hill R., *Continuum micro-mechanics of elastoplastic polycrystals*, J. Mech. Phys. Solids **13** (1965), 89–101.

[Hornby et al,94] Hornby B., Schwartz L.,Hudson J., *Anisotropic effective medium modeling of the elastic properties of shales*, Geophysics **59** (1994), 1570–1583.

[Hornby,98] Hornby B., *Experimental laboratory determination of the dynamic elastic properties of wet, drained shales*, Journal of Geophysical Research **103** (1998), 29945–29964.

[Jakobsen and Johansen.,00] Jakobsen M, Johansen TA, *Anisotropic approximations for mudrocks: A seismic laboratory study*, Geophysics **65** (2000), 1711–1725.

[Jones and Wang,94] Jones LEA., Wang HF., *Ultrasonic velocities in Cretaceous shales from the Williston basin*, Geophysics **46** (1994), 288–297.

[Kaarsberg,59] Kaarsberg E.A., *Introductory studies of natural and artificial argillaceous aggregates by sound-propagation and X-ray diffraction methods*, Journal of Geology **67** (1959), 447–472.

[Kocks et al.,00] Kocks U.F., Tome C.N., Wenk H.R., *Texture and Anisotropy*, Cambridge University Press, Reading, 2000.

[Kroner,78] Kroner E., *Self-consistent scheme and graded disorder in polycrystal elasticity*, Journal of Physics F-Metal Physics**8** (1978), 2261–2267.

[Love,44] Love A.E.H., *A treatise on the mathematical theory of elasticity*, Dover, Reading, New-York, 1944.

[Maalej et al.,09] Maalej Y., Dormieux L., Sanahuja J., *Micromechanical approach to the failure criterion of granular media*, European Journal of Mechanics A-Solids **28** (2009), 647–653.

[Ponte Castaneda et al.,98] Ponte Castaneda P., Suquet P., *Nonlinear composites*, Adv. Appl. Mech. **34** (1998), 171–302.

[Robinet,08] Robinet, J., 2008. *Mineralogie Porosite et diffusion des solutes dans l'argilite du callovo-oxfordien de bure (meuse/haute-marne, france) de l'echelle centimetrique a micrometrique*, Phd.thesis, Universite de poitiers, France.

[sammartino,01] Sammartino G., *Construction d'un model conceptual d'organisation de la porosite de la mineralogie des argilites du site de bure*, Rapport Andra DRP0ERM01-018/A, Rapport final, 2001.

[Sanahuja,08] Sanahuja J., *Impact de la morphologie structurale sur les performances mecaniques des materiaux de construction: application au platre et a la pate de ciment*, These de doctorat, 2008.

[Sayers,94] Sayers C.M., *The elastic anisotropy of shales*, Journal of Geophysical Research **99** (1994), 767–774.

[Sayers,99] Sayers C.M., *Stress-dependent seismic anisotropy of shales*, Geophysics **64** (1999), 93–98.

[Shen et al.,12] Shen W.Q., Shao J.F., Kondo D., and Gatmiri B., *A micro-macro model for clayey rocks with a plastic compressible porous matrix*, International Journal of Plasticity, 36, (2012) 64–85.

[Suquet et al.,97] Suquet P., Tome C.N., Wenk H.R., *Effective behavior of non linear composites, In Continuum Micromechanics*, Springer, Reading, Berlin, 1997.

[Tandon et al.,88] Tandon G.P., Weng G.J., *A theory of particle-renforced plasticity*, J.Appl. Mech. **55** (1988), 126–135.

[Ulm et al.,05] Ulm F.-J., Constantinides, G., Delafargue, A.,Abousleiman, Y.,Ewy, R., Duranti, L., McCarty, D.K., *Material invariant poromechanics properties of shales*, 3rd Biot Conference on Poromechanics (Norman, Oklahoma, USA.2005), Balkema Publishers, London, 2005, pp. 37–644.

[Withers,89] Withers P.J., *The determination of the elastic field of an ellipsoidal inclusion in a transversely isotropic medium and its relevance to composite materials*, Philosophical Magazine A **59** (1989), 759–781.

[Zamiri et al.,07] Zamiri A., Pourboghrat F., Barlat F., *An effective computational algorithm for rate-independent crystal plasticity based on a single crystal yield surface with an application to tube hydroforming*, International Journal of Plasticity **23** (2007), 1126–1147.

[Zaoui,02] Zaoui A., *Continuum micromechanics: survey*, Journal of Engineering Mechanics **128** (2002), 808–816.

Chapter 2

Poroelastic model for granular materials with interface effect

Contents

Rappels du contenu

Divers matériaux rencontrés dans le domaine du génie civil sont constitués de grains en interaction avec un autre le long de leurs interfaces. L'objectif du présent chapitre est de formuler dans un cadre micromécanique un modèle linéaire poro-élastique pour milieux granulaires saturés, et ayant des interfaces imparfaites. L'espace poreux est rempli par un fluide à une pression uniforme p. La théorie classique de poro-élasticité linéaire [Biot,41], [Coussy,95] introduit une équation d'état impliquant deux paramètres poroélastiques: le tenseur du second ordre de Biot $\mathbb{B}$ et le module de Biot N.

Le présent chapitre fournit un cadre d'interprétation microscopique des constantes poroélastiques. Ensuite, en restant dans ce cadre 'micro-macro', l'estimation auto-cohérente de $\mathbb{B}$ et N sont dérivées de la solution à un problème d'Eshelby généralisé incorporant deux caractéristiques spécifiques: couches minces molles entourant les grains rigides et pression interstitielle dans l'espace des pores. En définitive, on montre que les constantes poroélastiques pour les matériaux granulaires avec effets d'interface s'écrivent:

$$b = 1 - \frac{3k^{eff}}{2K_n d} \quad ; \quad \frac{1}{N} = \frac{3}{2}\frac{b-f}{K_n d} \tag{2.1}$$

où K_n est le coefficient de raideur normale d'interface, d le rayon des grains sphériques.

De plus, il a été établi que le comportement homogénéisé peut être obtenu en remplaçant la morphologie hétérogène 'grain + interface' par une inclusion homogène équivalente. Ce résultat est prometteur en vue d'une dérivation des comportements non-linéaires ou des résistances mécaniques des matériaux granulaires avec des effets d'interface. Le module volumique 'équi-valent' k^s_{eq} étant alors défini comme:

$$k^s_{eq} = \frac{2}{3}K_n d \tag{2.2}$$

et le module de cisaillement 'équivalent' μ^s_{eq}:

$$\frac{\mu^s_{eq}}{K_n d} = \begin{cases} \dfrac{2(1-3f)}{8-15f}(1+\rho\,\eta(f)) & 0 < f < 1/3 \quad (a) \\ \dfrac{3-f}{3(3f-1)}\rho & 1/3 < f < 1/2 \quad (b) \end{cases} \tag{2.3}$$

où $\eta(f) = \dfrac{3}{2}\dfrac{(2-3f)^2(45f^2-87f+32)}{(4-3f)(8-15f)(1-3f)^2}$, et $\rho = \dfrac{K_t}{K_n} \to 0$

Ce chapitre a fait l'objet d'une publication parue dont les références sont aux suivants

2.1 introduction

Various materials encountered in civil engineering are made up of grains interacting with one another along their interfaces. The contact between two grains is not perfect in the sense that a significant part of the overall strain of a representative elementary volume (r.e.v.) corresponds to the relative displacements between grains in contact (intergranular part), while the other contribution to the effective strain is related to the intragranular part. Hence, the effective mechanical properties are strongly affected by those of these interfaces.

The contact on the interfaces between grains can be described by a 2D geometrical model. In this case, the constitutive equation relates the stress vector acting on the surface and the displacement jump accross the surface. Alternatively, the contact zone can be represented by a thin interphase layer with an appropriate 3D description of the mechanical properties. The quantitative link between 2D and 3D model parameters was discussed by [Benveniste and Miloh,01] and [Hashin,02]. Qualitatively, the relative displacement between two grains is the 2D counterpart of large strains concentrated in a thin 3D interphase.

In view of the micromechanical description of a granular material, the self-consistent scheme ([Kroener,78],[Zaoui,02]) generally used for polycrystals is an appealing candidate. Still it must be extended in order to capture the mechanical impact of the interfaces. As opposed to the classical self-consistent scheme in which perfect contact between elementary crystals is assumed, the extended scheme is based on the solution to a generalized Eshelby problem: A composite particle made up of the grain surrounded by an interface is embedded in an infinite space having the mechanical properties of the sought homogenized material. [Hashin,02] described this approach and implemented it in view of application to coated fibers. Adopting a spherical model for the grains, a number of papers have been devoted to the micromechanical modelling of granular materials including the determination of the effective linear and non linear elastic properties [Maalej et al.,07] and the effective strength [Dormieux et al.,07], [Maalej et al.,09], [Dormieux et al.,10].

The purpose of the present paper is to derive a linear poroelastic model for fluid-saturated granular media with imperfect interfaces. The pore space which is a complementary phase with respect to the solid is filled by a fluid at a uniform pressure p. As compared to standard linear elasticity, the classical theory of linear poroelasticity (see e.g. [Coussy,95]) introduces an additional state equation. The first one states that the strain tensor $\mathbf{E}$ is controlled by a so-called effective stress, which is a linear combination of the stress tensor $\boldsymbol{\Sigma}$ and of the fluid pressure p. The second one gives the normalized pore volume change v as a linear function of strain and pressure. Hence, in addition to the effective stiffness tensor $\mathbb{C}^{eff}$, linear poroelasticity introduces two new material parameters, namely the so-called Biot (second order) tensor $\mathbf{B}$ and the Biot modulus N:

$$\begin{aligned} \boldsymbol{\Sigma} + p\mathbf{B} &= \mathbb{C}^{eff} : \mathbf{E} \\ v &= \frac{p}{N} + \mathbf{B} : \mathbf{E} \end{aligned} \tag{2.4}$$

The micromechanical approach to poroelasticity provides an alternative theoretical framework for the derivation of the state equations (2.4). Besides, it relates the poroelastic constants to the microscopic behavior of the solid skeleton (see e.g. [Tompson and Willis,91], [Dormieux et al.,02], [Dormieux et al.,06]). Furthermore, the classical Eshelby-based schemes can be extended in order to derive quantitative estimates of $\mathbf{B}$ and N. In particular, when the solid phase is a homogeneous solid with stiffness tensor $\mathbb{C}^s$, the poroelastic constants are directly related to $\mathbb{C}^s$ and $\mathbb{C}^{eff}$:

$$\begin{aligned} \mathbf{B} &= \mathbf{1} - \mathbb{C}^{eff} : \mathbb{C}^{s-1} : \mathbf{1} \\ \frac{1}{N} &= \mathbf{1} : \mathbb{C}^{s-1} : (\mathbf{B} - f\mathbf{1}) \end{aligned} \tag{2.5}$$

where f is the porosity, that is, the volume fraction of the pore space. In the isotropic case, $\mathbf{B}$ is a spherical tensor ($\mathbf{B} = b\mathbf{1}$). Introducing the bulk moduli k^{eff} and k^s of the effective material and of the solid, (2.5) reduce to

$$b = 1 - \frac{k^{eff}}{k^s} \quad ; \quad \frac{1}{N} = \frac{b-f}{k^s} \tag{2.6}$$

(2.5) means that it suffices to determine the effective stiffness tensor $\mathbb{C}^{eff}$. Since the later characterizes the elastic properties of the dry material, this can be achieved with standard homogenization techniques (no fluid-solid coupling).

In contrast, the present paper deals with a strongly heterogeneous solid material due to imperfect interfaces between the grains. First, the microscopic interpretation of the poroelastic constants is recalled. In this framework, self-consistent estimates of $\mathbf{B}$ and N are derived from the solution to a generalized Eshelby problem incorporating two specific features: thin soft layers surrounding stiff grains and pore pressure in the pore space.

2.2 Micromechanical definition of the poroelastic constants

The granular material at stake comprises a solid phase and a pore space. The solid phase itself is made up of discrete stiff grains (stiffness tensor $\mathbb{C}_g$) in mechanical interaction with one another. Following [Hashin,02], it is possible to resort to the 2D (interface) or 3D (interphase) model of the contact zone between grains. In the 2D model, the stress vector $\mathbf{T}$ acting on grain G_i at the contact surface Γ_{ij} between grains G_i and G_j is linearly related to the displacement jump $[\![\boldsymbol{\xi}]\!]$ accross the contact surface :

$$\mathbf{T} = \mathbf{K} \cdot [\![\boldsymbol{\xi}]\!] \quad ; \quad [\![\boldsymbol{\xi}]\!] = \boldsymbol{\xi}_j - \boldsymbol{\xi}_i \tag{2.7}$$

where the stiffness tensor $\mathbf{K}$ of the interface reads:

$$\mathbf{K} = K_n \mathbf{n} \otimes \mathbf{n} + K_t(\mathbf{1} - \mathbf{n} \otimes \mathbf{n}) \tag{2.8}$$

where K_n and K_t denote the normal and tangential stiffness coefficients of the interface. In turn, in the 3D model, the interphase is a thin layer with thickness h, made up of an isotropic (soft) solid with bulk and shear moduli k_{int} and μ_{int}. The 3D model is asymptotically equivalent to the 2D model when $h \to 0$ provided that k_{int} and μ_{int} are proportional to h and related to the surface constants by [Hashin,02]:

$$k_{int} = h(K_n - \frac{4}{3}K_t) \quad ; \quad \mu_{int} = hK_t \tag{2.9}$$

With the usual fourth-order projectors $\mathbb{J}$ and $\mathbb{K}$, the stiffness tensor in the interphase reads $\mathbb{C}_{int} = 3k_{int}\mathbb{J} + 2\mu_{int}\mathbb{K}$. The stiffness contrast between the interphase and the grain formally reads $\mathbb{C}_{int} : \mathbb{C}_g^{-1} \ll \mathbb{I}$, where $\mathbb{I}$ is the fourth-order symmetric identity tensor. More precisely, d denoting the characteristic grain size, and introducing $\delta = h/d$, it is assumed that $\mathbb{C}_{int} : \mathbb{C}_g^{-1} = O(\delta)\mathbb{I}$.

Let $\Gamma = \cup_{i,j}\Gamma_{ij}$ (resp. $\mathcal{G} = \cup_i G_i$) denote the soft (resp. stiff) part of the solid phase in the r.e.v. Ω and let $\mathcal{P}$ denote the fluid-saturated pore space: $\Omega = \Gamma \cup \mathcal{G} \cup \mathcal{P}$. The loading applied to Ω is defined by the pore pressure p and by uniform strain boundary conditions on the displacement field on the boundary $\partial\Omega$:

$$(\forall \mathbf{z} \in \partial\Omega) \quad \boldsymbol{\xi}(\mathbf{z}) = \mathbf{E} \cdot \mathbf{z} \tag{2.10}$$

Interestingly, the microscopic stress field $\boldsymbol{\sigma}$ is related to the microscopic strain field $\boldsymbol{\varepsilon}$ by:

$$\boldsymbol{\sigma}(\mathbf{z}) = \mathbb{C}(\mathbf{z}) : \boldsymbol{\varepsilon}(\mathbf{z}) + \boldsymbol{\sigma}^p(\mathbf{z}) \tag{2.11}$$

with

$$\begin{array}{lll} \mathbf{z} \in \mathcal{G}: & \mathbb{C}(\mathbf{z}) = \mathbb{C}_g & ; \quad \boldsymbol{\sigma}^p(\mathbf{z}) = 0 \\ \mathbf{z} \in \Gamma: & \mathbb{C}(\mathbf{z}) = \mathbb{C}_{int} & ; \quad \boldsymbol{\sigma}^p(\mathbf{z}) = 0 \\ \mathbf{z} \in \mathcal{P}: & \mathbb{C}(\mathbf{z}) = 0 & ; \quad \boldsymbol{\sigma}^p(\mathbf{z}) = -p\mathbf{1} \end{array} \tag{2.12}$$

In the dry case $p = 0$, the only parameter is the macroscopic strain $\mathbf{E}$ and the microscopic strain field linearly depends on $\mathbf{E}$ which is expressed through the fourth-order strain concentration tensor $\mathbb{A}$:

$$\boldsymbol{\varepsilon}(\mathbf{z}) = \mathbb{A}(\mathbf{z}) : \mathbf{E} \tag{2.13}$$

When the only parameter is the pore pressure p (case $\mathbf{E} = 0$), the microscopic strain field now linearly depends on p which is expressed through the second-order strain concentration tensor $\mathbf{a}$:

$$\boldsymbol{\varepsilon}(\mathbf{z}) = p\mathbf{a}(\mathbf{z}) \tag{2.14}$$

In the general case $(p, \mathbf{E} \neq 0)$, the macroscopic counterpart of (2.11) reads:

$$\boldsymbol{\Sigma} = \mathbb{C}^{eff} : \mathbf{E} + \boldsymbol{\Sigma}^p \tag{2.15}$$

with

$$\mathbb{C}^{eff} = \overline{\mathbb{C} : \mathbb{A}} \quad ; \quad \boldsymbol{\Sigma}^p = \overline{\boldsymbol{\sigma}^p : \mathbb{A}} \tag{2.16}$$

where $\overline{a}$ (resp. $\overline{a}^{\mathcal{D}}$) denote the volume average on Ω (resp. on the domain $\mathcal{D} \subset \Omega$). Comparing (2.15)-(2.16) with the first equation of (2.4) yields the following micromechanical interpretation of Biot tensor $\mathbf{B}$:

$$\mathbf{B} = f\mathbf{1} : \overline{\mathbb{A}}^{\mathcal{P}} \tag{2.17}$$

In turn, considering the second equation of (2.4) and (2.14) yields the following micromechanical interpretation of Biot modulus N:

$$\frac{1}{N} = f\mathbf{1} : \overline{\mathbf{a}}^{\mathcal{P}} \tag{2.18}$$

Note that (2.17) and (2.18) are valid irrespective of the selected homogenization scheme. However, in order to derive quantitative estimates of $\mathbf{B}$ and N, a homogenization scheme is due.

2.3 self-consistent estimates of the poroelastic constants

2.3.1 description of the generalized self-consistent scheme with composite sherical inclusion

The classical self-consistent scheme for porous media consists in representing each phase by a spherical inclusion embedded in an infinite space with remote boundary conditions on the displacemnt at infinity. The stiffness of the later is the unknown effective stiffness (tensor $\mathbb{C}^{eff}$). The "real" average stress and strain states in each phase is estimated from the uniform strain and stress states in the corresponding inclusion.

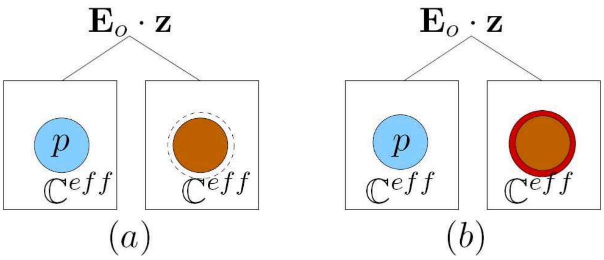

Figure 2.1: generalized self-consistent scheme (GSCS): (a) composite inclusion with 2D-interface; (b) composite inclusion with 3D-interphase

In order to capture the mechanical role of the intergranular contact zone in a generalized self-consistent scheme, the idea is to represent the heterogeneous solid phase $\mathcal{S} = \mathcal{G} \cup \Gamma$ by a composite sphere. As in the classical scheme, the pore space is represented by a (possibly) pressurized spherical cavity (see figure 2.1). As far as the solid phase is concerned, there are two equivalent models. If the interphase model is adopted, the composite sphere is a homogeneous sphere (radius d) with stiffness $\mathbb{C}_g$ surrounded by a layer with stiffness $\mathbb{C}_{int}$ and thickness $h/2$ (half of the total thickness of the "real" interphase in the r.e.v.). In turn, if the interface model is adopted, the composite sphere is made up of the same homogeneous sphere (radius d, stiffness $\mathbb{C}_g$) surrounded by an interface with normal and tangential stiffness coefficients $K'_n = 2K_n$ and $K'_t = 2K_t$. The origin of the factor 2 between the stiffness of the interface in the composite sphere and that of the "real" intergranular interface in the r.e.v. (see (2.7)) is discussed in [Maalej et al.,09]. Clearly, it is the 2D counterpart of the thickness $h/2$ selected in the 3D interphase model.

In order to implement the GSC scheme sketched at figure 2.1, the solutions to the corresponding Eshelby-type problems must be derived. With uniform strain boundary conditions of the form $\boldsymbol{\xi} = \mathbf{E}_o \cdot \mathbf{z}$ at infinity, the solution to the pressurized cavity problem classically reads (see e.g. [Dormieux et al.,06]):

$$\boldsymbol{\varepsilon}^{cav} = (\mathbb{I} - \mathbb{P} : \mathbb{C}^{eff})^{-1} : (\mathbf{E}_o + p\mathbb{P} : \mathbf{1}) \tag{2.19}$$

$\mathbb{P}$ here denotes the Hill tensor of the sphere for the material with stiffness $\mathbb{C}^{eff}$. In turn, focusing on the 2D interface model, the equations of the corresponding generalized Eshelby problem read:

$$\begin{array}{ll} r < d: & \boldsymbol{\sigma} = \mathbb{C}_g : \varepsilon \\ r = d: & \boldsymbol{\sigma} \cdot \mathbf{n} = \mathbf{K}' \cdot [\boldsymbol{\xi}] \\ r > d: & \boldsymbol{\sigma} = \mathbb{C}^{eff} : \varepsilon \\ r \rightarrow \infty: & \boldsymbol{\xi} = \mathbf{E}_o \cdot \mathbf{z} \end{array} \tag{2.20}$$

where $[\boldsymbol{\xi}] = \boldsymbol{\xi}(d^+) - \boldsymbol{\xi}(d^-)$ denotes the displacement discontinuity across the sphere boundary $r = d$ in the auxiliary Eshelby problem. Unlike the cavity, the strain field is not homogeneous in the composite sphere. The average strain and the average stress in the composite sphere take the form of integrals over the external face $(r = d^+)$ of the composite sphere. Both are linearl functions of $\mathbf{E}_o$:

$$\boldsymbol{\varepsilon}^{CS} = \frac{3}{4\pi d^3} \int_{r=d} \boldsymbol{\xi}(d^+) \overset{s}{\otimes} \mathbf{e}_r \, dS = \mathbb{L} : \mathbf{E}_o \tag{2.21}$$

$$\boldsymbol{\sigma}^{CS} = \frac{3}{4\pi d^2} \int_{r=d} \mathbf{e}_r \otimes \boldsymbol{\sigma}(d) \cdot \mathbf{e}_r \, dS = \mathbb{D} : \mathbf{E}_o \tag{2.22}$$

where $\mathbb{L}$ and $\mathbb{D}$ are fourth-order tensors which depend on $\mathbb{C}_g$, $\mathbf{K}'$ and $\mathbb{C}^{eff}$.

In the line of reasoning of the self-consistent scheme, $\boldsymbol{\varepsilon}^{cav}$ and $\boldsymbol{\varepsilon}^{CS}$ are respectively adopted as estimates of the average strain in the pore space and in the heterogeneous solid:

$$\overline{\boldsymbol{\varepsilon}}^{\mathcal{P}} = \boldsymbol{\varepsilon}^{cav} \quad ; \quad \overline{\boldsymbol{\varepsilon}}^{\mathcal{S}} = \boldsymbol{\varepsilon}^{CS} \tag{2.23}$$

Accordingly, the strain average rule $\overline{\boldsymbol{\varepsilon}} = \mathbf{E}$ clarifies the relationship between the auxiliary strain tensor $\mathbf{E}_o$ and the actual loading parameters $\mathbf{E}$ and p:

$$\mathbf{E}_o = \left(f(\mathbb{I} - \mathbb{P} : \mathbb{C}^{eff})^{-1} + (1-f)\mathbb{L} \right)^{-1} : \left(\mathbf{E} - pf(\mathbb{I} - \mathbb{P} : \mathbb{C}^{eff})^{-1} : \mathbb{P} : \mathbf{1} \right) \tag{2.24}$$

Furthermore, $\boldsymbol{\sigma}^{CS}$ is adopted as an estimate of the average stress in the heterogeneous solid:

$$\overline{\boldsymbol{\sigma}}^{\mathcal{P}} = -p\mathbf{1} \quad ; \quad \overline{\boldsymbol{\sigma}}^{\mathcal{S}} = \boldsymbol{\sigma}^{CS} \tag{2.25}$$

According to (2.17), the Biot tensor $\mathbf{B}$ is derived from $\overline{\varepsilon}^{\mathcal{P}}$ in the dry case $p = 0$. Similarly, according to (2.18), the Biot modulus N is derived from $\overline{\varepsilon}^{\mathcal{P}}$ in the case $\mathbf{E} = 0$. Introducing (2.24) into (2.19) and recalling (2.23) successively yields:

$$\mathbf{B} = f\mathbf{1} : (\mathbb{I} - \mathbb{P} : \mathbb{C}^{eff})^{-1} : \Big(f(\mathbb{I} - \mathbb{P} : \mathbb{C}^{eff})^{-1} + (1-f)\mathbb{L}\Big)^{-1} \tag{2.26}$$

and

$$\frac{1}{N} = f(\mathbf{1} - \mathbf{B}) : \Big((\mathbb{I} - \mathbb{P} : \mathbb{C}^{eff})^{-1} - \mathbb{I}\Big) : \mathbb{C}^{eff^{-1}} : \mathbf{1} \tag{2.27}$$

Practical use of these estimates requires $\mathbb{C}^{eff}$ and $\mathbb{L}$ to be determined.

2.3.2 Practical implementation of the self-consistent scheme

Using (2.25) with (2.22) in the stress average rule yields:

$$\begin{aligned}\mathbf{\Sigma} = \;& -fp\mathbf{1} + (1-f)\mathbb{D} : \big(f(\mathbb{I} - \mathbb{P} : \mathbb{C}^{eff})^{-1} + (1-f)\mathbb{L}\big)^{-1} : (\mathbf{E} \\ & -pf(\mathbb{I} - \mathbb{P} : \mathbb{C}^{eff})^{-1} : \mathbb{P} : \mathbf{1}\big)\end{aligned} \tag{2.28}$$

The comparison with the first equation of (2.4) first provides an implicit equation which characterizes the self-consistent estimate of $\mathbb{C}^{eff}$:

$$\mathbb{C}^{eff} = (1-f)\mathbb{D} : \Big(f(\mathbb{I} - \mathbb{P} : \mathbb{C}^{eff})^{-1} + (1-f)\mathbb{L}\Big)^{-1} \tag{2.29}$$

where $\mathbb{L}$ and $\mathbb{D}$ have been introduced in (2.21) and (2.22). In view of the practical implementation of (2.29), we now assume that the solid grain stiffness $\mathbb{C}_g$ is an isotropic tensor. This implied that $\mathbb{C}^{eff}$ as well as $\mathbb{L}$ and $\mathbb{D}$ are isotropic tensors as well. In this framework, analytical expressions of these tensors can be readily derived from [Herve and Zaoui,93] and (2.29) proves to be strictly equivalent to the condition

$$\Big(f(\mathbb{I} - \mathbb{P} : \mathbb{C}^{eff})^{-1} + (1-f)\mathbb{L}\Big) = \mathbb{I} \tag{2.30}$$

In other words, the self-consistent estimate of $\mathbb{C}^{eff}$ can be determined from the solution to either (2.29) or (2.30). This generalizes to the case of a composite solid inclusion a well-known property of the classical self-consistent scheme (see appendix, equation (2.46)).

The second corollary of (2.28) is an alternative expression of the Biot tensor, denoted by $\mathbf{B}'$:

$$\mathbf{B}' = f(\mathbf{1} + \mathbb{C}^{eff} : (\mathbb{I} - \mathbb{P} : \mathbb{C}^{eff})^{-1} : \mathbb{P} : \mathbf{1}) \tag{2.31}$$

which can be put in the form:

$$\mathbf{B}' = f\mathbb{C}^{eff} : (\mathbb{I} - \mathbb{P} : \mathbb{C}^{eff})^{-1} : \mathbb{C}^{eff^{-1}} : \mathbf{1} \tag{2.32}$$

Furthermore, using the isotropy assumption, (2.32) simplifies into:

$$\mathbf{B}' = f(\mathbb{I} - \mathbb{P} : \mathbb{C}^{eff})^{-1} : \mathbf{1} \tag{2.33}$$

In the general case, the above expression is a priori formally different from (2.26) previously derived from the average theorem (2.16). This is not surprising since, even in the classical self-consistent scheme, specific conditions are required for the consistency of the classical self-consistent scheme with the average theorem (2.16) to be satisfied (see [Pichler and Dormieux,08]). However, introducing (2.30) into (2.26) proves that $\mathbf{B} = \mathbf{B}'$ when the solid grain is isotropic.

2.3.3 analytical estimates

Analytical solutions can be derived in the limit case of a rigid solid ($\mathbb{C}_g \to \infty$). In this case, it is convenient to introduce the ratio $\rho = K_t/K_n$ and to normalize the effective bulk and shear moduli by $K_n d$. Let $M = \mu^{eff}/K_n d$ and $K = k^{eff}/K_n d$. Considering successively the spherical and the deviatoric part of (2.29) yields:

$$K = \frac{4(1-f)M}{3(2M+f)} \quad \text{with} \quad K = \frac{k^{eff}}{K_n d} \quad \text{and} \quad M = \frac{\mu^{eff}}{K_n d} \tag{2.34}$$

and

$$16M^3 + 4(3f + 2 + 2\rho(3f-1))M^2 + (3(3f-1) + 2\rho(12f-5))M + 3\rho(2f-1) = 0 \tag{2.35}$$

The (spherical) Biot tensor takes the form $b\mathbf{1}$. The expression of the Biot coefficient is derived from (2.33) and (2.34) with (2.48):

$$b = 1 - \frac{3K}{2} = 1 - \frac{3k^{eff}}{2K_n d} \tag{2.36}$$

Similarly, (2.27) yields:

$$\frac{1}{N} = \frac{3}{2}\frac{b-f}{K_n d} \tag{2.37}$$

2.4 The equivalent homogeneous solid

In this section, we further adopt the assumption of rigid grains. It is instructive to compare (2.36) and (2.37) to (2.6). The formal analogy suggests to introduce an "equivalent" bulk modulus k^s_{eq} for the heterogeneous solid phase $\mathcal{S}$ defined as:

$$k^s_{eq} = \frac{2}{3} K_n d \tag{2.38}$$

If one goes further on this line of reasoning, the question arises whether it is possible to replace the heterogeneous solid phase $\mathcal{S}$ by an "equivalent" homogeneous and isotropic one in the sense that the homogenized stiffness $\mathbb{C}^{eff}$ characterized by (2.34) and (2.35) and the poroelastic constants b and N are preserved. If this fictitious homogeneous solid phase exists, we have already seen that its bulk modulus is necessarily equal to k^s_{eq} given by (2.38). We now seek an appropriate shear modulus μ^s_{eq} for which the equivalence as defined above can be achieved. We shall of course consider this question in the framework of the self-consistent scheme. In other words, we replace the composite sphere in figure 2.1 by a homogeneous sphere with stiffness $\mathbb{C}^s_{eq} = 3k^s_{eq}\mathbb{J} + 2\mu^s_{eq}\mathbb{K}$. The sought value of μ^s_{eq}, if it exists, is the one for which identical estimates of $\mathbb{C}^{eff}$, b and N are derived. Because of the definition (2.38) of k^s_{eq}, note that it is sufficient to focus on the equivalence in terms of homogenized stiffness. The equivalence as regards b and N is a corollary of (2.36) and (2.37).

Since this supposedly equivalent material is homogeneous, the self-consistent scheme now reduces to the classical one, described at section 2.5.1. More specifically, we now deal with a 2-phase composite, made up of a pore space with vanishing stiffness and a solid phase with stiffness $\mathbb{C}^s_{eq}$. Both the porous and the solid phases are geometrically represented by spherical inclusions. As a consequence, these two phases are associated with the same Hill tensor $\mathbb{P}$ defined by (2.48). Combining (2.46) and (2.47) yields the following relation:

$$\mathbb{C}^s_{eq} = \mathbb{C}^{eff} : \left(\mathbb{I} - f\left(\mathbb{I} - \mathbb{P} : \mathbb{C}^{eff}\right)^{-1}\right)^{-1} \tag{2.39}$$

Taking advantage of (2.48), (2.39) reduces to:

$$\left\{\begin{array}{l} k^s_{eq} = \dfrac{4\mu^{eff} k^{eff}}{4\mu^{eff}(1-f) - 3f k^{eff}} \\ \mu^s_{eq} = \dfrac{(9k^{eff} + 8\mu^{eff})\mu^{eff}}{4(2-5f)\mu^{eff} + 3(3-5f)k^{eff}} \end{array}\right. \tag{2.40}$$

Using (2.34) in the above expression of k^s_{eq}, the definition (2.38) is retrieved. Furthermore, the following determination of the equivalent shear modulus is obtained:

$$\mu^s_{eq} = K_n\, d\, \frac{M\,(4M+3-f)}{3(1-2f)+2(2-5f)M} \tag{2.41}$$

where $M(f,\rho)$ is the real (physical) solution of (2.35). The latter may be derived from Cardan's method (see 2.5.2). This eventually confirms the existence of an equivalent material in terms of stiffness and poroelastic constants and provides its definition through (2.38) and(2.41)) . This original result opens the door to a new systematic approach for the poromechanics behavior of granular materials with interface effects.

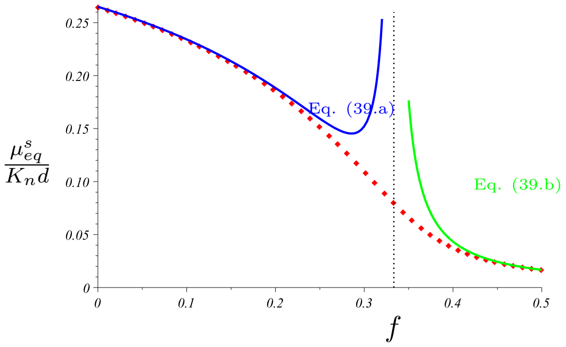

Figure 2.2: equivalent shear modulus vs. pore volume fraction ($\rho = 10^{-2}$)

Application In practice, numerous studies evoke the weakness of the tangential stiffness as compared to the normal stiffness. This amounts to assuming that $\rho = K_t/K_n \ll 1$. Within the framework of the equivalent solid phase previously derived, while (2.38) is still valid, it requires the Taylor expansion of (2.41) at $\rho = 0$:

$$\frac{\mu^s_{eq}}{K_n d} = \begin{cases} \frac{2(1-3f)}{8-15f}\,(1+\rho\,\eta(f)) & 0<f<1/3 \quad (a) \\ \frac{3-f}{3(3f-1)}\rho & 1/3<f<1/2 \quad (b) \end{cases} \tag{2.42}$$

where $\eta(f) = \dfrac{3}{2}\,\dfrac{(2-3f)^2(45f^2-87f+32)}{(4-3f)(8-15f)(1-3f)^2}$.
Then, application of the classical self-consistent scheme for a 2-phase composite, made up of a pore space with vanishing stiffness and a solid phase with stiffness $\mathbb{C}^s_{eq} = 3k^s_{eq}\mathbb{J} + 2\mu^s_{eq}\mathbb{K}$ where (2.38) and (2.42) are used, eventually yields the homogenizd stiffness coefficients :

$$f < \frac{1}{3} \quad \begin{cases} k^{eff} = K_n\, d\left[(\frac{2}{3}(1-3f) + \frac{8f(3f-2)^2}{(3f-4)(3f-1)}\,\rho\right] & (a) \\ \mu^{eff} = K_n\, d\left[\frac{1}{4}(1-3f) + \frac{3(1-f)(3f-2)^2}{2(3f-4)(3f-1)}\,\rho\right] & (b) \end{cases} \tag{2.43}$$

and,

$$f > \frac{1}{3} \qquad \begin{cases} k^{eff} = K_n\, d\, \frac{4(1-f)(1-2f)}{3f(3f-1)}\, \rho & (a) \\ \mu^{eff} = K_n\, d\, \frac{1-2f}{(3f-1)}\, \rho & (b) \end{cases} \tag{2.44}$$

(2.43) and (2.44) retrieve the homogenized stiffness coefficients derived previously by [Dormieux et al.,07].

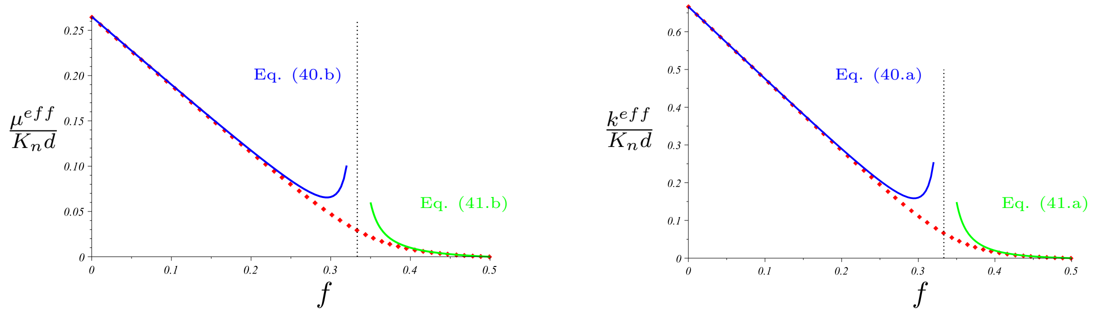

Figure 2.3: self-consistent scheme estimates vs. pore volume fraction ($\rho = 10^{-2}$): (a) homogenized shear modulus; (b) homogenized bulk modulus

2.5 Appendix

2.5.1 Classical self-consistent scheme

Consider an heteregenous material made up of n linear elastic phases, with stiffness tensor $\mathbb{C}_r$ $(r = 1, \dots, n)$. The self-consistent scheme provides an estimate of the effective stiffness $\mathbb{C}^{eff}$ as the solution of the following implicit equation:

$$\mathbb{C}^{eff} = \overline{\mathbb{C}_r : (\mathbb{I} + \mathbb{P}_r : \delta\mathbb{C}_r)^{-1}} : \overline{(\mathbb{I} + \mathbb{P}_r : \delta\mathbb{C}_r)^{-1}}^{-1} \tag{2.45}$$

with $\delta\mathbb{C}_r = \mathbb{C}_r - \mathbb{C}^{eff}$. $\mathbb{P}_r$ denotes the Hill tensor of the material with stiffness $\mathbb{C}^{eff}$, associated with the ellipsoidal shape selected for the inclusion representing phase r. When the same shape is adopted for all phases, all the $\mathbb{P}_r$ $(r = 1, \dots, n)$ are equal and (2.45) proves to be equivalent to :

$$\overline{(\mathbb{I} + \mathbb{P} : \delta\mathbb{C}_r)^{-1}} = \mathbb{I} \tag{2.46}$$

and yields:

$$\mathbb{C}^{eff} = \overline{\mathbb{C}_r : (\mathbb{I} + \mathbb{P} : \delta\mathbb{C}_r)^{-1}} \tag{2.47}$$

It is recalled that

$$\mathbb{P} = \frac{1}{3k^{eff} + 4\mu^{eff}}\mathbb{J} + \frac{3(k^{eff} + 2\mu^{eff})}{5\mu^{eff}(3k^{eff} + 4\mu^{eff})}\mathbb{K} \tag{2.48}$$

2.5.2 Cardan's solution of a cubic polynomial equation

Eq. (2.35) is a cubic equation of the form :

$$M^3 + a_2(f,\rho)\,M^2 + a_1(f,\rho)\,M + a_0(f,\rho) = 0 \tag{2.49}$$

Introducing the following notations :

$$p = \frac{a_2^2}{3} - a_1 \geq 0 \quad \forall \rho \geq 0, \forall f \quad ; \quad q = \frac{a_2}{3}\left(a_1 - \frac{2\,a_2^2}{9}\right) - a_0$$

the discriminant of (2.49), defined as $\Delta = q^2 - 4p^3/27$, always meets the condition:

$$\Delta \leq 0 \quad \forall \rho \geq 0, \forall f \in [0,1/2]$$

so that the sole real and positive root of (2.49) reads (Cardan's method, 1545):

$$M(f,\rho) = 2\sqrt{\frac{p}{3}}\cos\left(\frac{1}{3}\arccos\left(\frac{q}{2}\sqrt{\frac{27}{p^3}}\right)\right) - \frac{a_2}{3} \tag{2.50}$$

Bibliography

[Benveniste and Miloh,01] Benveniste Y. and Miloh T. Imperfect soft and stiff interfaces in two-dimensional elasticity. *Mech. Mater.*, 33:309–324, 2001.

[Biot,41] Biot M.A. General theory of three-dimensional consolidation, *Journal of Applied Physics*, 12, 155–164.,1941.

[Coussy,95] Coussy 0. *Mechanics of porous continua*. Wiley, 1995.

[Dormieux et al.,02] Dormieux L., Molinari A., and Kondo D. Micromechanical approach to the behavior of poroelastic materials. *J. Mech. Phys. Solids*, 50:2203–2231, 2002.

[Dormieux et al.,06] Dormieux L., Kondo D., and Ulm F.-J. *Microporomechanics*. Wiley, 2006.

[Dormieux et al.,07] Dormieux L., Sanahuja J., and Maalej Y. Résistance d'un polycristal avec interfaces imparfaites. *Comptes rendus Mecanique*, 335:25–31, 2007.

[Dormieux et al.,10] Dormieux L., Jeannin L., Bemer E., Le T. H., and Sanahuja J. Micromechanical models of the strength of a sandstone. *Int. J. Numer. Anal. Meth. Geomech.*, 34:249–271, 2010.

[Hashin,02] Hashin Z. Thin interphase/imperfect interface in elasticity with application to coated fiber composites. *J. Mech. Phys. Solids*, 50:2509–2537, 2002.

[Herve and Zaoui,93] Hervé E. and Zaoui A. N-layered inclusion based micromechanical modelling. *Int. J. Eng. Sc.*, 31:1–10, 1993.

[Kroener,78] Kroener E. Self-consistent scheme and graded disorder in polycrystal elasticity. *Journal of Physics F: Metal Physics*, 8:2261–2267, 1978.

[Maalej et al.,07] Maalej Y., Dormieux L., and Sanahuja J. Elastic non linear behavior of a granular medium: micromechanical approach. *Comptes rendus Mecanique*, 335:461–466, 2007.

[Maalej et al.,09] Maalej Y., Dormieux L., and Sanahuja J. Micromechanical approach to the failure criterion of granular media. *Eur. J. Mech./A Solids*, 28:647–653, 2009.

[Pichler and Dormieux,08] Pichler B. and Dormieux L. Consistency of homogenization schemes in linear poroelasticity. *Comptes rendus Mecanique*, 336:636–642, 2008.

[Tompson and Willis,91] Thompson M. and Willis J.R. A reformation of the equations of anisotropic poroelasticity. *J. Appl. Mech.*, 58:612–616, 1991.

[Zaoui,02] Zaoui A. Continuum micromechanics:survey. *J. Eng. Mech.*, 128:808–816, 2002.

Chapter 3

Mohr-Coulomb interface effects on strength criteria of granular materials

Contents

Rappels du contenu

Comme mentionné au chapitre 1, l'étude des matériaux granulaires a une importance considérable dans les problèmes de géotechniques et en génie civil. Le comportement mécanique macroscopique de ces matériaux étant directement lié aux propriétés d'interfaces locales de contact entre particules, la modélisation micromécanique de leur comportement à partir de l'échelle du niveau des grains est une question importante et de grand intérêt. Nous nous interessons en particulier au critère de résistance de ce type de mateŕiau granulaire. Bien qu'examiné récemment dans [Maalej et al.,09] et [Dormieux et al.,10], le sujet n'a été abordé que dans le cadre d'une hypothèse d'interface de type Mohr-Coulomb non-cohésve ($T_t + \alpha T_n \leq 0$). Or cette hypothèse n'est pas toujours conformée à la réalité de nombreux matériaux de la géotechnique. L'objectif principal de ce chapitre est d'étudier les effets d'interface de type Mohr-Coulomb cohésive ($T_t + \alpha T_n \leq \alpha h$) sur le critère de résistance des milieux granulaires.

L'idée est de suivre l'approche développée dans [Barthelemy and Dormieux,04] [Barthelemy and Dormieux,03]. La théorie de l'analyse limite requiert la considération du vecteur de contrainte microscopique au niveau des interfaces. Un vecteur est décrit par $\mathbf{T} = \partial \pi^I / \partial \mathbf{v}$, où π^I désigne la fonction d'appui du domaine convexe G^I des états de vecteur contrainte admissibles au niveau des interfaces. Afin de surmonter la difficulté induite par la singularité de π^I, ce vecteur est redéfini en introduisant une séquence de potentiels $\psi_a(\mathbf{v})$ (cf.[Barthelemy and Dormieux,03]). On démontre que la solution de la séquence de problèmes visco-plastiques trouvée à l'aide de techniques d'homogénéisation nonlinéaire conduit asymptotiquement à l'ensemble des états de contrainte limite macroscopiques. Dans le cas d'un comportement d'interface de Mohr-Coulomb cohésive, la résolution du problème implique techniquement un vecteur précontraint $\mathbf{T}^p$ au niveau des interfaces ce qui modifie l'analyse habituelle des matériaux granulaires poreux avec des effets d'interface dans le cas sec.

Se référant au modèle poro-élastique pour les milieux granulaires saturés avec des interfaces imparfaites exposé au Chapitre 2 (voir aussi [He et al.,2]) et le schéma auto-cohérent généralisé [Dormieux et al.,07], le critère de résistance des milieux granulaires avec effets d'interface de type Mohr-Coulomb cohésif peut être determiné et dépend du coefficient de frottement microscopique des grains α. On montre que dans le cas d'une porosité $\phi_0 < 1/3$, la résistance macroscopique est définie par $\Sigma_m \leq \lambda h$ et $\Sigma_d \to \infty$. Dans le cas de $1/3 < \phi_0 < 1/2$, une transition des enveloppes elliptiques aux enveloppes hyperboliques dans le plan Σ_m-Σ_d

est noté. Cette transition dépend d'un coefficient de frottantement critique $\alpha^{crit.}$.

Ce chapitre a fait l'objet d'une publication soumise à une revue internationale, et dont le titre est 'Mohr-Coulomb interface effects on strength criteria of materials with granular-based structure'

3.1 Introduction

Mechanical behavior of materials with granular-based microstructure is closely related to local properties and interparticle contact interfaces. To derive new closed-form results for the strength of these materials by micromechanical analysis constitutes an important and open issue when considering interface effects. Recent micromechanical approaches [Maalej et al.,09] and [Dormieux et al.,10] have thus been developped and proved to be efficient to predict homogenized strength properties of granular media by means of non linear homogenization techniques [Suquet,97],[Dormieux et al.,02], which consider a polycrystalline microstructure morphology of granular assemblies made up of rigid grains surrounded by an imperfect interface. The effective behavior is then derived by means of a generalized self-consistent scheme [Dormieux et al.,07] taking advantage of the generalized Eshelby solution [Hashin,91].

Meanwhile, an original method[1]has been proposed in [Barthelemy and Dormieux,04] which is also efficiently employed in order to estimate homogenized strength properties, even for the situation of non-associated plasticity [Maghous et al.,09]. Macroscopic criteria of two kinds of materials have been derived along this line: -1) porous media having a Drucker-Prager type solid phase; -2) heterogeneous materials made up of a Drucker-Prager type matrix reinforced by rigid inclusions (mortar, concrete, shale...). However, the prediction of the strength of materials with granular-based microstructure, which rises a prestressed poroelastic problem waiting to be solved, still constitutes a widely open question in the case of the interface described by a cohesive Mohr-Coulomb type criterion.

Taking advantage of a new poroelastic model for fluid-saturated granular media with imperfect interfaces recently derived in [He et al.,2] (from which the prestressed poroelastic problem can be solved), the aim of this paper is to investigate cohesive Mohr-Coulomb interface effects on the strength criterion of materials with granular-based microstructure. The methodology proposed follows that introduced in [Barthelemy and Dormieux,04] for Drucker-Prager matrice extended here to the more difficult case of materials with Mohr-Coulomb interfaces. The strength criterion of materials with granular-based microstructure including Mohr-Coulomb interface effects is determined as a function of the material pore volume fraction and the local strength properties of the Mohr-Coulomb interfaces.

---

[1] *This method is based on the mathematical equivalence between the Limit Analysis problem and a fictitious non-linear viscous problem which can be solved by using the non-linear homogenization techniques [Suquet,97],[Dormieux et al.,02]*

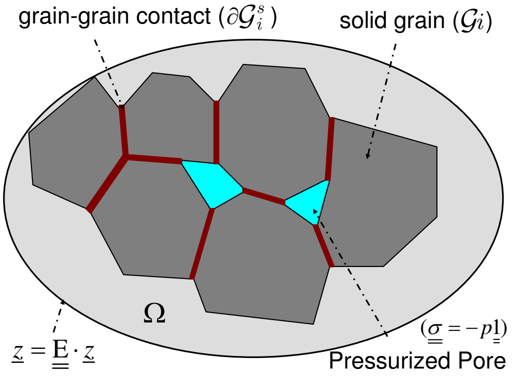

Figure 3.1: *r.e.v* Ω *of a fluid-saturated granular medium*

Notations: The unit tensor of fourth and second order are denoted by $\mathbb{I}$ and $\mathbf{1}$ respectively. We also introduce the fourth order tensor $\mathbb{J} = \frac{1}{3}\mathbf{1}\otimes\mathbf{1}$ and $\mathbb{K} = \mathbb{I} - \mathbb{J}$.

3.2 Poroelastic behavior of materials with interface effects

3.2.1 general results

Prior to dealing with homogenization of the strength, it will prove useful to summarize some results concerning the poroelastic behavior with interface effects. Let us consider a representative element volume ($r.e.v$) Ω made up of an assembly of grains $\mathcal{G}_i$ and of the pore space $\mathcal{P}$ in between. The latter is filled by a fluid at pressure p. The part of the boundary $\partial\mathcal{G}_i$ in contact with other solid grains is denoted by $\partial\mathcal{G}_i^s$ while I_{ij} denotes the interface between grains $\mathcal{G}_i$ and $\mathcal{G}_j$. We also introduce $\Gamma = \cup_{ij} I_{ij}$ and we note for further use that

$$|\Gamma| = \frac{1}{2}\sum_i |\partial\mathcal{G}_i^s| \tag{3.1}$$

where $|\Gamma|$ denotes the area of the surface Γ. The volume fractions of the solid grains and of the pore space are related by

$$f_i = \frac{|\mathcal{G}_i|}{|\Omega|} \quad ; \quad f_{\mathcal{P}} = \frac{|\mathcal{P}|}{|\Omega|} \quad ; \quad \sum_i f_i = 1 - f_{\mathcal{P}} \tag{3.2}$$

$f_{\mathcal{P}}$ is the so-called porosity. In this section, a linear elastic behavior of the interface I_{ij} is assumed:

$$\begin{gathered}\boldsymbol{\sigma}\cdot\mathbf{n}_{i\rightarrow j} = \mathbf{K}\cdot\left(\boldsymbol{\xi}_j - \boldsymbol{\xi}_i\right)\\ [\![\boldsymbol{\sigma}]\!]\cdot\mathbf{n} = 0\\ \mathbf{K} = K_n\mathbf{n}\otimes\mathbf{n} + K_t(\mathbf{1} - \mathbf{n}\otimes\mathbf{n})\end{gathered} \tag{3.3}$$

where $\mathbf{n}$ is the unit normal to the interface I_{ij}. The stress vector is continuous whereas there is a displacement jump $[\![\boldsymbol{\xi}]\!] = \boldsymbol{\xi}_j - \boldsymbol{\xi}_i$ across the interface I_{ij}. The normal component of the displacement jump is the scalar $\xi_n = [\![\boldsymbol{\xi}]\!] \cdot \mathbf{n}$. The tangential component is the vector $\boldsymbol{\xi}_t = (\mathbf{1} - \mathbf{n} \otimes \mathbf{n}) \cdot [\![\boldsymbol{\xi}]\!]$.

The stiffness of the interface is characterized by the tensor $\mathbf{K}$ which involves a normal and a tangential stiffness coefficient. Let $\mathbb{C}^s$ denote the stiffness tensor of the solid material the grain is made up of. In the framework of uniform strain boundary conditions, the local problem of elasticity at the microscopic scale is defined by the following equations:

$$\begin{array}{ll} \operatorname{div} \boldsymbol{\sigma} = 0 & (\Omega) \\ \mathbf{T} = \boldsymbol{\sigma} \cdot \mathbf{n} = \mathbf{K} \cdot [\![\xi]\!] & (I_{ij} \subset \Gamma) \\ \boldsymbol{\sigma} = \mathbb{C}^s : \boldsymbol{\varepsilon} & (\mathcal{G}_i \subset \Omega) \\ \boldsymbol{\sigma} = -p\mathbf{1} & (\mathcal{P}) \\ \boldsymbol{\xi} = \mathbf{E} \cdot \mathbf{z} & (\partial\Omega) \end{array} \tag{3.4}$$

where $\mathbf{E}$ is the macroscopic strain tensor. In particular, the normal component $\sigma_{nn} = \mathbf{n} \cdot \boldsymbol{\sigma} \cdot \mathbf{n}$ on the grain boundary $\partial\mathcal{G}_i$ is given by:

$$\sigma_{nn} = \begin{cases} -p & (\partial\mathcal{G}_i \cap \mathcal{P}) \\ K_n \xi_n & (I_{ij},\, j \neq i) \end{cases} \tag{3.5}$$

The purpose of homogenization is to derive the macroscopic state equations. The macroscopic stress $\boldsymbol{\Sigma}$ is defined as the average $\overline{\boldsymbol{\sigma}}$ of the stress field $\boldsymbol{\sigma}$:

$$\boldsymbol{\Sigma} = \overline{\boldsymbol{\sigma}} = \frac{1}{|\Omega|} \int_\Omega \boldsymbol{\sigma} \, dV = \sum_i f_i \overline{\boldsymbol{\sigma}}^{\mathcal{G}_i} - p f_{\mathcal{P}} \mathbf{1} \tag{3.6}$$

with

$$\overline{\boldsymbol{\sigma}}^{\mathcal{G}_i} = \frac{1}{|\mathcal{G}_i|} \int_{\mathcal{G}_i} \boldsymbol{\sigma} \, dV = \frac{1}{|\mathcal{G}_i|} \int_{\partial\mathcal{G}_i} \mathbf{z} \otimes \boldsymbol{\sigma} \cdot \mathbf{n} \, dS \tag{3.7}$$

In (3.7), $\mathbf{z}$ denotes the location on the boundary of the grain. In the case of elasticity, the macroscopic stress is sought as a function of $\mathbf{E}$. In the poroelastic case, the pore pressure appears as an additional state variable (see [Dormieux et al.,06b],[He et al.,2]):

$$\boldsymbol{\Sigma} = \mathbb{C}^{hom} : \mathbf{E} - p\mathbf{B} \tag{3.8}$$

$\mathbb{C}^{hom}$ is the homogenized stiffness and $\mathbf{B}$ is referred to as the Biot tensor in poroelasticity [Coussy,03]. Since a new state variable is introduced, poroelasticity requires a second state equation. It involves the normalized pore volume change $\phi - \phi_o$ which is related to the state variables $\mathbf{E}$ and p:

$$\phi - \phi_o = \frac{p}{N} + \mathbf{B} : \mathbf{E} \quad \text{with} \quad \phi = |\mathcal{P}|/|\Omega_o| \tag{3.9}$$

N is referred to as Biot modulus. The subscript o corresponds to the value in the initial configuration. In the framework of infinitesimal transformation, $\phi_o = |\mathcal{P}_o|/|\Omega_o|$ also represents the pore volume fraction, that is, the porosity $f_{\mathcal{P}}$.

In the isotropic case, $\mathbb{C}^{hom}$ is characterized by the effective bulk and shear module:

$$\mathbb{C}^{\text{hom}} = 3k^{\text{hom}}\mathbb{J} + 2\mu^{\text{hom}}\mathbb{K} \tag{3.10}$$

and the Biot tensor is defined by the scale Biot coefficient b: $\mathbf{B} = b\mathbf{1}$. Let r_0 denote the characteristic grain size. It is convenient to normalize k^{hom} and μ^{hom} by $K_n r_0$

$$k^{\text{hom}} = K_n r_0 K(\phi_o, \rho) \quad ; \quad \mu^{\text{hom}} = K_n r_0 M(\phi_o, \rho) \tag{3.11}$$

where $\rho = K_t/K_n$. In the limit case of rigid grains ($\mathbb{C}^s \to \infty$), the self-consistent scheme provides the following series expansions of K and M in the neighborhood of $\rho = 0$ [Maalej et al.,09]. The mathematical expressions depend on the value of the porosity.

When $\phi_o < 1/3$:

$$\begin{aligned} &K(\phi_o, \rho) = \mathcal{K}_0(\phi_o) + \mathcal{K}_1(\phi_o)\rho \\ &\mathcal{K}_0(\phi_o) = \frac{2}{3}(1 - 3\phi_o)\,; \qquad \mathcal{K}_1(\phi_o) = \frac{8\phi_o (3\phi_o - 2)^2}{(3\phi_o - 4)(3\phi_o - 1)} \end{aligned} \tag{3.12}$$

and

$$\begin{aligned} &M(\phi_o, \rho) = \mathcal{M}_0(\phi_o) + \mathcal{M}_1(\phi_o)\rho \\ &\mathcal{M}_0(\phi_o) = \frac{1}{4}(1 - 3\phi_o)\,; \qquad \mathcal{M}_1(\phi_o) = \frac{3(1 - \phi_o)(3\phi_o - 2)^2}{2(3\phi_o - 4)(3\phi_o - 1)} \end{aligned} \tag{3.13}$$

When $1/3 < \phi_o < 1/2$:

$$\begin{aligned} &K(\phi_o, \rho) = \mathcal{K}(\phi_o)\rho \quad \text{with} \quad \mathcal{K}(\phi_o) = \frac{4(1 - \phi_o)(1 - 2\phi_o)}{3\phi_o(3\phi_o - 1)} \\ &M(\phi_o, \rho) = \mathcal{M}(\phi_o)\rho \quad \text{with} \quad \mathcal{M}(\phi_o) = \frac{1 - 2\phi_o}{3\phi_o - 1} \end{aligned} \tag{3.14}$$

Furthermore, the poroelastic coefficients can be estimated from a homogenization scheme [He et al.,2]:

$$b = 1 - \frac{3k^{\text{hom}}}{2K_n r_0} = 1 - \frac{3}{2}K \quad ; \quad \frac{1}{N} = \frac{3(b - \phi_o)}{2K_n r_0} \tag{3.15}$$

For forthcoming use in non linear homogenization, we now derive an average for each component of the displacement jump $[\![\boldsymbol{\xi}]\!]$.

3.2.2 The quadratic average of tangential displacement

The macroscopic potential energy density $\Psi(\mathbf{E}, p)$ is classically defined as the difference between the total elastic energy and the work of the given forces, namely the pore pressure in the present case. Note that the elastic energy comprises the contribution of the solid grains and of the interfaces.

$$\Psi(\mathbf{E}, p) = \frac{1}{|\Omega|} \left(\int_\Omega \frac{1}{2} \boldsymbol{\varepsilon} : \mathbb{C}(\mathbf{z}) : \boldsymbol{\varepsilon} \, dV + \int_\Gamma \frac{1}{2} [\![\xi]\!] \cdot \mathbf{K} \cdot [\![\xi]\!] \, dS - p(\phi - \phi_o) \right) \tag{3.16}$$

It can be shown [Dormieux et al.,06b] that the expression of the potential energy as a function of the macroscopic state variables $\mathbf{E}$ and p is:

$$\Psi = \frac{1}{2} \mathbf{E} : \mathbb{C}^{\text{hom}} : \mathbf{E} - p\mathbf{B} : \mathbf{E} - \frac{p^2}{2N} \tag{3.17}$$

Let us now introduce the quadratic average $< \xi_t >$ of the tangential displacement jump at the grain-to-grain interface, defined as

$$< \xi_t >^2 = \frac{1}{|\Gamma|} \int_\Gamma \boldsymbol{\xi}_t \cdot \boldsymbol{\xi}_t dS \tag{3.18}$$

Extending the result established in [Maalej et al.,09] to the case of a pressurized pore space, it is readily seen that $< \xi_t >$ can be determined from the derivative of $\Psi(\mathbf{E}, p)$ with respect to K_t:

$$\frac{|\Gamma|}{|\Omega|} < \xi_t >^2 = 2 \frac{\partial \Psi}{\partial K_t} \tag{3.19}$$

This equation constitutes the interface form of a general result early derived by [Kreher,90]. Then (3.17) yields

$$\frac{\partial \Psi}{\partial K_t} = \frac{1}{2} \frac{\partial k^{\text{hom}}}{\partial K_t} {E_v}^2 + \frac{\partial \mu^{\text{hom}}}{\partial K_t} E_d^2 - \frac{\partial b}{\partial K_t} p E_v - \frac{p^2}{2} \frac{\partial (1/N)}{\partial K_t} \tag{3.20}$$

where $E_v = \operatorname{tr} \mathbf{E}$ and $E_d^2 = \mathbf{E}_d : \mathbf{E}_d$ with $\mathbf{E}_d = \mathbb{K} : \mathbf{E}$ are invariants of the macroscopic strain $\mathbf{E}$ and of its deviatoric part $\mathbf{E}_d$.

Finally, recalling (3.15), the average of tangential displacement is written as

$$< \xi_t >^2 = \frac{|\Omega|}{|\Gamma|} \left[2 \frac{\partial \mu^{\text{hom}}}{\partial K_t} E_d^2 + \frac{\partial k^{\text{hom}}}{\partial K_t} \left(E_v + \frac{3p}{2 r_0 K_n} \right)^2 \right] \tag{3.21}$$

Recalling (3.11), (3.21) also reads:

$$\frac{< \xi_t >^2}{r_0^2} = \frac{2}{3\lambda} \left[2 \frac{\partial M}{\partial \rho} E_d^2 + \frac{\partial K}{\partial \rho} \left(E_v + \frac{3p}{2 r_0 K_n} \right)^2 \right] \tag{3.22}$$

where the dimensionless parameter λ is defined as:

$$\lambda = \frac{2 r_0 \, |\Gamma|}{3 \, |\Omega|} \tag{3.23}$$

3.2.3 The average of normal displacement

As regards the normal component ξ_n of the displacement jump, we seek an estimate of the direct average on Γ:

$$< \xi_n >= \frac{1}{|\Gamma|} \sum_{\{i,j\}} \int_{I_{ij}} \xi_n \, dS \tag{3.24}$$

It is prefered to a quadratic average which would not preserve the sign of ξ_n. It is assumed that the average of ξ_n on $\partial \mathcal{G}_i^s$ for a given grain n°i is independent on the considered grain. Accordingly, we have:

$$< \xi_n >= \frac{1}{|\partial \mathcal{G}_i^s|} \sum_{j \neq i} \int_{I_{ij}} \xi_n \, dS \tag{3.25}$$

In turn, introducing (3.5) into (3.25) relates $< \xi_n >$ to the average of the normal stress acting on $\partial \mathcal{G}_i^s$:

$$K_n < \xi_n >= \frac{1}{|\partial \mathcal{G}_i^s|} \int_{\partial \mathcal{G}_i^s} \sigma_{nn} \, dS \tag{3.26}$$

Furthermore, it is assumed that the average of the stress field on a grain $\mathcal{G}_i$ is also independent of the choice of the grain. The stress average rule in the form (3.6) now reads.

$$\boldsymbol{\Sigma} = (1 - \phi_o) \overline{\boldsymbol{\sigma}}^{\mathcal{G}} - p \phi_o \mathbf{1} \tag{3.27}$$

where the subscript i is now omitted. The spherical part of (3.27) reads:

$$\Sigma_m = (1 - \phi_o) \overline{\sigma_m}^{\mathcal{G}} - p \phi_o \tag{3.28}$$

with $\sigma_m = \operatorname{tr} \boldsymbol{\sigma}/3$ and $\Sigma_m = \operatorname{tr} \boldsymbol{\Sigma}/3$. Finally, the assumption that all grains have identical geometrical characteristics also implies that

$$|\Gamma| = \frac{1}{2} \mathcal{N} |\partial \mathcal{G}^s| \quad ; \quad |\Omega| = |\mathcal{G}| \frac{\mathcal{N}}{1 - \phi_o} \tag{3.29}$$

where $\mathcal{N}$ denotes the number of grains in Ω.

The geometry of the grain is now idealized by a spherical shape (radius r_0). Accordingly, $\mathbf{z}$ is replaced by $r_0 \mathbf{n}$ in (3.7). Using (3.5) and (3.26), it is readily seen from (3.7) that

$$\overline{\sigma_m}^{\mathcal{G}} = \frac{r_0}{3|\mathcal{G}|} \int_{\partial \mathcal{G}} \sigma_{nn} \, dS = \frac{r_0 |\partial \mathcal{G}^s|}{3|\mathcal{G}|} \left(K_n < \xi_n > - (\frac{|\partial \mathcal{G}|}{|\partial \mathcal{G}^s|} - 1) p \right) \tag{3.30}$$

Making further use of the spherical grain model, the following estimates are derived:

$$\frac{|\partial \mathcal{G}^s|}{|\partial \mathcal{G}|} = \frac{r_0}{3} \frac{|\partial \mathcal{G}^s|}{|\mathcal{G}|} \quad ; \quad \frac{|\partial \mathcal{G}^s|}{|\mathcal{G}|} = \frac{2}{1 - \phi_o} \frac{|\Gamma|}{|\Omega|} \tag{3.31}$$

The ratio $|\Gamma|/|\Omega|$ represents the specific grain-to-grain surface. (3.28) can now be rearranged in the form:

$$\Sigma_m + p = \lambda(K_n < \xi_n > +p) \tag{3.32}$$

with λ introduced in (3.23). Eventually, recalling (3.10), (3.15) and combining (3.8) with (3.32) yields the sought estimate of $< \xi_n >$:

$$\frac{< \xi_n >}{r_0} = \frac{K}{\lambda} \left(E_v + \frac{3p}{2r_0 K_n} \right) - \frac{p}{K_n r_0} \tag{3.33}$$

3.3 Determination of the homogenized strength

3.3.1 general results

We now consider the determination of the effective strength of a granular medium. This means that we seek the domain G^{hom} of admissible macroscopic stress states $\boldsymbol{\Sigma}$.
At the local scale, this requires the strength properties of the grains and of the interfaces to be characterized. The domain $G^{\mathcal{G}}$ of admissible stress states in the grains is defined by a criterion $f^G(\boldsymbol{\sigma}) \leq 0$:

$$\boldsymbol{\sigma} \in G^{\mathcal{G}} \quad \Leftrightarrow \quad f^G(\boldsymbol{\sigma}) \leq 0 \tag{3.34}$$

The domain G^I of admissible stress vectors acting on the interfaces is defined by a criterion $f^I(\mathbf{T}) \leq 0$:

$$\mathbf{T} \in G^I \quad \Leftrightarrow \quad f^I(\mathbf{T}) \leq 0 \tag{3.35}$$

In turn, the domains $G^{\mathcal{G}}$ and G^I can be described in an equivalent manner by their support functions (see e.g. [Salencon,90], [Dormieux et al.,06b]). As for the grains, the support function of $G^{\mathcal{G}}$ reads:

$$\pi^G(\mathbf{d}) = \sup\{\boldsymbol{\sigma} : \mathbf{d},\ f^G(\boldsymbol{\sigma}) \leq 0\} \tag{3.36}$$

where $\mathbf{d}$ and $\pi^G(\mathbf{d})$ physically represent a virtual strain rate and the associated dissipation. Similarly, for any vector $[\![\mathbf{v}]\!]$, the support function associated to G^I is:

$$\pi^I([\![\mathbf{v}]\!]) = \sup\{\mathbf{T} \cdot [\![\mathbf{v}]\!],\ f^I(\mathbf{T}) \leq 0\} \tag{3.37}$$

where $[\![\mathbf{v}]\!]$ and $\pi([\![\mathbf{v}]\!])$ physically represent a virtual velocity jump across the interface and the associated dissipation. Following [Leblond et al.,94], any admissible macroscopic stress state $\mathbf{\Sigma}$ located on the boundary of G^{hom} can be determined from the solution to a boundary value problem formally equivalent to (3.4) defined on the $r.e.v$ Ω by:

$$\begin{array}{ll} \text{div}\,\boldsymbol{\sigma} = 0 & (\Omega) \\ \mathbf{T} = \dfrac{\partial \pi^I}{\partial [\![\mathbf{v}]\!]} & (I_{ij} \subset \Gamma) \\ \boldsymbol{\sigma} = \dfrac{\partial \pi^G}{\partial \mathbf{d}} & (\mathcal{G}_i \subset \Omega) \\ \boldsymbol{\sigma} = 0 & (\mathcal{P}) \\ \mathbf{v} = \mathbf{D} \cdot \mathbf{z} & (\partial\Omega) \end{array} \tag{3.38}$$

where $\boldsymbol{\sigma}$ and $\mathbf{v}$ respectively denote the microscopic stress field and the microscopic velocity field. $\mathbf{\Sigma}$ is related to $\boldsymbol{\sigma}$ by the stress average rule:

$$\mathbf{\Sigma} = \overline{\boldsymbol{\sigma}} \in \partial G^{hom} \tag{3.39}$$

In other words, the determination of the boundary of G^{hom} amounts to solving a non linear homogenization problem in which fictitious state equations of the grains and of the interfaces are defined from the derivatives of their support functions.

3.3.2 Mohr-Coulomb interface and rigid grains

In this study, the strength of the grains is assumed to be infinite. Therefore, the support function of (3.36) is infinite if $\mathbf{d} \neq 0$ while $\pi^G(0) = 0$. In order to avoid the mathematical singularity, the criterion of the grains is written in the form:

$$f^G(\boldsymbol{\sigma}) = \boldsymbol{\sigma} : \boldsymbol{\sigma} - R^2 \leq 0 \tag{3.40}$$

with $R \to \infty$. It is readily seen that $\pi^G(\mathbf{d}) = R\sqrt{\mathbf{d} : \mathbf{d}}$. This yields:

$$\boldsymbol{\sigma} = \frac{\partial \pi^G}{\partial \mathbf{d}} = \mathbb{C}^G(\mathbf{d}) : \mathbf{d} \quad \text{with} \quad \mathbb{C}^G(\mathbf{d}) = \frac{R}{\sqrt{\mathbf{d} : \mathbf{d}}}(\mathbb{J} + \mathbb{K}) \tag{3.41}$$

In other words, the state equation of the grains to be introduced in problem (3.38) is formally defined by the isotropic secant stiffness tensor $\mathbb{C}^G(\mathbf{d})$. The latter is characterized by the following bulk and shear moduli:

$$k^G(\mathbf{d}) = \frac{R}{3\sqrt{\mathbf{d} : \mathbf{d}}} \quad ; \quad \mu^G(\mathbf{d}) = \frac{R}{2\sqrt{\mathbf{d} : \mathbf{d}}} \tag{3.42}$$

As $R \to \infty$, the apparent stiffness of the grains tends towards infinity.

The strength properties of an interface characterized by a Mohr-Coulomb failure criterion are defined by a condition on the stress vector $\mathbf{T}$ acting on this interface:

$$f^I(\mathbf{T}) = |\mathbf{T}_t| + \alpha(T_n - h) \leq 0 \quad \text{with} \quad \begin{cases} T_n = \mathbf{T}\cdot\mathbf{n} \\ \mathbf{T}_t = \mathbf{T} - T_n\mathbf{n} \end{cases} \tag{3.43}$$

where $\alpha \geq 0$ denotes the coefficient of internal friction and αh is the cohesion. For the Mohr-Coulomb interface, $\pi^I(\llbracket \mathbf{v} \rrbracket))$ is given by [Salencon,90],

$$\begin{aligned} \pi^I(\llbracket \mathbf{v} \rrbracket) &= +\infty \quad \text{if} \quad \llbracket v_n \rrbracket < \alpha|\llbracket \mathbf{v}_t \rrbracket| \\ \pi^I(\llbracket \mathbf{v} \rrbracket) &= h\llbracket v_n \rrbracket \quad \text{if} \quad \llbracket v_n \rrbracket \geq \alpha|\llbracket \mathbf{v}_t \rrbracket| \end{aligned} \tag{3.44}$$

It appears that $\pi^I(\llbracket \mathbf{v} \rrbracket)$ is a strongly singular function and is not differentiable. This prevents from a direct implementation of (3.38). In order to overcome this difficulty, it is proposed to extend the technique introduced in [Barthelemy and Dormieux,03],[Barthelemy and Dormieux,04] to the presence of interfaces. For the sake of clarity, $|\llbracket \mathbf{v}_t \rrbracket|$ and $\llbracket v_n \rrbracket$ will now be simply denoted by v_t and v_n respectively. A sequence ψ_a of convex differentiable functions (indexed by the scalar $a > 0$) is introduced as follows:

$$\psi_a(v_n, v_t) = f_a(Y) + hv_n \tag{3.45}$$

$$Y = v_n - \alpha v_t \tag{3.46}$$

where $f_a(Y)$ is a sequence of convex functions of class C^2 to ensure the convexity of ψ_a. The convex function $f_a(Y)$ meets the following requirements (see Fig.3.2):

is decreasing on $]-a, 0]$ $(f_a'(Y) \leq 0)$;

$f_a(Y) = 0$ when $Y \geq 0$;

$\lim_{Y \to -a^+} f_a(Y) = +\infty$

Then it can be seen from (3.45) that the sequence of functions ψ_a tends towards the Mohr-Coulomb support function $\pi^I(\mathbf{v})$ of (3.44) when the scalar a tends towards 0. Replacing π^I by ψ_a in the fictitious state equation of the interfaces introduced in (3.38), one obtains:

$$\mathbf{T} = \frac{\partial \psi_a}{\partial \llbracket \mathbf{v} \rrbracket} = \frac{\partial \psi_a}{\partial v_n}\mathbf{n} + \frac{\partial \psi_a}{\partial v_t}\mathbf{t} \tag{3.47}$$

with (3.46), (3.47) then yields

$$\mathbf{T} = \mathcal{F}(Y)(\mathbf{n} - \alpha\mathbf{t}) + h\mathbf{n} \qquad \text{with} \quad \mathcal{F}(Y) = \frac{\partial f_a(Y)}{\partial Y} \tag{3.48}$$

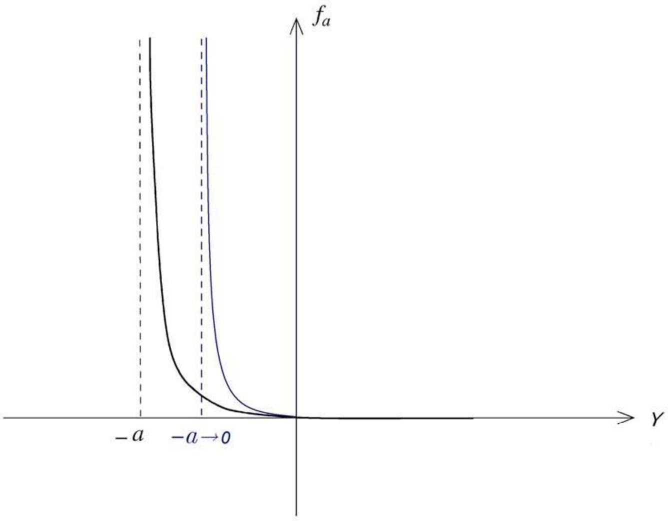

Figure 3.2: Shape of function f_a

If $\mathbf{T} \neq h\mathbf{n}$, (3.48) shows that $\mathcal{F}(Y) \neq 0$, which means $Y \in]-a, 0[$. Therefore, the normality rule $v_n = \alpha v_t$ is asymptotically fulfilled when $a \to 0$.

The stress vector $\mathbf{T}$ in (3.48) can be rearranged and expressed in an affine form with respect to $[\![\mathbf{v}]\!]$:

$$\mathbf{T} = \mathbf{K}(v_n, v_t) \cdot [\![\mathbf{v}]\!] + \mathbf{T}^p(v_n, v_t) \tag{3.49}$$

where $\mathbf{K}$ is a secant stiffness tensor defined according to (3.3) by the following coefficients K_n and K_t :

$$K_n = \frac{\mathcal{F}}{Y} \quad ; \qquad K_t = -\frac{\alpha \mathcal{F}}{v_t} \tag{3.50}$$

It is recalled that $\mathcal{F} \leq 0$. $\mathbf{T}^p$ is a prestress vector term defined as:

$$\mathbf{T}^p(v_n, v_t) = \left(h - \alpha \frac{\mathcal{F}}{Y} v_t \right) \mathbf{n} \tag{3.51}$$

We note for forthcoming use that

$$\frac{T^p}{K_n} = \left(\frac{hY}{\mathcal{F}} - \alpha v_t \right) \tag{3.52}$$

The reason for spliting $\mathbf{T}$ this way lies in the fact that K_n and K_t are positive numbers, which ensures that $\mathbf{K}$ is a definite positive stiffness tensor. This property is related to the already mentioned condition

$$\mathcal{F} \leq 0 \tag{3.53}$$

As already stated, the local flow rule $Y = v_n - \alpha v_t = 0$ is asymptotically satisfied as $a \to 0$. Owing to (3.50), we note that:

$$\lim_{a \to 0} \frac{K_t}{K_n} = \lim_{a \to 0} \frac{-\alpha Y}{v_t} = 0 \tag{3.54}$$

This validates the use of the series expansions of k^{hom} and μ^{hom} (see (3.14)). Similarly, (3.52) asymptotically takes the simplified form:

$$\frac{T^p}{K_n r_0} = -\alpha \frac{v_t}{r_0} \tag{3.55}$$

Eventually, considering a given macroscopic strain rate $\mathbf{D}$, a macroscopic stress state $\boldsymbol{\Sigma}$ located on the boundary ∂G^{hom} is related by the average rule $\boldsymbol{\Sigma} = \overline{\boldsymbol{\sigma}}$ to the microscopic stress field $\boldsymbol{\sigma}(\mathbf{z})$ solution to the following non linear problem:

$$\begin{array}{ll} \text{div } \boldsymbol{\sigma} = 0 & (\Omega) \\ \mathbf{T} = \mathbf{K}(v_n, v_t) \cdot [\![\mathbf{v}]\!] + \mathbf{T}^p(v_n, v_t) & (I_{ij} \subset \Gamma) \\ \boldsymbol{\sigma} = \mathbb{C}^G(\mathbf{d}) : \mathbf{d} & (\mathcal{G}_i \subset \Omega) \\ \boldsymbol{\sigma} = 0 & (\mathcal{P}) \\ \mathbf{v} = \mathbf{D} \cdot \mathbf{z} & (\partial\Omega) \end{array} \tag{3.56}$$

with $\mathbb{C}^G(\mathbf{d}) \to \infty$.

3.3.3 Decomposition of problem (3.58)

The idea of secant methods for the resolution of non linear homogenization problems consists in replacing the secant quantities $\mathbf{K}(v_n, v_t)$, $\mathbf{T}^p(v_n, v_t)$ by constants which are defined from some appropriate average estimates (upperscript av) of v_n and v_t over Γ:

$$\mathbf{K} \approx \mathbf{K}(v_n^{av}, v_t^{av}) \quad ; \quad \mathbf{T}^p \approx T^p(v_n^{av}, v_t^{av})\mathbf{1} \tag{3.57}$$

As regards the grains, the asymptotic case of rigid behavior is considered.
In the framework of this approximation, we come up with a formally linear elastic boundary value problem which is derived from (3.56):

$$\begin{array}{ll} \text{div } \boldsymbol{\sigma} = 0 & (\Omega) \\ \mathbf{T} = \mathbf{K} \cdot [\![\mathbf{v}]\!] + T^p \mathbf{1} & (I_{ij} \subset \Gamma) \\ \boldsymbol{\sigma} = \mathbb{C}^G : \mathbf{d} & (\mathcal{G}_i \subset \Omega) \\ \boldsymbol{\sigma} = 0 & (\mathcal{P}) \\ \mathbf{v} = \mathbf{D} \cdot \mathbf{z} & (\partial\Omega) \end{array} \tag{3.58}$$

We note that the above problem involves two loading parameters which are $\mathbf{D}$ and T^p respectively. We now split (3.58) into two auxiliary problems (denoted by I and II) as suggested by Fig.3.3:

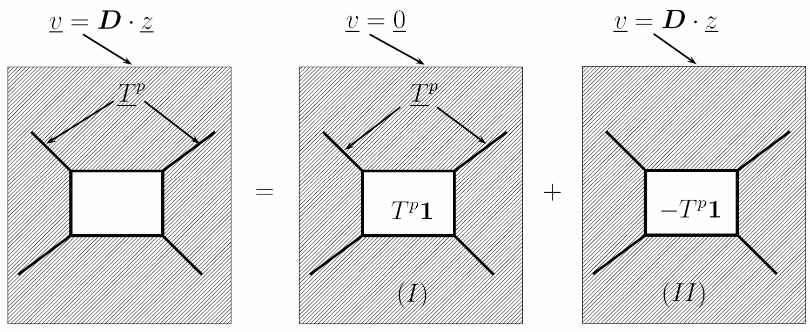

Figure 3.3: Decomposition of the prestressed problem

In problem I, the velocity vanishes on the boundary $\partial\Omega$. There is a prestress $T^p\mathbf{1}$ in Γ and a pressure $-T^p$ in the pore space $\mathcal{P}$:

$$\begin{aligned} &\text{div } \boldsymbol{\sigma} = 0 && (\Omega) \\ &\mathbf{T} = \mathbf{K} \cdot [\![\mathbf{v}]\!] + T^p\mathbf{1} && (I_{ij} \subset \Gamma) \\ &\boldsymbol{\sigma} = \mathbb{C}^G : \mathbf{d} && (\mathcal{G}_i \subset \Omega) \\ &\boldsymbol{\sigma} = T^p\mathbf{1} && (\mathcal{P}) \\ &\mathbf{v} = 0 && (\partial\Omega) \end{aligned} \tag{3.59}$$

It is readily seen that the stress field solution to (3.59) is uniform and equal to $\boldsymbol{\sigma}^I = T^p\mathbf{1}$, while the corresponding velocity field is $\mathbf{v}^I = 0$:

$$\begin{aligned} &\boldsymbol{\Sigma}^I = \overline{\boldsymbol{\sigma}^I} = \boldsymbol{\sigma}^I = T^p\mathbf{1} \\ &\mathbf{v}^I = 0 \end{aligned} \tag{3.60}$$

In problem II, the velocity field is kinematically admissible with $\mathbf{D}$. There is a pressure T^p in the pore space $\mathcal{P}$ (in order to balance the opposite value in problem I). There is no prestress in the interfaces:

$$\begin{aligned} &\text{div } \boldsymbol{\sigma} = 0 && (\Omega) \\ &\mathbf{T} = \mathbf{K} \cdot [\![\mathbf{v}]\!] && (I_{ij} \subset \Gamma) \\ &\boldsymbol{\sigma} = \mathbb{C}^G : \mathbf{d} && (\mathcal{G}_i \subset \Omega) \\ &\boldsymbol{\sigma} = -T^p\mathbf{1} && (\mathcal{P}) \\ &\mathbf{v} = \mathbf{D} \cdot \mathbf{z} && (\partial\Omega) \end{aligned} \tag{3.61}$$

(3.61) is formally identical to (3.4): it suffices to replace $\boldsymbol{\xi}$ and $\mathbf{E}$ by $\mathbf{v}$ and $\mathbf{D}$ respectively, and p by T^p. In other words, problem II is of the poroelastic type. Accordingly, (3.8) reads:

$$\boldsymbol{\Sigma}^{II} = \mathbb{C}^{\text{hom}} : \mathbf{D} - bT^p\mathbf{1} \tag{3.62}$$

which, together with (3.60) yields:

$$\boldsymbol{\Sigma} = \boldsymbol{\Sigma}^{II} + T^p\mathbf{1} = \mathbb{C}^{\text{hom}} : \mathbf{D} + (1-b)T^p\mathbf{1} \tag{3.63}$$

Moreover, the solution $\mathbf{v}^{II}$ of problem II in fact coincides with the solution $\mathbf{v}$ of (3.58), since $\mathbf{v}^I = 0$:

$$\mathbf{v} = \mathbf{v}^{II} \tag{3.64}$$

This makes it possible to use the averages determined at sections 3.2.2 (see (3.21)) and 3.2.3 (see (3.33)). Accordingly, the following definition of the averages v_n^{av} and v_t^{av} is adopted:

$$v_n^{av} =< v_n^{II} > \quad ; \quad v_t^{av} =< v_t^{II} > \tag{3.65}$$

(3.32) now reads:

$$\Sigma_m = \lambda(K_n v_n^{av} + T^p) \tag{3.66}$$

where it has been used that $\Sigma_m = \Sigma_m^{II} + T^p$ (see (3.63)). Similarly, (3.33) yields:

$$\frac{v_n^{av}}{r_0} = \frac{K}{\lambda}\left(D_v + \frac{3T^p}{2r_0K_n}\right) - \frac{T^p}{K_n r_0} \tag{3.67}$$

In turn, (3.22) takes the form:

$$\frac{v_t^{av2}}{r_0^2} = \frac{2}{3\lambda}\left[2\frac{\partial M}{\partial \rho}D_d^2 + \frac{\partial K}{\partial \rho}\left(D_v + \frac{3T^p}{2r_0K_n}\right)^2\right] \tag{3.68}$$

Finally, from the deviatoric part of (3.63), we note for forthcoming use that:

$$\Sigma_d = 2\mu^{\text{hom}} D_d \tag{3.69}$$

with $\Sigma_d^2 = \boldsymbol{\Sigma}_d : \boldsymbol{\Sigma}_d$.

3.3.4 System of equations at limit state

In order to incorporate the local flow rule ($Y = 0$), we have seen that the asymptotic case $a \to 0$ must be considered. In addition, in the line of reasoning of secant methods, the local flow rule is to be written on the average estimates of v_n and v_t:

$$\lim_{a\to 0} Y = 0 \qquad \Rightarrow \qquad v_n^{av} = \alpha v_t^{av} \tag{3.70}$$

Similarly, (3.55) now reads:

$$\frac{T^p}{K_n r_0} = -\alpha \frac{v_t^{av}}{r_0} \tag{3.71}$$

(3.14) into (3.67) together with (3.66) yields

$$\Sigma_m = \lambda \left(K_n v_n^{av} + T^p \right) = K r_0 K_n \left(D_v + \frac{3T^p}{2K_n r_0} \right) \tag{3.72}$$

In turn, (3.50) and (3.51) yield

$$\left(K_n v_n^{av} + T^p \right) = \mathcal{F} + h \tag{3.73}$$

Therefore, (3.72) now reads

$$\Sigma_m = \lambda \left(\mathcal{F} + h \right) \tag{3.74}$$

While (3.50), (3.72) and (3.74)

$$\frac{v_t^{av}}{r_0} = \mathcal{G} \left(D_v + \frac{3T^p}{2K_n r_0} \right) \tag{3.75}$$

with

$$\mathcal{G} = \frac{-\alpha \mathcal{F}}{\lambda \left(\mathcal{F} + h \right)} \frac{K}{\rho} \tag{3.76}$$

Let us now make use of (3.71) which incorporates the local flow rule (in the averaged form $v_n^{av} \approx \alpha v_t^{av}$). Combined with (3.75), one obtains:

$$\frac{v_t^{av}}{r_0} = \frac{2\mathcal{G}}{2 + 3\alpha\mathcal{G}} D_v \tag{3.77}$$

Moreover, (3.68) together with (3.75) takes the following form:

$$\frac{3}{2} \lambda \left(\frac{v_t^{av}}{r_0} \right)^2 = 2 \frac{\partial M}{\partial \rho} {D_d}^2 + \frac{\partial K}{\partial \rho} \left(\frac{v_t^{av}}{\mathcal{G} r_0} \right)^2 \tag{3.78}$$

which may be simplified into:

$$\left(\frac{v_t^{av}}{r_0} \right)^2 = \frac{4M_{,\rho} \mathcal{G}^2}{3\lambda \mathcal{G}^2 - 2K_{,\rho}} D_d^2 \tag{3.79}$$

Finally, a combination of (3.75) and (3.78) gives

$$\frac{4M_{,\rho} \mathcal{G}^2}{3\lambda \mathcal{G}^2 - 2K_{,\rho}} D_d^2 = \frac{4\mathcal{G}^2}{\left(2 + 3\alpha\mathcal{G} \right)^2} {D_v}^2 \tag{3.80}$$

3.3.5 Macroscopic strength criterion

3.3.5.1 The case $1/3 < \phi_o < 1/2$

We first consider the case $1/3 < \phi_o < 1/2$ which is a general case for the granular material. Recalling (3.14), the parameters $K_{,\rho}$ and $M_{,\rho}$ in (3.80) read:

$$\begin{cases} K_{,\rho} = \frac{\partial K}{\partial \rho} = \mathcal{K} \\ M_{,\rho} = \frac{\partial M}{\partial \rho} = \mathcal{M} \end{cases} \tag{3.81}$$

Meanwhile with (3.14), (3.76) can be also simplified as,

$$\mathcal{G}(\mathcal{F}) = -\frac{\alpha \mathcal{K} \mathcal{F}}{\lambda(\mathcal{F} + h)} \tag{3.82}$$

Thus, (3.80),(3.81) and (3.82) proves that $\mathcal{F}$ is the solution of the following equation :

$$\mathrm{a}\mathcal{F}^2 + \mathrm{b}\mathcal{F} + \mathrm{c} = 0 \tag{3.83}$$

with

$$\begin{cases} \mathrm{a} = 2\left(1-\delta\right)\Delta \\ \mathrm{b} = 4h\Delta \\ \mathrm{c} = 2h^2\left(\mathcal{K}{D_v}^2 + 2\mathcal{M}{D_d}^2\right) \end{cases} \tag{3.84}$$

$$\Delta = \mathcal{K}{D_v}^2 + 2\left(1-\delta\right)\mathcal{M}{D_d}^2 \tag{3.85}$$

where we introduced the dimensionless parameter:

$$\delta = \frac{3\alpha^2\mathcal{K}}{2\lambda} \tag{3.86}$$

It can be easily verified that the existence of solutions to (3.83) requires that $\Delta \geq 0$. If this condition is satisfied, (3.83) has a priori the following solutions:

$$\mathcal{F} = \frac{h}{\delta - 1}\left(1 + \epsilon\sqrt{\frac{\delta\mathcal{K}}{\Delta}}|D_v|\right) \quad \text{with} \quad \epsilon = \pm 1 \tag{3.87}$$

However, the appropriate solution must be negative (see (3.53)). Besides, due to the very definition of v_t ($v_t = |\mathbf{v}_t|$), the solution $\mathcal{F}$ must also be compatible with the condition $v_t^{av} \geq 0$. It appears that the macroscopic strength criterion is controlled by the dimensionless parameter δ.

We first assume that $\delta < 1$ which ensures that $\Delta > 0$ and $\mathcal{K}D_v^2/\Delta < 1$. Combining (3.77) and (3.87), and recalling that $\mathcal{F} \leq 0$, the condition $v_t^{av} \geq 0$ amounts to $\epsilon D_v < 0$, that is, $\epsilon = -D_v/|D_v|$. Accordingly, the appropriate solution to (3.83) reads

$$\mathcal{F} = \frac{h}{\delta - 1}\left(1 - \sqrt{\frac{\delta\mathcal{K}}{\Delta}}D_v\right) \tag{3.88}$$

In turn, using the definition (3.85) of Δ and the condition $\delta < 1$, it is readily seen that the requirement $\mathcal{F} \leq 0$ is indeed fulfilled. The mean stress Σ_m and the deviatoric stress Σ_d are now determined from (3.74) and (3.69) respectively:

$$\Sigma_m = \lambda\left(\mathcal{F} + h\right) \tag{3.89}$$

$$\Sigma_d = 2\mu^{\text{hom}}D_d = -2\alpha\mathcal{M}\mathcal{F}\frac{D_d}{v_t^{av}/r_0} \tag{3.90}$$

where μ^{hom} is derived from (3.11) together with (3.50). Introducing (3.88) with (3.77) into (3.89) and (3.90) yields:

$$\begin{aligned} \Sigma_m &= \frac{\delta h\lambda}{\delta - 1}\left(1 - \sqrt{\frac{\mathcal{K}}{\delta\Delta}}D_v\right) \\ \Sigma_d &= 2\lambda h\sqrt{\frac{\delta}{\mathcal{K}\Delta}}\mathcal{M}D_d \end{aligned} \tag{3.91}$$

(3.91) are the parametric equations of the boundary ∂G^{hom} of the domain of admissible macroscopic stress states. Eliminating the ratio D_d/D_v provides the cartesian equation of ∂G^{hom} which proves to be an ellipse in the plane (Σ_m, Σ_d):

$$\left(\frac{\Sigma_m - C}{A}\right)^2 + \left(\frac{\Sigma_d}{B}\right)^2 = 1 \tag{3.92}$$

with

$$A = h\lambda\frac{\sqrt{\delta}}{1-\delta} \quad ; \quad B = h\lambda\sqrt{\frac{2\delta\mathcal{M}}{(1-\delta)\mathcal{K}}} \quad ; \quad C = h\lambda\frac{\delta}{\delta - 1} \tag{3.93}$$

The negative scalar C represents the location of the center of the domain on the axis $\Sigma_d = 0$.

We now assume that $\delta > 1$ which ensures that $\mathcal{K}D_v^2/\Delta > 1$. The two solutions given in (3.87) (that exist provided that $\Delta > 0$) have now opposite signs. Again, we recall that the appropriate one is negative. In turn, the condition $v_t^{av} \geq 0$ together with (3.77) shows that D_v must be positive. It then appears that the negative solution in (3.87) is again given by (3.88), so that (3.91) represents the parametric equations of ∂G^{hom}. Eventually, eliminating the ratio D_d/D_v provides the equation of a hyperbola:

$$\left(\frac{\Sigma_m - C}{A'}\right)^2 - \left(\frac{\Sigma_d}{B'}\right)^2 = 1 \tag{3.94}$$

with

$$A' = h\lambda\frac{\sqrt{\delta}}{\delta - 1} \quad ; \quad B' = h\lambda\sqrt{\frac{2\delta\mathcal{M}}{(\delta - 1)\mathcal{K}}} \tag{3.95}$$

The positive scalar C now represents the isotropic tensile strength.

Moreover, when $\delta > 1$ we may encounter the situation where $\Delta = 0$. Since D_v must be positive, (3.85) yields

$$\frac{D_v}{D_d} = \sqrt{\frac{2(\delta - 1)\mathcal{M}}{\mathcal{K}}} \tag{3.96}$$

Introducing (3.96) in (3.91), an asymptotic criterion appearing as a Drucker-Prager type criterion is eventually obtained:

$$\Sigma_d = \frac{B'}{A'}(C - \Sigma_m) \tag{3.97}$$

with A',B',C defined in (3.95),(3.93).

Let us now consider the case $\delta = 1$. From(3.86), this condition yields a critical value of the interface friction coefficient α^{crit} defined as:

$$\alpha^{crit} = \sqrt{\frac{2\lambda}{3\mathcal{K}}} \tag{3.98}$$

Consequently, the macroscopic strength criterion depends upon the position of the interface friction coefficient α with respect to this critical value. At a given porosity, low frictional property between grains ($\alpha < \alpha^{crit}$) yields an elliptic failure envelope defined by (3.92), while high frictional property ($\alpha > \alpha^{crit}$) yields a hyperbolic failure envelope defined by (3.94).

3.3.5.2 The case $\phi_o < 1/3$

We then consider the case $\phi_o < 1/3$. Following (3.12) and (3.13), the parameters $K_{,\rho}$ and $M_{,\rho}$ in (3.80) now read:

$$\begin{cases} K_{,\rho} = \frac{\partial K}{\partial \rho} = \mathcal{K}_1 \\ M_{,\rho} = \frac{\partial M}{\partial \rho} = \mathcal{M}_1 \end{cases} \tag{3.99}$$

Meanwhile with (3.14), (3.76) can be also simplified as,

$$\mathcal{G}(\mathcal{F}) = -\frac{\alpha\mathcal{F}}{\lambda(\mathcal{F} + h)}(\frac{\mathcal{K}_0}{\rho} + \mathcal{K}_1) \tag{3.100}$$

Since we have simultaneously $\mathcal{F} \to 0$ and $\rho \to 0$ in the expression (3.100), let us assume that

$$\mathcal{F} = \mathcal{A}\rho\chi \quad ; \quad \text{with} \quad \chi = \frac{\mathcal{K}_1}{\mathcal{K}_0} \tag{3.101}$$

where $\mathcal{A} \leq 0$ is the solution of the following equation:

$$\mathrm{a}\mathcal{A}^2 + \mathrm{b}\mathcal{A} + \mathrm{c} = 0 \tag{3.102}$$

with

$$\begin{cases} \mathrm{a} = \delta_1 \left(2\delta_1 \mathcal{M}_1 D_d^2 - \mathcal{K}_1 D_v^2\right) \\ \mathrm{b} = -4h\delta_1 \mathcal{M}_1 D_d^2 \\ \mathrm{c} = h^2 \left(\mathcal{K}_1 {D_v}^2 + 2\mathcal{M}_1 {D_d}^2\right) \end{cases} \quad \text{and} \quad \delta_1 = \frac{3\alpha^2 \mathcal{K}_1}{2\lambda} \tag{3.103}$$

It can be verified that the existance of solutions to (3.102) requires that,

$$\Delta = 2(1-\delta_1)\mathcal{M}_1 D_d^2 + \mathcal{K}_1 D_v^2 \geq 0 \tag{3.104}$$

If this condition is satisfied, (3.102) has a priori the following solutions:

$$\mathcal{A} = h\left(1 + \frac{1-\delta_1}{\delta_1}\left(1 + \epsilon\sqrt{\frac{\mathcal{K}_1}{\delta_1 \Delta}}|D_v|\right)^{-1}\right) \quad \text{with} \quad \epsilon = \pm 1 \tag{3.105}$$

We first assume that $\delta_1 < 1$ which ensures that $\Delta > 0$ enforcing the condition,

$$\sqrt{\frac{\delta_1 \mathcal{K}_1}{\Delta}}|D_v| < 1 \tag{3.106}$$

The two solutions given in (3.105) have opposite signs. Recalling(3.53), the appropriate solution $\mathcal{A} = \mathcal{F}/(\rho\chi)$ must also be negative. Thus the only appropriate solution with $\epsilon = -1$ reads,

$$\mathcal{A} = h\left(1 + \frac{1-\delta_1}{\delta_1}\left(1 - \sqrt{\frac{\mathcal{K}_1}{\delta_1 \Delta}}|D_v|\right)^{-1}\right) \tag{3.107}$$

Then, the condition $v_t^{av} \geq 0$ refering to (3.77) together with (3.106) yiled that D_v must be positive. Therefore, it then appears that the negative solution in (3.102) is given by,

$$\mathcal{A} = h\left(1 + \frac{1-\delta_1}{\delta_1}\left(1 - \sqrt{\frac{\mathcal{K}_1}{\delta_1 \Delta}}D_v\right)^{-1}\right) \tag{3.108}$$

Recalling (3.50) we have:

$$\mathcal{F} = \mathcal{A}\rho\chi = \mathcal{A}\frac{-\alpha Y}{v_t^{av}}\frac{\mathcal{K}_1}{\mathcal{K}_0} \tag{3.109}$$

According to (3.74) and (3.69), the mean stress Σ_m and the deviatoric stress Σ_d are then determinated respectively,

$$\Sigma_m = \lambda(\mathcal{A}\rho\chi + h) \tag{3.110}$$

$$\Sigma_d = 2\mu^{\mathrm{hom}} D_d = 2r_0(\mathcal{M}_0 K_n + \mathcal{M}_1 K_t) D_d \tag{3.111}$$

where μ^{hom} is derived from (3.11). In the limit cases $a \to 0$ (the local flow rule is asymptotically satisfied) and $\rho \to 0$, substituting K_n and K_t in (3.111) by (3.50) thus we have:

$$\Sigma_d = -2\alpha\mathcal{M}_0\mathcal{A}\chi\frac{D_d}{v_t^{av}/r_0} \tag{3.112}$$

Introducing (3.76), (3.77) into (3.110) (3.112), we have

$$\begin{aligned}
\Sigma_m &= \lambda(\mathcal{A}\rho\chi + h) && (3.113)\\
\Sigma_d &= 2\lambda h\frac{\mathcal{M}_0}{\mathcal{K}_0}\left(1-\frac{\mathcal{A}}{h}\delta_1\right)\frac{D_d}{D_v} && (3.114)
\end{aligned}$$

Eliminating D_v/D_d in (3.114) by using (3.104) and (3.108), then combining with (3.114) yields the strength criterion,

$$\forall\Sigma_m \leq \lambda h \quad , \quad \Sigma_d = \beta\left(\lambda h - \Sigma_m\right) \tag{3.115}$$

where the coefficient β is defined as:

$$\beta = \frac{\sqrt{2\delta_1}}{\sqrt{\mathcal{M}_1\mathcal{K}_1}}\frac{\mathcal{M}_0}{\rho} \tag{3.116}$$

Consequently, in the case of $\rho \to 0$, the coefficient β defined in (3.116) tends to infinity ($\beta \to \infty$), $\forall\phi_o < 1/3$. Therefore, the macroscopic strength is defined by,

$$\Sigma_m \leq \lambda h \tag{3.117}$$

We then assume that $\delta_1 > 1$. The two solutions are given by (3.105) provided that $\Delta \geq 0$. According to (3.104), this condition reads:

$$\sqrt{\frac{\delta_1\mathcal{K}_1}{\Delta}}|D_v| > 1 \tag{3.118}$$

Combining (3.77) and (3.105), and recalling that $\mathcal{A} \leq 0$, the condition $v_t^{av} \geq 0$ amounts to $\epsilon D_v < 0$, that is, $\epsilon = -D_v/|D_v|$. Accordingly, the negative appropriate solution to (3.102) is again given by (3.108). Finally, the macroscopic strength criterion (3.117) is obtained.

3.4 Application

The present section is devoted to the application of theoretical macroscopic strength criteria of granular materials derived in the previous section. To begin with, let us point out that the granular material grain-to-grain contact fraction λ, defined in (3.23), is related to a contact surface fraction ω. Recalling (3.31), we have:

$$\lambda = (1-\phi_0)\frac{r_0}{3}\frac{\sum_{i=1}^{\mathcal{N}}|\partial\mathcal{G}_i|}{\sum_{i=1}^{\mathcal{N}}|\mathcal{G}_i|}\cdot\frac{\sum_{i=1}^{\mathcal{N}}|\partial\mathcal{G}_i^s|}{\sum_{i=1}^{\mathcal{N}}|\partial\mathcal{G}_i|} = (1-\phi_0)\omega \tag{3.119}$$

where

$$\frac{\sum_{i=1}^{\mathcal{N}}|\partial\mathcal{G}_i|}{\sum_{i=1}^{\mathcal{N}}|\mathcal{G}_i|} = \frac{3}{r_0} \tag{3.120}$$

$$\frac{\sum_{i=1}^{\mathcal{N}}|\partial\mathcal{G}_i^s|}{\sum_{i=1}^{\mathcal{N}}|\partial\mathcal{G}_i|} = \omega \tag{3.121}$$

For the granular material, the contact surface fraction ω reads,

$$\omega = \frac{ZA_c}{4\pi r_0^2} \tag{3.122}$$

Parameter A_c is estimated as the contact area between two spherical grains, with characteristic radius r_0, within a granular assembly of porosity ϕ_0 according to ([Helle et al.,85],[Fleck,95]):

$$A_c = \frac{\pi}{3}\frac{\phi_{max}-\phi_0}{\phi_{max}}r_0^2 \tag{3.123}$$

Assuming a cubic lattice of a monodisperse granular assembly, we have $\phi_{max} \approx 1/2$ and the number of contacts is $Z \approx 12(1-\phi_0)$ (see [Artz,82]). In this case, the grain-to-grain fraction λ, defined in (3.119) reduces to as ([Maalej et al.,09],[Maalej,07]):

$$\lambda = (1-\phi_0)^2(1-2\phi_0) \tag{3.124}$$

Following the results derived in the previous section, the definition of the macroscopic strength criterion depends upon the initial pore volume fraction:

> When $\phi_0 < 1/3$, according to (3.117) the macroscopic strength is defined by $\Sigma_m \leq \lambda h$.
>
> When $1/3 < \phi_0 < 1/2$, the macroscopic strength criterion of granular materials depends upon the position of the interface friction coefficient α with respect to the critical value α^{crit} defined in (3.98). Using Eqs (3.14) and (3.124), the critical value α^{crit}, defined in (3.98), can be determined as:
>
> $$\alpha^{crit} = \sqrt{\frac{\phi_0(3\phi_0-1)(1-\phi_0)}{2}} \tag{3.125}$$

This critical value has also been derived by using another methodology in [Dormieux et al.,10]. While in [Dormieux et al.,10] the failure takes place in cohesionless interfaces ($T_t + \alpha T_n \leq 0$), the macroscopic strength of the granular material vanishes for $\alpha < \alpha^{crit}$ and $1/3 < \phi_0 < 1/2$. By contrast, the cohesive and frictional interfaces ($T_t + \alpha T_n \leq \alpha h$) considered in this paper allow to managing the definition of the homogenized strength properties of low frictional ($\alpha < \alpha^{crit}$) and highly porous ($1/3 < \phi_0 < 1/2$) granular materials.

Weakly frictional interfaces For weakly frictional contacts ($\alpha < \alpha^{crit}$), the strength criterion (3.92) is performed with the following analytical expressions of coefficients A, B, C:

$$A = -\frac{\alpha h(1-\phi_0)^2(1-2\phi_0)\sqrt{2\phi_0(3\phi_0-1)(1-\phi_0)}}{2\alpha^2 - \phi_0(3\phi_0-1)(1-\phi_0)} \tag{3.126}$$

$$B = \alpha h(1-\phi_0)(1-2\phi_0)\sqrt{\frac{3\phi_0(-1+\phi_0)}{2\alpha^2 - \phi_0(3\phi_0-1)(1-\phi_0)}} \tag{3.127}$$

$$C = \frac{2\alpha^2 h(1-\phi_0)^2(1-2\phi_0)}{2\alpha^2 - \phi_0(3\phi_0-1)(1-\phi_0)} \tag{3.128}$$

For granular materials defined by $\phi_0 = 0.45$ ($\alpha^{crit} \approx 0.2081$) the corresponding elliptic envelopes are plotted in the mean-deviatoric stress plan for different values of α ($\alpha < \alpha^{crit}$) (see Fig.3.4). These results clearly exhibit the increase of the macroscopic strength domain with increasing value of α ($\alpha < \alpha^{crit}$). Besides the macroscopic isotropic tensile strength also increases with α according to (3.126) and (3.128).

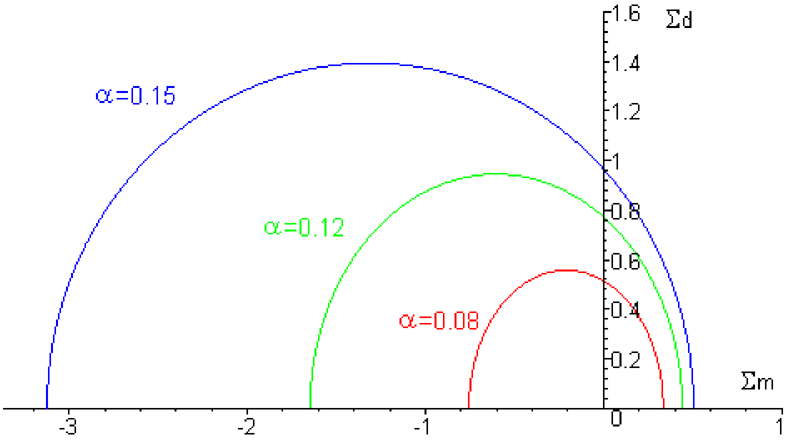

Figure 3.4: Elliptic macroscopic strength criterion (with porosity $\phi_0 = 0.45$ and $h = 40$), α is the coefficient of internal friction at interfaces

Strongly frictional interfaces For strongly frictional contacts ($\alpha > \alpha^{crit}$), the strength criterion (3.94) is now applied with the following analytical expressions of coefficients A' and B':

$$A' = \frac{\alpha h(1-\phi_0)^2(1-2\phi_0)\sqrt{2\phi_0(3\phi_0-1)(1-\phi_0)}}{2\alpha^2-\phi_0(3\phi_0-1)(1-\phi_0)} \tag{3.129}$$

$$B' = \alpha h(1-\phi_0)(1-2\phi_0)\sqrt{\frac{3\phi(1-\phi_0)}{2\alpha^2-\phi_0(3\phi_0-1)(1-\phi_0)}} \tag{3.130}$$

Still considering $\phi_0 = 0.45$, the corresponding hyperbolic envolopes are plotted in Fig.3.5 for different values of α ($\alpha > \alpha^{crit}$). Still, the greater the coefficient of internal friction α the greater the macroscopic strength. Moreover, the hyperbolic definition of the strength criterion ensures the increase of the macroscopic strength properties for increasing confining pressure. In Fig.3.6, the transition from weak to strong frictional interfaces definition is sketched for granular materials with initial porosity $\phi_0 = 0.45$.

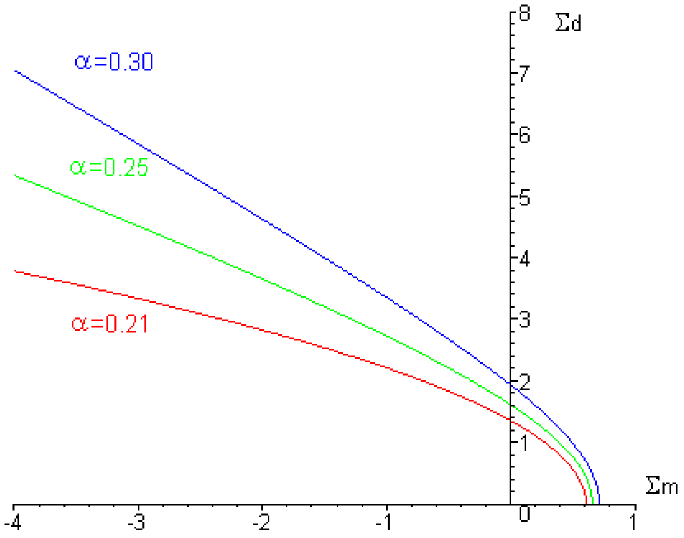

Figure 3.5: Hyperbolic macroscopic strength criterion (with porosity $\phi_0 = 0.45$ and $h = 40$), α is the coefficient of internal friction at interfaces

Influence of the initial porosity ϕ_0 In an alternative way, by fixing the critical frictional coefficient, for instance $\alpha^{crit} = 0.2$, a corresponding critical value of the pore volume fraction ϕ_0^{crit} can be calculated from (3.125) which reads here $\phi_0^{crit} \approx 0.4415$. In the case of 'lower porosity' ($\phi_0 < \phi_0^{crit}$ equivalent to $\alpha < \alpha^{crit}$), the material obeys the criterion of elliptic shape (3.92); in the case of 'higher porosity' ($\phi_0 > \phi_0^{crit}$ equivalent to $\alpha > \alpha^{crit}$), the

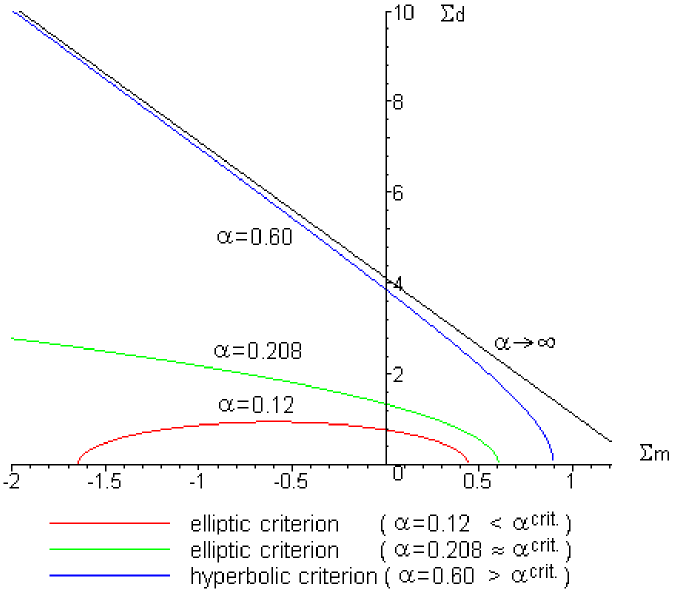

Figure 3.6: Transition of the strength criteria according to different α (with porosity $\phi_0 = 0.45$ and $h = 40$), α is the coefficient of internal friction at interfaces

material obeys the criterion of hyperbolic shape (3.94). A transition of the strength criteria (with $h = 40$) for different values of ϕ_0 is obtained and shown in Fig.3.7.

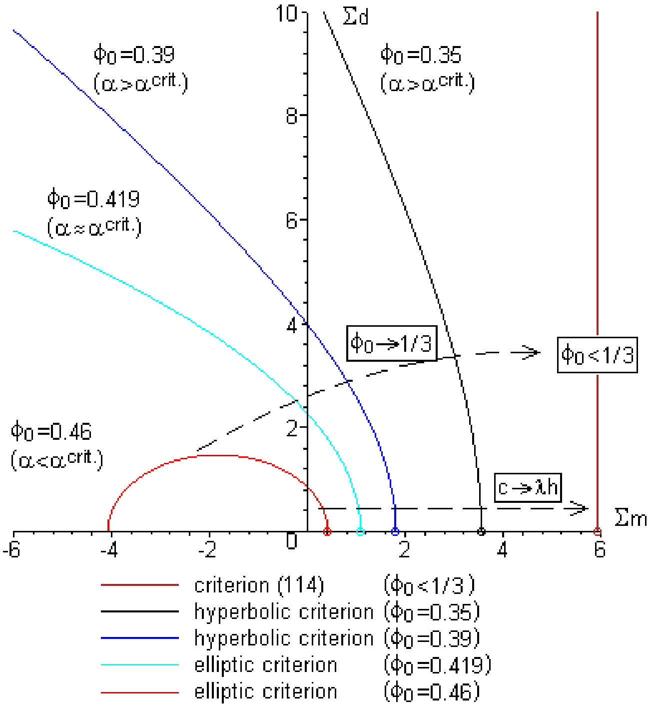

Figure 3.7: Transition of the macroscopic strength criteria according to different porosity ϕ_0 (with $\alpha^{crit} = 0.2$ and $h = 40$), $\alpha^{crit.}$ is the critical frictional coefficient

3.5 Conclusion

Strength criteria of materials with cohesive Mohr-Coulomb type interfaces have been investigated in this paper.

In the framework of the Limit Analysis theory, it has been demonstrated that the solution of a sequence of visco-plastic problems leads asymptotically to the set of macroscopic limit stress states [Barthelemy and Dormieux,04]. Introduction of a cohesive Mohr-Coulomb strength criterion at interfaces modifies the usual analysis of materials with interface effects. Based on the solution established for the prestressed poroelastic problem [He et al.,2], a modified secant homogenization method has been performed. Following [He et al.,2], the micromechanical approach proposed here predicts a macroscopic response for materials with granular-based microstructure having a pore volume fraction $\phi_0 < 1/2$. For materials defined by $\phi_0 < 1/3$, the macroscopic strength is defined by (3.117) suggesting that the macroscopic strength domain is infinite when $\Sigma_m \leq \lambda h$. For materials satisfying $1/3 < \phi_0 < 1/2$, a transition of the macroscopic strength envelopes in the mean stress-deviatoric stress plan has been derived depending upon the internal friction coefficient α of interfaces. The latter relies on the definition of a critical value denoted by α^{crit} appearing as a function of ϕ_0. When $\alpha < \alpha^{crit}$, the macroscopic strength criterion is of elliptic shape (3.92). When $\alpha > \alpha^{crit}$, the macroscopic strength criterion is of hyperbolic shape (3.94). Moreover, when $\alpha > \alpha^{crit}$, the macroscopic strength criterion tends toward a Drucker-Prager criterion for infinite values of the macroscopic confining pressure.

Bibliography

[Artz,82] Artz E. The influence of an increasing particle co-ordination on the densification of spherical powders. Acta Metallica, 30, 1883–1890, 1982.

[Barthelemy and Dormieux,03] Barthelemy J.-F. and Dormieux L. Determination of the macroscopic strength criterion of a porous medium by nonlinear homogenization. Comptes Rendus Mecanique, 331(4), 271 – 276, 2003.

[Barthelemy and Dormieux,04] Barthelemy J.-F. and Dormieux L. A micromechanical approach to the strength criterion of drucker-prager materials reinforced by rigid inclusions. International Journal for Numerical and Analytical Methods in Geomechanics, 28(7-8), 565–582, 2004.

[Coussy,03] Coussy O. Poromechanics. Wiley, 2003.

[Dormieux et al.,02] Dormieux L., Molinari A., and Kondo D. Micromechanical approach to the behavior of poroelastic materials. Journal of the Mechanics and Physics of Solids, 50(10), 2203 – 2231, 2002.

[Dormieux et al.,06] Dormieux L., Barthelemy J.-F., and Maghous S. Resistance d'un composite a renforts rigides : le cas d'une matrice de drucker-prager avec regle d'ecoulement plastique non associee. Comptes Rendus Mecanique, 334(2), 111 – 116, 2006.

[Dormieux et al.,07] Dormieux L., Sanahuja J., and Maalej Y. Strength of a polycrystal with imperfect intergranular interfaces. Comptes Rendus Mecanique, 335, 25–31, 2007.

[Dormieux et al.,06b] Dormieux L., Kondo D., and Ulm F.-J. Microporomechanics. Wiley, 2006.

[Dormieux et al.,10] Dormieux L., Jeannin L., Bemer E., Le T., and Sanahuja J. Micromechanical models of the strength of a sandstone. International Journal for Numerical and Analytical Methods in Geomechanics, 34(3), 249–271, 2010.

[Fleck,95] Fleck N. On the cold compaction of powders. Journal of the Mechanics and Physics of Solids, 43, 1409–1431, 1995.

[Hashin,91] Hashin Z. The spherical inclusion with imperfect interface. Journal of Applied Mechanics, 58, 444–449, 1991.

[He et al.,2] He Z., Dormieux L., Lemarchad E., and Kondo D. A poroelastic model for the effective behavior of granular materials with interface effect. Mechanics Research Communications, 43, 41–46, 2012.

[Helle et al.,85] Helle A.-S., Easterling K.-E., and Ashby M.-F. Hot-isostatic pressing diagrams: new developments. Acta Metallica, 33, 2163–2174, 1985.

[Kreher,90] Kreher W, Residual stresses and stored elastic energy of composites and polycrystals. J Mech Phys Solids 38, 115–128, 1990.

[Leblond et al.,94] Leblond G., JB.Perrin and Suquet P. Exact results and approximate models for porous viscoplastic solids. International Journal of Plasticity, 10, 213–235, 1994.

[Maalej,07] Maalej Y. Comportement mecanique d'un milieu granulaire injecte par un coulis de ciment- etude experimentale et modelisation micromecanique. PhD thesis, ENPC, 2007.

[Maalej et al.,09] Maalej Y., Dormieux L., and Sanahuja J. Micromechanical approach to the failure criterion of granular media. European Journal of Mechanics - A/Solids, 28(3), 647 – 653, 2009.

[Maghous et al.,09] Maghous S., Dormieux L., and Barthelemy J. Micromechanical approach to the strength properties of frictional geomaterials. European Journal of Mechanics - A/Solids, 28(1), 179 – 188, 2009.

[Salencon,90] Salencon J. An introduction to the yield design theory and its applications to soil mechanics. European journal of mechanics. A. Solids, 9, 477–500, 1990.

[Suquet,97] Suquet P. Effective behavior of nonlinear composites. In: Continuum Micromechanics. Springer-Verlag, 1997.

[Zaoui,97] Zaoui A. Structural morphology and constitutive behavior of microheterogeneous materials. In: Suquet, P. (Ed.), Continuum Micromechanics., pages 291–347, 1997.

Chapter 4

Strength properties of a porous medium reinforced by rigid particles

Contents

Rappels du contenu

Pour la transition 'micro-macro' complète en vue de l'application à l'argilite du Callovo-Oxfordien, un modèle de type Gurson étendu est proposé. Dans le modèle, l'argilite du Callovo-Oxfordien a été considérée comme un matériau composite constitué d'inclusions rigides noyées dans une matrice d'argile poreuse. La matrice d'argile elle même est décrite comme un matériau poreux constitué d'une phase solide de type Drucker-Prager et de pores sphériques. La taille des pores est supposée très faible par rapport à celle d'inclusions rigides. L'homogénéisation a pu ainsi être réalisée en deux étapes différentes. Pour la première étape 'micro-méso' concernant la transition 'micro-méso' on adopte des résultats de la litterature proposés par [Maghous et al.,09]. La deuxième étape portant sur la transition 'méso-macro' (voir Fig.4.1(a)) est la partie principale de ce chapitre. Dans le cadre de la théorie de l'analyse limite, compte tenu de la matrice plastique compressible, ce chapitre met l'accent sur une approche cinématique réalisée sur le modèle de sphère avec noyau rigide à l'échelle mésoscopique (intermédiaire). Ceci fournit une borne supérieure du critère de résistance macrscopique pour composite.

Le critère dérivé a été comparé avec celui établi à l'aide d'une approche variationnelle [Shen,11]. Un très bon accord est obtenu pour des états de contrainte isotrope. En revanche, un écart important entre les enveloppes de rupture est observé sur la résistance en cisaillement pour les grandes valeurs de la fraction volumique d'inclusions rigides. La précision de l'estimation de la résistance sous chargements isotropes a été confirmée par une comparaison avec les résultats d'une approche statique. Il est intéressant de noter que les estimations de la résistance isotrope en traction ou en compression, peu dependentes de la fraction d'inclusion, également de la méthode d'homogénéisation. La conséquence pratique est que les propriétés de résistance isotropes de la matrice d'argile et de l'argilite sont très proches, quelle que soit la teneur en quartz / calcite. Par ailleurs, la restriction du modèle au cas de Von Mises solide a été détaillée. La précision de l'estimation analytique est obtenue dans ce cas est évaluée grâce à une comparaison avec les prédictions correspondantes du modèle de [Shen,11], [Garajeu and Suquet,97]. Enfin, il est constaté que le critère proposé fournit bonne estimation de résistance sous un chargement déviatorique, en comparant avec les données expérimentales.

Ce chapitre a fait l'objet d'une publication soumise à une revue internationale, et dont le titre est 'Strength properties of a Drucker-Prager porous medium reinforced by rigid particles'

4.1 Introduction

For ductile porous media, Gurson [Gurson,77] has derived a celebrated strength criterion based on a kinematic approach of limit analysis performed on a 'hollow sphere model' in which the solid is rigid-plastic and obeys a von Mises criterion. This criterion is exact for spherical stress states, but proves less accurate for low stress triaxialities. In turn, the variational method of nonlinear homogenization [PonteCastaneda,91] provides an alternative approach to the effective strength criterion of ductile porous media which improves the prediction of the strength under shear loading, but is less efficient for spherical stress states. Using these two types of micromechanical approaches, a number of contributions have followed these pioneering criteria, by considering more refined trial velocity field [Monchiet et al.,11], or by incorporating void shape effects [Gologanu et al.,93] [Gologanu et al.,94] [Gologanu et al.,97] [Garajeu et al.,00] [Monchiet et al.,07], or considering plastic anisotropy in the solid matrix [Liao et al.,97] [Benzerga and Besson 01] (see also [Monchiet et al.,08] or [Keralavarma and Benzergar,10] for the void shape effect on the plastic deformation of anisotropic porous solids). In addition to these works, mention can be made of very recent studies devoted to porous materials with matrix exhibiting asymmetry between tension and compression [Cazacu and Stewart,09]. It must be noted that all these theories deal with incompressible plastic matrix. Interestingly, porous media with compressible plastic matrix like cohesive geomaterials or porous polymers were considered by several authors among which [Jeong and Pan,95], [Lee and Oung,00], [Jeong,02], [Barthélémy and Dormieux,03], [Trillat et al.,06], [Guo et al.,08], [Vincent et al.,09], [Thore et al.,09], [Thore et al.,11], [Shen et al.,12b].

We propose a 'rigid core sphere model' in view of application to the mechanical behavior of the Callovo-Oxfordien (COx) argillite in the context of a research program initiated by the French 'National Radioactive Waste Management Agency'(ANDRA). Being hard clayey rocks, COx Argillite [Andra,05] is a kind of multi-scale porous material including plate- or sheet like structured clay aggregates, mineral phases such as quartz, calcite etc. and pores. The results of correlation between the volume fraction of clay phases and of the porosity reveal that the pores are mainly part of the clay [Robinet,12]. More precisely, two different scales can be identified (see figure 4.1). At the so-called mesoscopic scale, the COx argillite can be regarded as a clay matrix in which quartz or silica inclusions are embedded. The

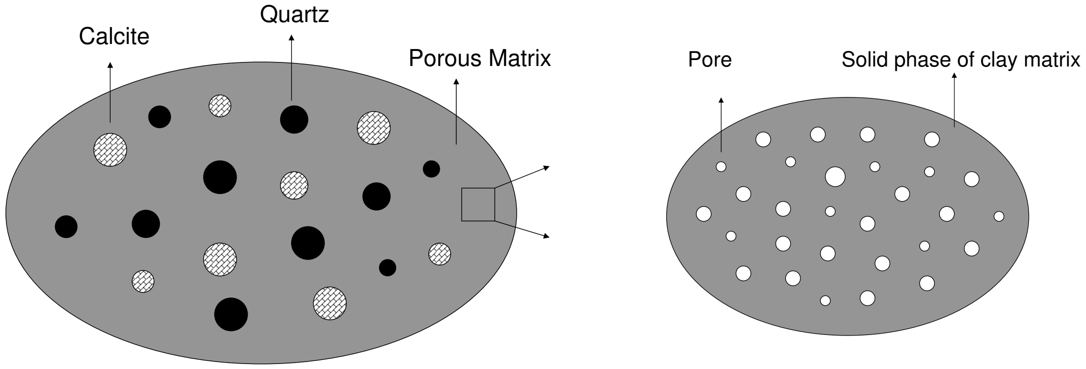

(a) argillite at meso-scale (b) porous matrix at micro-scale

Figure 4.1: Microstructure of the argillite of Callovo-Oxfordien

typical size of these mineral inclusions is some tens of μm. At this scale, the clay appears as a homogeneous material. Moreover, as compared to clay, the solid inclusions can be considered to be rigid. Based on a Hill type incremental homogenization approach, a two scale model of the COx argillite has been proposed by [Abou-Chakra et al.,08]. Despite its interest, this two scale model does not explicitly account for the microporosity of the clay matrix (which behavior has been modeled by a Drucker-Prager plasticity law). Indeed, at a refined scale, referred here to as microscopic scale, the clay phase is a porous material with microvoids embedded in a dilatant solid phase. The typical pore size is some tens of nm[1]. This confirms that the scale separation condition is satisfied. Accordingly, the micro-to-macro homogenization can be performed in two steps. The first step is the micro-to-meso transition in which the clay phase, described as a porous material, has to be homogenized. The second step deals with the meso-to-macro transition. A first approach of this two steps modeling of the COx argillite including both effects of micropores as well as that of the inclusions has been proposed by [Shen et al.,12] who follow the previous Hill incremental approach. In their model, the clay matrix is explicitly described as a Drucker-Prager solid phase containing spherical pores. Although this model delivers interesting results, the macroscopic plastic behavior is not described in closed-form constitutive relations but by means of a numerically-based implementation in the second step procedure.

In the present study, we mainly aim to derive new closed-form results for the strength of the argillite, under the assumption that the solid phase of the clay is a Drucker-Prager per-

---

[1] *Further investigations on voids size effects can be made by following the recent contribution by [Dormieux et al.,10]*

fectly plastic material. As far as the first step is concerned, the result of the homogenization is an analytical elliptic criterion ([Maghous et al.,09]) involving the first and second invariants of the mesoscopic stress tensor. We therefore focus on the second step. This question has been recently addressed in the framework of a two step variational nonlinear homogenization approach (the so called modified secant method) by [Shen,11]. The present paper explores an alternative approach which can be viewed as an extension of the original Gurson model. Instead of a spherical cavity surrounded by a matrix, the proposed 'rigid core sphere model' consists of a rigid spherical core surrounded by the homogeneous porous material whose property is determined from the first step (see figure 4.2). Hence, the shell is a compressible phase (see also [Shen,11]). The failure criterion of this 'rigid core sphere model' is derived in the framework of the kinematic approach of limit analysis (LA). It is worth noting that from the LA point of view the failure mechanism can include a strain concentration at the core-matrix interface which can be described mathematically by a velocity discontinuity.

The outline of the paper is as follows: first, the elliptic criterion for the frictional porous medium developed in [Maghous et al.,09] is recalled and the corresponding support function is derived (section 4.2). Thereafter, the overall dissipation is determined as the sum of the contributions of the matrix and of the core-matrix interface (section 4.3). The macroscopic criterion is derived in a parametric form (section 4.4). Numerical simulations of the macroscopic criterion of the COx argillite are presented. A comparison with the results of the alternative modified secant method [Shen,11] is provided (section 4.5) and some analytical results are also established (section 4.6, section4.7). Finally, we provide in an appendix the predictions of the 'rigid core sphere model' in the case of a von Mises solid phase. The results are then assessed by comparison with that of [Shen,11] and [Garajeu and Suquet,97] (Appendix 4.9).

Notations: $\mathbf{1}$ and $\mathbb{I}$ are the second and fourth order identity tensors. $\mathbb{J} = \frac{1}{3}\mathbf{1} \otimes \mathbf{1}$, $\mathbb{K} = \mathbb{I} - \mathbb{J}$ are respectively the spherical and deviatoric projectors of isotropic fourth order symmetric tensor.

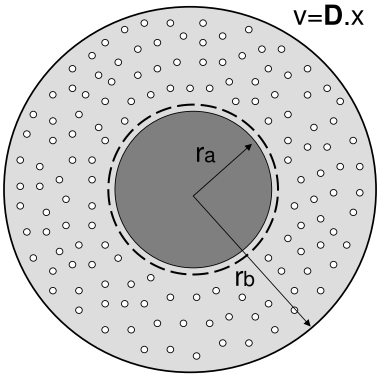

Figure 4.2: 'Rigid core sphere model'

4.2 The micro-to-meso transition: elliptic criterion and support function of porous matrix

The first homogenization step approach starts at the microscopic scale. At this scale, the porous clay matrix is described as a heterogeneous material being made up of a Drucker-Prager perfectly plastic solid in which pores are embedded. Let $\tilde{\boldsymbol{\sigma}}_d = \tilde{\boldsymbol{\sigma}} - \tilde{\sigma}_m \mathbf{1}$ denote the deviatoric part of the stress tensor $\tilde{\boldsymbol{\sigma}}$ at the microscopic scale. The scalar deviatoric stress $\tilde{\sigma}_d$ and mean stress $\tilde{\sigma}_m$ are defined as $\tilde{\sigma}_d = \sqrt{\tilde{\boldsymbol{\sigma}} : \mathbb{K} : \tilde{\boldsymbol{\sigma}}}$ and $\tilde{\sigma}_m = (\mathbf{1} : \mathbb{J} : \tilde{\boldsymbol{\sigma}})/3$ and the Drucker-Prager criterion reads:

$$\tilde{\sigma}_d + T(\tilde{\sigma}_m - h) \leq 0 \tag{4.1}$$

The parameters T and h respectively characterize the friction coefficient and the tensile strength of the solid phase of the clay matrix.

The result of the first homogenization step is the derivation of the strength properties of the porous clay matrix at the mesoscopic scale where it is described as a homogeneous material. These properties were estimated successfully in [Maghous et al.,09] by means of the modified secant method. Now $\boldsymbol{\sigma}_d = \boldsymbol{\sigma} - \sigma_m \mathbf{1}$ denotes the deviatoric part of the stress tensor $\boldsymbol{\sigma}$ at the mesoscopic scale and we introduce $\sigma_d = \sqrt{\boldsymbol{\sigma} : \mathbb{K} : \boldsymbol{\sigma}}$ and $\sigma_m = (\mathbf{1} : \mathbb{J} : \boldsymbol{\sigma})/3$. In the situation of associated plasticity, the domain of admissible stress states is an ellipse in the (σ_m, σ_d)-plane:

$$F^{\text{meso}}(\boldsymbol{\sigma}, f, T) = \frac{1 + 2f/3}{T^2}\sigma_d^2 + \left(\frac{3f}{2T^2} - 1\right)\sigma_m^2 + 2(1-f)h\sigma_m - (1-f)^2h^2 \leq 0 \tag{4.2}$$

Note that $0 < T \leq \sqrt{3f/2}$ (see [Maghous et al.,09]). At the mesoscopic scale, the clay matrix is described by the elliptic criterion (4.2). It will be useful to consider a general expression reading:

$$\mathcal{F}(\boldsymbol{\sigma}, f, T) = \mathrm{a}\sigma_m^2 + \mathrm{b}\sigma_d^2 + \mathrm{c}\sigma_m - \mathrm{d}^2 \leq 0 \tag{4.3}$$

(4.2) is retrieved with the following parameters:

$$\mathrm{a} = \frac{3f - 2T^2}{2T^2}, \quad \mathrm{b} = \frac{1 + 2f/3}{T^2}, \quad \mathrm{c} = 2(1-f)h, \quad \mathrm{d} = (1-f)h \tag{4.4}$$

In turn (4.3) can be put in the form $\mathcal{G}(\boldsymbol{\sigma} - \sigma_c \mathbf{1}) \leq 0$ where

$$\mathcal{G}(\boldsymbol{\sigma}, f, T) = (\frac{\sigma_m}{L})^2 + \frac{1}{2}{\sigma_d}^2 - k^2 \tag{4.5}$$

with

$$\sigma_c = -\frac{\mathrm{c}}{2\mathrm{a}} \quad ; \quad L^2 = \frac{2\mathrm{b}}{\mathrm{a}} \quad ; \quad k^2 = \frac{d^2 + \sigma_c^2 \mathrm{a}}{2\mathrm{b}} \tag{4.6}$$

In the framework of limit analysis theory (see e.g. [Salencon,90]), a dual characterization of the strength criterion $\mathcal{F}(\sigma) \leq 0$ is the support function $\pi_{\mathcal{F}}(\mathbf{d}) = \sup(\boldsymbol{\sigma} : \mathbf{d}, \mathcal{F}(\boldsymbol{\sigma}) \leq 0\}$ of the convex set of admissible stress states. First, the support function $\pi_{\mathcal{G}}(\mathbf{d})$ of the domain $\mathcal{G}(\boldsymbol{\sigma}, f, T) \leq 0$ (see (4.5)) reads (see e.g. [Dormieux et al.,06b]):

$$\pi_{\mathcal{G}}(\mathbf{d}) = 2k\sqrt{\frac{L^2}{4}d_v^2 + \frac{1}{2}d_d^2} \tag{4.7}$$

with

$$d_v = \mathrm{tr}\ \mathbf{d} \quad ; \quad d_d = \sqrt{\mathbf{d}_d : \mathbf{d}_d} \quad ; \quad \mathbf{d}_d = \mathbf{d} - d_v \mathbf{1} \tag{4.8}$$

Since $\mathcal{F}(\boldsymbol{\sigma}) \leq 0 \Leftrightarrow \mathcal{G}(\boldsymbol{\sigma} - \sigma_c \mathbf{1}) \leq 0$, it is readily seen that $\pi_{\mathcal{F}}(\mathbf{d})$ and $\pi_{\mathcal{G}}(\mathbf{d})$ are related according to

$$\pi_{\mathcal{F}}(\mathbf{d}) = \pi_{\mathcal{G}}(\mathbf{d}) + \sigma_c d_v \tag{4.9}$$

Combining (4.4), (4.6), (4.7) and (4.9), the support function $\pi(\mathbf{d})$ associated with (4.2) of the porous matrix finally takes the form

$$\pi_{\mathcal{F}}(\mathbf{d}) = (1-f)h\sqrt{\frac{3f}{3f - 2T^2}\frac{T^2}{1 + 2f/3}}\sqrt{\frac{1 + 2f/3}{3f/2 - T^2}d_v^2 + d_d^2} - (1-f)h\frac{2T^2}{3f - 2T^2}d_v \tag{4.10}$$

For the further derivations in this paper, (4.10) can be simplified as follows,

$$\pi_{\mathcal{F}}(\mathbf{d}) = \sigma_0 d_{EQ} - \lambda d_v \qquad \text{with} \quad d_{EQ} = \sqrt{\frac{2}{3}\mathbf{d} : \mathbb{H} : \mathbf{d}} \tag{4.11}$$

with

$$\sigma_0 = (1-f)h\sqrt{\frac{3}{2}}\sqrt{\frac{3f}{3f-2T^2}\frac{T^2}{1+2f/3}} \quad ; \quad \lambda = (1-f)h\frac{2T^2}{3f-2T^2} \tag{4.12}$$

where $\mathbb{H} = \frac{1}{\alpha}\mathbb{J} + \mathbb{K}$ is a fourth order tensor, with

$$\alpha = \frac{3f/2 - T^2}{3+2f} \tag{4.13}$$

4.3 Overall dissipation at the mesoscopic scale

We now focus on the transition from the mesoscopic scale to the macroscopic scale which constitutes the second homogenization step and is the main subject of the present paper. We seek the macroscopic criterion by means of a Gurson-type approach. As already stated, the microstructure at the mesoscopic scale is described by a composite sphere Ω with a rigid core surrounded by the homogenized clay resulting from the micro-to-meso transition (see figure 4.2). The external (resp. internal) radius is denoted by r_e (resp. r_i). The shell Ω_m ($r_i \leq r \leq r_e$) around the core represents the clay. The volume fraction $\rho = (r_i/r_e)^3$ of the core in the composite sphere is equal to the volume fraction of the rigid inclusions in a representative volume element of argillite.

4.3.1 Velocity field at the mesoscopic scale

As done in the classical approach, we then apply uniform strain rate boundary conditions on the external surface $r = r_e$ corresponding to the macroscopic strain rate tensor $\mathbf{D}$:

$$(\forall \underline{e}_r) \quad \underline{v}(r_e\underline{e}_r) = \mathbf{D}\cdot r_e\underline{e}_r \tag{4.14}$$

In order to take into account the compressibility of the clay, the velocity field used in the classical Gurson approach [Gurson,77] must be modified. We therefore combine a radial expansion with a Gurson velocity field:

$$r \geq r_i : \underline{v}(\underline{x}) = A\underline{x} + \underline{v}^G(\underline{x}) \tag{4.15}$$

$A\underline{x}$ denotes the compressible component of the velocity field while the incompressible Gurson component $\underline{v}^G$ (incompressible matrix) involves a scalar constant B and a purely deviatoric tensor $\mathbf{D}'$ ($\operatorname{tr}\mathbf{D}' = 0$):

$$r \geq r_i : \underline{v}^G(\underline{x}) = B\frac{r_e^3}{r^2}\underline{e}_r + \mathbf{D}'\cdot\underline{x} \quad \text{with} \quad \underline{x} = r\underline{e}_r \tag{4.16}$$

(4.14) implies that $\mathbf{D}'$ must be the deviatoric part $\mathbf{D}_d$ of $\mathbf{D}$ as well as the condition $A+B=D_m$. Accordingly, we have a family of kinematically admissible (k.a.) velocity fields with $\mathbf{D}$, depending on one parameter A:

$$r \geq r_i : \quad \underline{v}_A = A\underline{x} + (D_m - A)\frac{r_e^3}{r^2}\underline{e}_r + \mathbf{D}_d \cdot \underline{x} \tag{4.17}$$

The strain rate in the clay ($r_i \leq r \leq r_e$) can be determined from (4.17):

$$\mathbf{d}_A = A\mathbf{1} + \mathbf{D}_d + (D_m - A)\frac{r_e^3}{r^3}\left(\mathbf{1} - 3\underline{e}_r \otimes \underline{e}_r\right) \tag{4.18}$$

From (4.18), with $D_d^2 = \mathbf{D_d} : \mathbf{D_d}$, the expression of d_{EQ} in (4.11) can be written as

$${d_{EQ}}^2 = \frac{2A^2}{\alpha} + 4(D_m - A)^2\frac{r_e^6}{r^6} + \frac{2D_d^2}{3} + \frac{4(D_m - A)}{3}\frac{r_e^3}{r^3}\mathbf{D}_d : (\mathbf{1} - 3\underline{e}_r \otimes \underline{e}_r) \tag{4.19}$$

The velocity is $\underline{v}_O = 0$ in the rigid core. Note that the condition $\underline{v}_A = 0$ on the core boundary $r = r_i$ cannot be fulfilled by the velocity field defined in (4.17). This implies that the dissipation associated with a discontinuity of velocity must be considered at the boundary I ($r = r_i$) (see section 4.3.4).

4.3.2 Macroscopic support function

Defining the macroscopic strength domain G^{hom} as the set of admissible macroscopic stress states $\mathbf{\Sigma}$, the macroscopic support function reads $\Pi^{\text{hom}}(\mathbf{D}) = \sup(\mathbf{\Sigma} : \mathbf{D}, \mathbf{\Sigma} \in G^{\text{hom}})$. Considering the set $\mathcal{K}$ of k.a. velocity fields with $\mathbf{D}$, $\Pi^{\text{hom}}(\mathbf{D})$ is characterized as [Leblond et al.,94]:

$$\Pi^{\text{hom}}(\mathbf{D}) = \frac{1}{|\Omega|}\inf_{\underline{v}\in\mathcal{K}}\left(\int_{\Omega_m}\pi_{\mathcal{F}}(\mathbf{d}_A)\,dV + \int_I \pi([\![\underline{v}_A]\!])\,dS\right) \tag{4.20}$$

where $|\Omega| = 4\pi r_e^3/3$. In the surface integral, $[\![\underline{v}]\!]$ denotes the velocity discontinuity at the core boundary I and $\pi([\![\underline{v}]\!])$ represents the associated surface density of dissipation. In the line of reasoning of Gurson approach, $\Pi^{\text{hom}}(\mathbf{D})$ is approximated by the minimal dissipation obtained among the velocity fields $\underline{v}_A$ defined in (4.17):

$$\Pi^{\text{hom}}(\mathbf{D}) = \frac{1}{|\Omega|}\inf_{A\in\mathbb{R}}\left(\int_{\Omega_m}\pi_{\mathcal{F}}(\mathbf{d}_A)\,dV + \int_I \pi([\![\underline{v}_A]\!])\,dS\right) \tag{4.21}$$

For further use, let us introduce the following notation:

$$\frac{1}{|\Omega|}\int_{\Omega_m}\pi_{\mathcal{F}}(\mathbf{d}_A)\,dV = \tilde{\Pi}^{\text{m}}(\mathbf{D}, A) \quad ; \quad \frac{1}{|\Omega|}\int_I \pi([\![\underline{v}_A]\!])\,dS = \tilde{\Pi}^I(\mathbf{D}, A) \tag{4.22}$$

and

$$\tilde{\Pi}(\mathbf{D}, A) = \tilde{\Pi}^{\text{m}}(\mathbf{D}, A) + \tilde{\Pi}^I(\mathbf{D}, A) \tag{4.23}$$

Accordingly:

$$\Pi^{\mathrm{hom}}(\mathbf{D}) = \inf_{A\in\mathbb{R}} \tilde{\Pi}(\mathbf{D}, A) \tag{4.24}$$

Once $\Pi^{\mathrm{hom}}(\mathbf{D})$ is determined, the macroscopic admissible stress states on the boundary $\partial G^{\mathrm{hom}}$ are derived according to:

$$\mathbf{\Sigma} = \frac{\partial \Pi^{\mathrm{hom}}}{\partial \mathbf{D}}(\mathbf{D}) \tag{4.25}$$

The stress state of (4.25) lies on the boundary of G^{hom} at the location where the normal is parallel to $\mathbf{D}$.

The overall dissipation of (4.23) proves to read in the following form:

$$\tilde{\Pi}(\mathbf{D}, A) = \sigma_0 \left[N \operatorname{arcsinh}\left(\frac{uN}{M}\right) - \frac{\sqrt{M^2 + u^2N^2}}{u} \right]_1^{\frac{1}{\rho}} + \sigma_0 \sqrt{\frac{2}{3}} \mathscr{Y} - 3\lambda D_m \tag{4.26}$$

with the notations introduced in (4.30), (4.39) and (4.40).

For the sake of completeness, sections 4.3.3 and 4.3.4 respectively determine the contribution (4.29) of the shell Ω_m (volume integral in (4.21)) and the contribution (4.37) of the interface I (surface integral in (4.21)) which has led to (4.26).

Section 4.4 will consider the minimization w.r.t. parameter A.

4.3.3 Contribution of the shell to dissipation

For a given value of parameter A, the contribution of the matrix to the macroscopic dissipation reads

$$\tilde{\Pi}^{\mathrm{m}}(\mathbf{D}, A) = \frac{1}{|\Omega|} \int_{\Omega_m} \left(\sigma_0 d_{EQ} - \lambda d_v \right) dV \tag{4.27}$$

In order to obtain an analytical expression of $\tilde{\Pi}^{\mathrm{m}}(\mathbf{D}, A)$, the approximation introduced in [Gurson,77] (see also [Dormieux et al.,10]) is applied. Let $\mathcal{S}(r)$ denote the sphere of radius r. As a consequence of the Cauchy-Schwarz inequality, it is readily seen that

$$\int_{\mathcal{S}(r)} d_{EQ} dS \leq \sqrt{4\pi r^2} \sqrt{\int_{\mathcal{S}(r)} d_{EQ}^2 dS} \tag{4.28}$$

We observe that the average $\langle \mathbf{1} - 3\underline{e}_r \otimes \underline{e}_r \rangle_{\mathcal{S}(r)}$ of $\mathbf{1} - 3\underline{e}_r \otimes \underline{e}_r$ over the orientations of $\underline{e}_r$ on the sphere $\mathcal{S}(r)$ is equal to 0. Then, using (4.19) and (4.28) in (4.27), $\tilde{\Pi}^{\mathrm{m}}(\mathbf{D}, A)$ reads

$$\begin{aligned} \tilde{\Pi}^{\mathrm{m}}(\mathbf{D}, A) &= \frac{4\pi\sigma_0}{\Omega} \int_{r_i}^{r_e} r^2 \sqrt{\frac{2A^2}{\alpha} + 4(D_m - A)^2 \frac{r_e^6}{r^6} + \frac{2D_d^2}{3}} dr - \frac{\lambda}{\Omega} \int_{\Omega^{\mathrm{m}}} d_v dV \\ &= \sigma_0 \left[N \operatorname{arcsinh}\left(\frac{uN}{M}\right) - \frac{\sqrt{M^2 + u^2N^2}}{u} \right]_1^{\frac{1}{\rho}} - 3(1-\rho)\lambda A \end{aligned} \tag{4.29}$$

with

$$M^2 = \frac{2A^2}{\alpha} + \frac{2D_d^2}{3}, \quad N^2 = 4(D_m - A)^2 \tag{4.30}$$

4.3.4 Inclusion-matrix interface

Unlike the classical Gurson's 'hollow sphere model', the model proposed in this paper substitutes a rigid core for the void in the center of the thick-walled sphere. Therefore, owing to null velocity ($\underline{v}_O = 0$) in the rigid core, a velocity discontinuity tales place at the core boundary: $[\![\underline{v}_A]\!] = \underline{v}_A(r_a\underline{e}_r) - \underline{v}_O = \underline{v}_A(r_a\underline{e}_r)$.

4.3.4.1 Surface density of dissipation

The velocity field $\underline{v}_A$ being discontinuous across the surface I (rigid core boundary), its gradient and the associated strain rate are to be defined in the sense of the distribution theory:

$$\mathbf{d} = \{\mathbf{d}\} + \frac{1}{2}\left(\underline{n} \otimes [\![\underline{v}_A]\!] + [\![\underline{v}_A]\!] \otimes \underline{n}\right)\delta_I \tag{4.31}$$

where $\{\mathbf{d}\}$ is the standard expression of the strain rate corresponding to its smooth part, δ_I is the Dirac distribution which support is the surface of discontinuity I and $\underline{n} = \underline{e}_r$ is the unit normal to this surface. The surface density of dissipation $\pi([\![\underline{v}_A]\!])$ contributed by the velocity jump $[\![\underline{v}_A]\!]$ is therefore related to the support function $\pi_{\mathcal{F}}$ according to (see e.g. [Salencon,90]):

$$\pi([\![\underline{v}_A]\!]) = \pi_{\mathcal{F}}(\mathbf{d}^I) \tag{4.32}$$

where $\mathbf{d}^I$ is defined as

$$\mathbf{d}^I = \frac{1}{2}\left(\underline{n} \otimes [\![\underline{v}_A]\!] + [\![\underline{v}_A]\!] \otimes \underline{n}\right) \tag{4.33}$$

Recalling (4.17) and (4.33), the strain rate $\mathbf{d}^I$ associated with the velocity jump can be obtained and written as

$$\mathbf{d}^I = r_i\left((\frac{1}{\rho}D_m + (1-\frac{1}{\rho})A)\underline{e}_r \otimes \underline{e}_r + \frac{1}{2}\left((\mathbf{D}_d \cdot \underline{e}_r) \otimes \underline{e}_r + \underline{e}_r \otimes (\mathbf{D}_d \cdot \underline{e}_r)\right)\right) \tag{4.34}$$

Eventually, the surface density of dissipation is derived from the combination of (4.32) and (4.11)

$$\pi([\![\underline{v}_A]\!]) = \sigma_0 d^I_{EQ} - \lambda d^I_v \qquad \text{with} \quad d^I_{EQ} = \sqrt{\frac{2}{3}\mathbf{d}^I : \mathbb{H} : \mathbf{d}^I} \quad ; \quad d^I_v = \mathrm{tr}\ \mathbf{d}^I \tag{4.35}$$

4.3.4.2 Contribution of the interface to dissipation

Recalling (4.27), the macroscopic dissipation related to the part of inclusion-matrix interface depending also on the scalar A can be written as

$$\tilde{\Pi}^I(\mathbf{D}, A) = \frac{1}{\Omega} \int_{r=r_i} \left(\sigma_0 d^I_{_{EQ}} - \lambda d^I_v \right) dS \tag{4.36}$$

Again, the integration of d^I_{eq} is approximated by the upper bound (4.28) which yields

$$\tilde{\Pi}^I(\mathbf{D}, A) = \sigma_0 \sqrt{\frac{2}{3}} \mathscr{Y} - \lambda \mathscr{X} \tag{4.37}$$

with

$$\mathscr{Y} = \frac{\sqrt{4\pi r_i^2}}{\Omega} \sqrt{\int_{r=r_i} \mathbf{d}^I : \mathbb{H} : \mathbf{d}^I dS} \tag{4.38}$$

Using (4.34), $\mathscr{Y}$ takes the form

$$\mathscr{Y} = \sqrt{\frac{P^2 + Q^2}{15\alpha}} \tag{4.39}$$

with

$$Q^2 = \left(\frac{51}{2}\alpha + 6 \right) \rho^2 D_d^2, \quad P^2 = 45(1+2\alpha) \left[D_m - A(1-\rho) \right]^2 \tag{4.40}$$

In turn, observing that the average $\langle \underset{\sim}{e}_r \cdot \mathbf{D}_d \cdot \underset{\sim}{e}_r \rangle_{r=r_i}$ of $\underset{\sim}{e}_r \cdot \mathbf{D}_d \cdot \underset{\sim}{e}_r$ over the orientations of $\underset{\sim}{e}_r$ on the sphere I is equal to 0, it is readily seen that

$$\mathscr{X} = \frac{1}{\Omega} \int_{\mathcal{S}(r_a)} d^I_v dS = 3 \left(D_m - A(1-\rho) \right) \tag{4.41}$$

4.4 Macroscopic criterion

The macroscopic support function can be determinated by minimizing the sum $\tilde{\Pi}(\mathbf{D}, A) = \tilde{\Pi}^{\mathrm{m}}(\mathbf{D}, A) + \tilde{\Pi}^I(\mathbf{D}, A)$ with respect to the parameter A. Accordingly, the boundary of G^{hom} is determined according to (4.25)[Monchiet et al.,07]:

$$\mathbf{\Sigma} = \frac{\partial \tilde{\Pi}(\mathbf{D}, A)}{\partial \mathbf{D}}, \qquad \text{with} \qquad \frac{\partial \tilde{\Pi}(\mathbf{D}, A)}{\partial A} = 0 \tag{4.42}$$

It is readily seen from (4.26) that $\tilde{\Pi}(\mathbf{D}, A)$ can be put in the form:

$$\tilde{\Pi}(\mathbf{D}, A) = \mathcal{P}(M, N, P, Q) - 3\lambda D_m \tag{4.43}$$

where $\mathcal{P}(M, N, P, Q)$ depends on $\mathbf{D}$ and A through the parameters M, N, P and Q. (4.42) therefore reads

$$\mathbf{\Sigma} = \frac{\partial \mathcal{P}}{\partial M} \frac{\partial M}{\partial \mathbf{D}} + \frac{\partial \mathcal{P}}{\partial N} \frac{\partial N}{\partial \mathbf{D}} + \frac{\partial \mathcal{P}}{\partial P} \frac{\partial P}{\partial \mathbf{D}} + \frac{\partial \mathcal{P}}{\partial Q} \frac{\partial Q}{\partial \mathbf{D}} - \lambda \mathbf{1} \tag{4.44}$$

with the condition of minimization with respect to A to be met simultaneously,

$$\frac{\partial\mathcal{P}}{\partial M}\frac{\partial M}{\partial A}+\frac{\partial\mathcal{P}}{\partial N}\frac{\partial N}{\partial A}+\frac{\partial\mathcal{P}}{\partial P}\frac{\partial P}{\partial A}+\frac{\partial\mathcal{P}}{\partial Q}\frac{\partial Q}{\partial A}=0 \tag{4.45}$$

(4.44) can be decomposed as $\boldsymbol{\Sigma}=\Sigma_m\mathbf{1}+\boldsymbol{\Sigma}_d$, which gives

$$\begin{aligned}\Sigma_m &= \tfrac{1}{3}\left(\Sigma_N\tfrac{\partial N}{\partial D_m}+\Sigma_P\tfrac{\partial P}{\partial D_m}\right)-\lambda\\ \boldsymbol{\Sigma}_d &= \Sigma_M\tfrac{\partial M}{\partial\mathbf{D}_d}+\Sigma_Q\tfrac{\partial Q}{\partial\mathbf{D}_d}\end{aligned} \tag{4.46}$$

knowing that N and P are only in function of D_m and A, while M and Q are only in function of $\mathbf{D}_d$ and A. Recalling (4.30) and (4.40), Σ_M, Σ_N, Σ_P, Σ_Q are derived as follows,

$$\Sigma_M=\frac{\partial\mathcal{P}}{\partial M}=\sigma_0\left(\sqrt{1+\frac{N^2}{M^2}}-\sqrt{\rho^2+\frac{N^2}{M^2}}\right) \tag{4.47}$$

$$\Sigma_N=\frac{\partial\mathcal{P}}{\partial N}=\sigma_0\left[\operatorname{arcsinh}\left(\frac{N}{\rho M}\right)-\operatorname{arcsinh}\left(\frac{N}{M}\right)\right] \tag{4.48}$$

$$\Sigma_P=\frac{\partial\mathcal{P}}{\partial P}=\sqrt{\frac{2}{45\alpha}}\frac{\sigma_0 P}{\sqrt{P^2+Q^2}} \tag{4.49}$$

$$\Sigma_Q=\frac{\partial\mathcal{P}}{\partial Q}=\sqrt{\frac{2}{45\alpha}}\frac{\sigma_0 Q}{\sqrt{P^2+Q^2}} \tag{4.50}$$

The partial derivatives of N, P to D_m and of M, Q to $\mathbf{D}_d$ read

$$\frac{\partial N}{\partial D_m}=2,\qquad \frac{\partial P}{\partial D_m}=3\sqrt{5}\sqrt{1+2\alpha} \tag{4.51}$$

$$\frac{\partial M}{\partial\mathbf{D}_d}=\frac{2\mathbf{D}_d}{3M},\quad \frac{\partial Q}{\partial\mathbf{D}_d}=\left(\frac{51\alpha}{2}+6\right)\rho^2\frac{\mathbf{D}_d}{Q} \tag{4.52}$$

The partial derivatives of M, N, P, Q to A read

$$\frac{\partial M}{\partial A}=\frac{2A}{\alpha M},\quad \frac{\partial N}{\partial A}=-2,\quad \frac{\partial P}{\partial A}=-3(1-\rho)\sqrt{5}\sqrt{1+2\alpha},\quad \frac{\partial Q}{\partial A}=0 \tag{4.53}$$

With the above equations, it was not possible to find an analytical expression of the macroscopic criterion. Hence, a numerical resolution is provided in the following. It can be seen that the parametric equations (4.45) and (4.46) depend on the two non dimensional kinematic variables $\frac{D_d}{D_m}$ and $\frac{A}{D_m}$. Note that $\frac{D_d}{D_m}$ represents the direction of plastic flow which is also the normal to the yield surface. The failure envelope of the criterion is estimated by selecting a series of discrete values $\left(\frac{D_d}{D_m}\right)_i$ from 0 to ∞. The value 0 corresponds to isotropic loading while the value ∞ is associated with pure shear. For each value of $\left(\frac{D_d}{D_m}\right)_i$, the condition (4.45) provides an implicit equation to be solved by the optimal ratio $\left(\frac{A}{D_m}\right)_i$. The mascroscopic stresses Σ_m and Σ_d are then computed from (4.46).

4.5 Comparison with the result obtained by a variational approach

Numerical simulations of the macroscopic criterion derived in the framework of the kinematic approach of limit analysis are now compared with the result obtained by the variational approach [Shen,11]. For the derivation of their criterion, these authors consider a variational approach in the two homogenization steps. Their criterion reads:

$$F^{\text{hom}}(\mathbf{\Sigma}, f, T) = \Theta\Sigma_d^2 + \left(\frac{3f}{2T^2} - 1\right)\Sigma_m^2 + 2(1-f)h\Sigma_m - \frac{3+2f+3f\rho}{3+2f}(1-f)^2h^2 = 0 \quad (4.54)$$

with

$$\Theta = \frac{\frac{1+2f/3}{T^2} + \frac{2}{3}\rho\left(\frac{3f}{2T^2} - 1\right)}{\frac{4T^2-12f-9}{6T^2-13f-6}\rho + 1} \quad (4.55)$$

Applying the parameters $f = 0.25$ and $T = 0.525$, the comparison between the results predicted by the two different methods is shown in Fig.4.3

As it can be seen in Fig.4.3, the analytical estimate (4.54) obtained by the variational approach and the present numerical simulations based on the 'rigid core sphere model' show a very good agreement for purely isotropic stress states, both in traction and compression. It is noteworthy that the strength under purely isotropic stress seems surprisingly almost unaffected by the volume fraction ρ of the rigid core.

Although the shapes of the yield surfaces predicted by the two methods are similar, the strength predicted by limit analysis always overestimates that predicted by the variational method. In particular, as far as the strength under pure shear loading is concerned, the difference becomes very important when the volume fractions of the rigid core ρ is larger. In order to gain a deeper understanding of the effect of the parameter ρ, the isotropic strength will now be compared with the exact solution predicted by the so-called static approach (sections 4.6.2, 4.6.1, 4.6.4). Thereafter, we shall focus on the strength under pure shear loading (section 4.7.1).

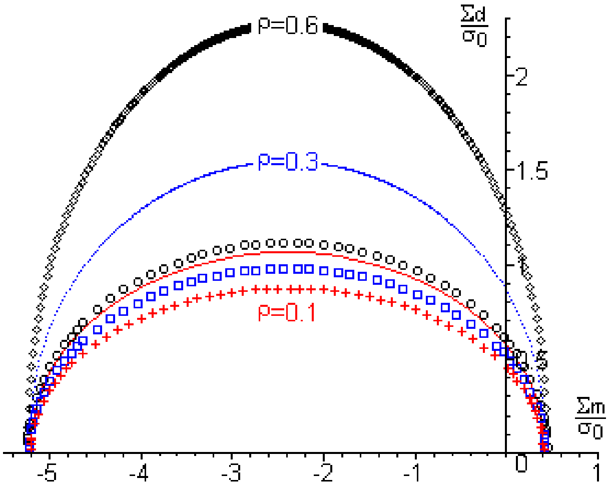

Figure 4.3: Comparison between the results predicted by limit analysis and the variational approach for different volume fractions of the rigid inclusion

-'line': limit analysis with $\rho = 0.1$, -'cross': variational approach with $\rho = 0.1$,

-'point': limit analysis with $\rho = 0.3$, -'box': variational approach with $\rho = 0.3$,

-'diamond': limit analysis with $\rho = 0.6$, -'circle': variational approach with $\rho = 0.6$

4.6 Strength under isotropic loading

4.6.1 Comparison between our results and the variational estimates of strength under isotropic loading

For the criterion developed by the kinematic approach of limit analysis in this paper, the strength under isotropic compression and traction is obtained numerically as indicated in section 4.4 with the plastic flow direction $\frac{D_d}{D_m} = 0$. In turn, for the criterion obtained by the variational method in [Shen,11] (see equations (4.54) with (4.55) in the present paper), the strength under isotropic compression is estimated by

$$\Sigma_m^{var-} = \frac{\left(-2T\sqrt{3+2f} - \sqrt{6f\left[(3f-2T^2)\rho + 3 + 2f\right]}\right)(1-f)Th}{\sqrt{3+2f}(3f-2T^2)} \tag{4.56}$$

while the strength under isotropic traction is estimated by

$$\Sigma_m^{var+} = \frac{\left(-2T\sqrt{3+2f} + \sqrt{6f\left[(3f-2T^2)\rho + 3 + 2f\right]}\right)(1-f)Th}{\sqrt{3+2f}(3f-2T^2)} \tag{4.57}$$

Figures 4.4 and 4.5 present the strength in isotropic compression for $\rho = 0.1$ and $\rho = 0.9$ respectively. The strength in isotropic traction is plotted at figures 4.6 and 4.7. In order to provide an insight into the effect of the parameter ρ, we compare the strength of the composite sphere as estimated by the two homogenization methods to that of the pure matrix ($\rho = 0$) (given by (4.69) in compression and (4.70) in traction, as will be shown in section 4.6.2). From these figures, it can be concluded that

> the results obtained by the kinematic method of limit analysis (Gurson approach) are in perfect agreement with those obtained by the variational method.
>
> At low volume fraction of the rigid core ($\rho = 0.1$), the three curves of figure 4.4 and figure4.6 are almost not differentiated from one another.
>
> At large volume fraction of the rigid core ($\rho = 0.9$), figures 4.5 and 4.7 reveal a small difference between the results of the reinforced material and the reference curve $\rho = 0$.

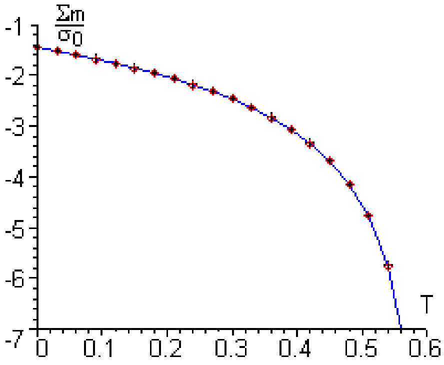

Figure 4.4: Strength in isotropic compression for $\rho = 0.1$ with reference curve $\rho = 0$ -'line':limit analysis, -'diamond':variational method, -'cross':reference curve

More precisely, selecting $f = 0.25$ and $T = 0.525$, figures 4.11 and 4.12 respectively present the variation of Σ_m^- and Σ_m^+ as functions of ρ (discrete points) together with analytical approximations introduced at section 4.6.4. This confirms the fact that the presence of a rigid core only slightly affects the isotropic strength.

4.6.2 Static approach of the limit analysis problem

The theory of limit analysis teaches that a kinematic approach like the Gurson one provides an upper bound of the true strength. In order to check the accuracy of a kinematic estimate, it is therefore highly desirable to derive a static approach which in turn will deliver a lower bound of the true strength.

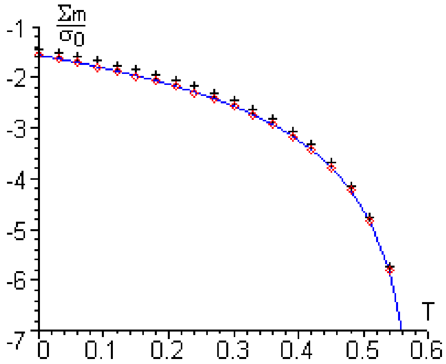

Figure 4.5: Strength in isotropic compression for $\rho = 0.9$ with reference curve $\rho = 0$

-'line':limit analysis, -'diamond':variational method, -'cross':reference curve

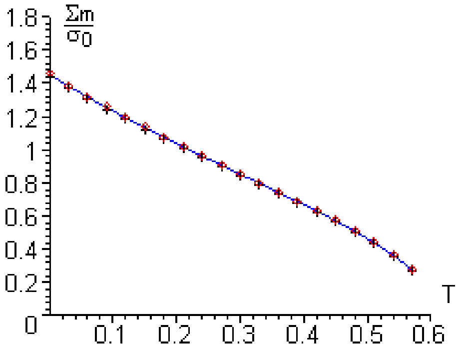

Figure 4.6: Strength in isotropic traction for $\rho = 0.1$ with reference curve $\rho = 0$

-'line':limit analysis, -'diamond':variational method, -'cross':reference curve

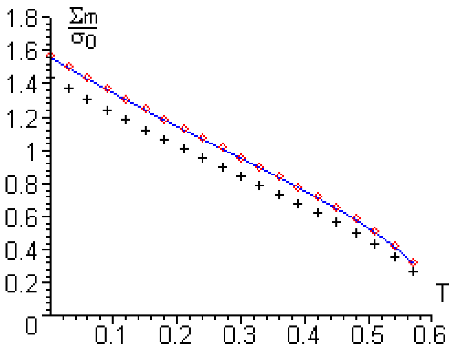

Figure 4.7: Strength in isotropic traction for $\rho = 0.9$ with reference curve $\rho = 0$

-'line':limit analysis, -'diamond':variational method, -'cross':reference curve

We therefore seek the stress field solution to an isotropic loading (traction or compression) in the framework of the 'rigid core sphere model'. The macroscopic stress state is of the form $\Sigma_m \mathbf{1}$. Accordingly the external boundary ($r = r_e$) is subjected to a radial surface force $\boldsymbol{\sigma} \cdot \underline{n} = \Sigma_m \underline{n}$. We implement the so-called static approach of limit analysis. It consists in deriving a mesoscopic stress field $\boldsymbol{\sigma}$ which must be statically admissible with these boundary conditions and meet the criterion $F^{meso}(\boldsymbol{\sigma}) = 0$ (see (4.2)). Owing to the spherical symmetry, this statically admissible stress field can be sought in the form (spherical coordinates):

$$\boldsymbol{\sigma} = \sigma_{rr}(r)\underline{e}_r \otimes \underline{e}_r + \sigma_{\theta\theta}(r)\left(\underline{e}_\theta \otimes \underline{e}_\theta + \underline{e}_\phi \otimes \underline{e}_\phi\right) \tag{4.58}$$

The boundary condition on the surface $r = r_e$ reads

$$\sigma_{rr}(r_e) = \Sigma_m \tag{4.59}$$

The momentum balance equation div$\boldsymbol{\sigma} = 0$ reduces to

$$\frac{d\sigma_{rr}}{dr} = 2\frac{\sigma_{\theta\theta} - \sigma_{rr}}{r} \tag{4.60}$$

With the notation $X = \sigma_{\theta\theta} - \sigma_{rr}$(note that $X^2 = \frac{3}{2}\sigma_d^2$), it is found that $\sigma_m = \sigma_{rr} - \frac{2}{3}X$, so that the criterion (4.2) yields

$$\frac{2}{3}\frac{\left(1 + \frac{2}{3}f\right)X^2}{T^2} + \frac{3f - 2T^2}{2T^2}\left(\sigma_{rr} + \frac{2}{3}X\right)^2 + 2(1-f)h\left(\sigma_{rr} + \frac{2}{3}X\right) - (1-f)^2h^2 = 0 \tag{4.61}$$

The values of X solutions of (4.61) read:

$$X = \frac{3}{2}\frac{(3f - 2T^2)\sigma_{rr} - 2hT^2(f-1) \pm \sqrt{\Delta}}{2T^2 - 5f - 3}, \quad \text{with} \tag{4.62}$$

$$\Delta = (2f+3)(2T^2 - 3f)\sigma_{rr}^2 + 4hT^2(2f+3)(f-1)\sigma_{rr} + 2h^2T^2(5f+3)(f-1)^2 \tag{4.63}$$

Recalling (4.60), an ordinary differential equation with respect to σ_{rr} is obtained in the form:

$$X(\sigma_{rr}) = \frac{r}{2}\frac{d\sigma_{rr}}{dr} \tag{4.64}$$

Introducing (4.62) into (4.64) and integrating over the interval $[r_i, r_e]$, one obtains

$$\frac{1}{3}\ln(\rho) = \int_c^{\Sigma_m} \frac{1}{3}\frac{2T^2 - 5f - 3}{(2T^2 - 3f)\sigma_{rr} + 2hT^2(f-1) + \epsilon\sqrt{\Delta}} d\sigma_{rr} \tag{4.65}$$

where the notation $c = \sigma_{rr}(r_a)$ and the boundary condition (4.59) at $r = r_e$ have been used. Note that no boundary condition is available at $r = r_i$. The physical meaning of (4.65) is the following: Whenever there exists a constant c such that (4.65) is fulfilled (with $\epsilon = +1$

or -1), then Σ_m is an admissible loading for the value of ρ at stake. We seek the highest possible value $\Sigma_m^+ > 0$ of Σ_m (isotropic strength in traction) and the lowest one, denoted by $\Sigma_m^- < 0$ (isotropic strength on compression).

For the simplification of the following discussion, the denominator in the integral of (4.65) is denoted by $\mathcal{D}_\epsilon$:

$$\mathcal{D}_\epsilon = (2T^2 - 3f)\sigma_{rr} + 2hT^2(f-1) + \epsilon\sqrt{\Delta} \tag{4.66}$$

In order for this integral to be defined, two mathematical conditions are to be met, namely $\Delta \geq 0$ and $\mathcal{D}_\epsilon \neq 0$. This remark leads to introduce the solutions to the equations of $\Delta = 0$ and of $D_\epsilon = 0$.

First, let $\Sigma_{1m}^\pm$ denote the solutions to $\Delta = 0$, which read:

$$\begin{aligned} \Sigma_{1m}^+ &= \frac{\left[2T\left(3+2f\right) - \sqrt{6f\left(3+2f\right)\left(5f-2T^2+3\right)}\right](1-f)hT}{(3+2f)(2T^2-3f)} \\ \Sigma_{1m}^- &= \frac{\left[2T\left(3+2f\right) + \sqrt{6f\left(3+2f\right)\left(5f-2T^2+3\right)}\right](1-f)hT}{(3+2f)(2T^2-3f)} \end{aligned} \tag{4.67}$$

Recalling that $2T^2 - 3f < 0$, we note that the condition $\Delta \geq 0$ implies that c and $\Sigma_m \in \left[\Sigma_{1m}^-, \Sigma_{1m}^+\right]$. An immediate consequence is that the bounds $\Sigma_m^\pm$ are subjected to

$$\Sigma_{1m}^- \leq \Sigma_m^-(\rho) \leq \Sigma_m^+(\rho) \leq \Sigma_{1m}^+ \tag{4.68}$$

In turn, let Σ_{2m}^+ (resp. Σ_{2m}^-) denote the solution to $D_+ = 0$ (resp. $D_- = 0$):

$$\Sigma_{2m}^- = \frac{\left(2T + \sqrt{6}\sqrt{f}\right)(f-1)Th}{3f - 2T^2} \tag{4.69}$$

$$\Sigma_{2m}^+ = \frac{\left(2T - \sqrt{6}\sqrt{f}\right)(f-1)Th}{3f - 2T^2} \tag{4.70}$$

The condition $D_\epsilon \neq 0$ on the interval of integration $[c, \Sigma_m]$ requires one of the 3 following conditions to be satisfied:

$$\begin{aligned} &\text{case 1}: \quad c,\ \Sigma_m \leq \Sigma_{2m}^- \\ &\text{case 2}: \quad \Sigma_{2m}^- \leq c,\ \Sigma_m \leq \Sigma_{2m}^+; \\ &\text{case 3}: \quad c,\ \Sigma_m \geq \Sigma_{2m}^+ \end{aligned} \tag{4.71}$$

Considering (4.61) or (4.62) with $X = 0$, it appears that Σ_{2m}^- and Σ_{2m}^+ can be interpreted as the isotropic strength, respectively in compression and traction, of the matrix surrounding the core. Observing that the strength of the composite sphere is necessarily higher than that of the matrix, an immediate consequence of the physical meaning of $\Sigma_{2m}^{\pm}$ is that the bounds $\Sigma_m^{\pm}$ satisfy:

$$\Sigma_m^-(\rho) \leq \Sigma_{2m}^- \quad ; \quad \Sigma_{2m}^+ \leq \Sigma_m^+(\rho) \tag{4.72}$$

The combination of (4.68) and (4.72) reveals that:

$$\Sigma_m^-(\rho) \in \left[\Sigma_{1m}^-, \Sigma_{2m}^-\right] \quad ; \quad \Sigma_m^+(\rho) \in \left[\Sigma_{2m}^+, \Sigma_{1m}^+\right] \tag{4.73}$$

Accordingly, only cases 1 and 3 in (4.71) have to be considered. The intervals of (4.73) are depicted at figure 4.8.

Let us now come back to (4.65) (remember that $2T^2 - 5f - 3 \leq 0$). We start with $\epsilon = +1$ and the case 3 of (4.71). For the integral to be defined and negative, we must have:

$$\Sigma_{2m}^+ \leq \Sigma_m \leq c \leq \Sigma_{1m}^+ \qquad (D_+ < 0)$$

For a given value of ρ, the greatest value of Σ_m, that is $\Sigma_m^+(\rho)$, is the solution to (4.65) with $c = \Sigma_{1m}^+$:

$$\frac{1}{3}\ln(\rho) = \int_{\Sigma_{1m}^+}^{\Sigma_m^+} \frac{1}{3}\frac{2T^2 - 5f - 3}{(2T^2 - 3f)\sigma_{rr} + 2hT^2(f-1) + \sqrt{\Delta}} d\sigma_{rr} \tag{4.74}$$

Similarly, consider $\epsilon = -1$ in (4.65) with case 1 in (4.71). For the integral to be defined and negative, it is necessary that

$$\Sigma_{1m}^- \leq c \leq \Sigma_m \leq \Sigma_{2m}^- \qquad (D_- > 0)$$

Again, for a given value of ρ, the lowest value of Σ_m, that is $\Sigma_m^-(\rho)$, is the solution of (4.65) with $c = \Sigma_{1m}^-$:

$$\frac{1}{3}\ln(\rho) = \int_{\Sigma_{1m}^-}^{\Sigma_m^-} \frac{1}{3}\frac{2T^2 - 5f - 3}{(2T^2 - 3f)\sigma_{rr} + 2hT^2(f-1) - \sqrt{\Delta}} d\sigma_{rr} \tag{4.75}$$

(4.74) and (4.75) allow to determine the sought values $\Sigma_m^{\pm}(\rho)$. In practice, it is easier to use these equations for the numerical determination of the inverse functions $\rho(\Sigma_m^{\pm})$.

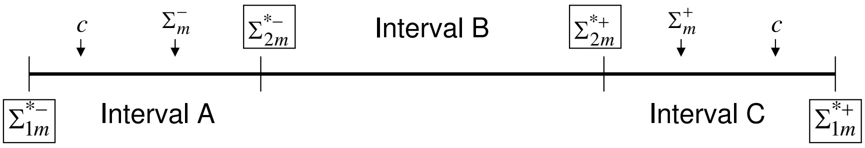

Figure 4.8: Intervals of integration

4.6.3 Comparisation between static and kinematic solutions

Figures 4.9 and 4.10 present the comparison between the static solution (solid curve) and the kinematic solution (points) as functions of the rigid core volume fraction ρ ($f = 0.25$, $T = 0.525$). Since the two plotted solutions can hardly be differentiated, it can be concluded that they can be regarded as the exact strength of the composite material, within the rigid core model. This comes in addition to the previous observation that the Gurson model and the variational method yield seemingly identical results in isotropic loadings (section 4.6.1).

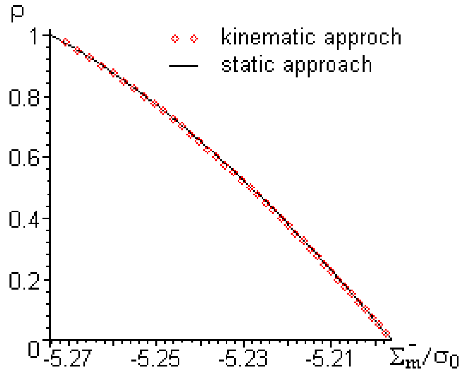

Figure 4.9: Static and kinematic bounds in isotropic compression

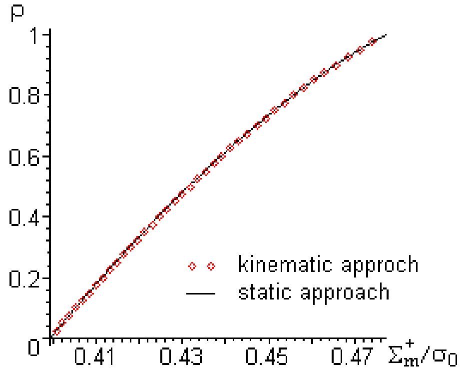

Figure 4.10: Static and kinematic bounds in isotropic traction

4.6.4 Analytical expressions of the strength under isotropic loading

Due to the complexity of the integrals in (4.74) and (4.75), these equations can hardly be solved analytically. However, we observe that $\Sigma_m^{\pm}$ remain in the neighborhood of $\Sigma_{2m}^{\pm}$. We therefore propose to approximate the functions $\mathcal{D}_+$ and $\mathcal{D}_-$ by series expansions in the neigborhood of Σ_{2m}^{+} and Σ_{2m}^{-} respectively. These series expansions read:

In the case of series expansion to first order,

$$\mathcal{D}_{-}(\sigma_{rr}) = (2T^2 - 5f - 3)(\sigma_{rr} - \Sigma_{2m}^{-}) + \mathcal{O}\left[(\sigma_{rr} - \Sigma_{2m}^{-})^2\right] \tag{4.76}$$

$$\mathcal{D}_{+}(\sigma_{rr}) = (2T^2 - 5f - 3)(\sigma_{rr} - \Sigma_{2m}^{+}) + \mathcal{O}\left[(\sigma_{rr} - \Sigma_{2m}^{+})^2\right] \tag{4.77}$$

We then substitute $\mathcal{D}_{\epsilon}$ in (4.65) by the above expressions (4.76) and (4.77) for the compressive and tensile strength respectively. Under compression, the analytical solution of (4.74) reads,

$$\Sigma_m^{-} = \rho\Sigma_{1m}^{-} + (1-\rho)\Sigma_{2m}^{-} \tag{4.78}$$

Under traction, the analytical solution reads,

$$\Sigma_m^{+} = \rho\Sigma_{1m}^{+} + (1-\rho)\Sigma_{2m}^{+} \tag{4.79}$$

The comparisons between the results predicted by the analytical expression and by the numerical integration are plotted in figures 4.11 and 4.12.

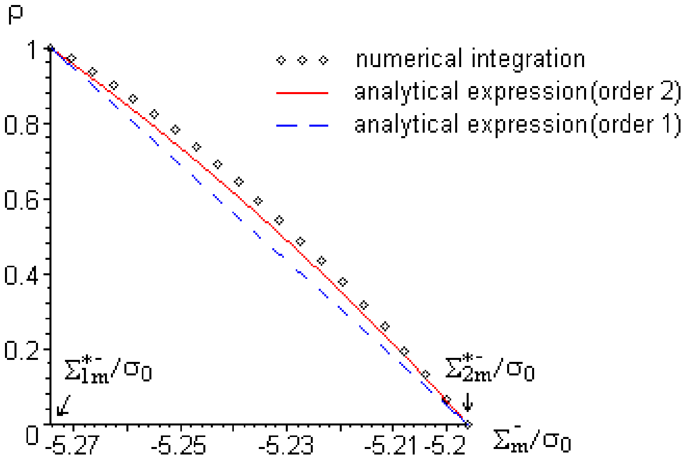

Figure 4.11: Strength in isotropic compression Σ_m^{-}/σ_0 as a function of ρ ($f = 0.25$, $T = 0.525$). Numerical integration and first and second order approximations.

In the case of of series expansion to the second order,

$$\mathcal{D}_{-}(\sigma_{rr}) = (2T^2 - 5f - 3)(\sigma_{rr} - \Sigma_{2m}^{-}) + B^{-}(\sigma_{rr} - \Sigma_{2m}^{-})^2 + \mathcal{O}\left[(\sigma_{rr} - \Sigma_{2m}^{-})^3\right] \tag{4.80}$$

$$\mathcal{D}_{+}(\sigma_{rr}) = (2T^2 - 5f - 3)(\sigma_{rr} - \Sigma_{2m}^{+}) + B^{+}(\sigma_{rr} - \Sigma_{2m}^{+})^2 + \mathcal{O}\left[(\sigma_{rr} - \Sigma_{2m}^{+})^3\right] \tag{4.81}$$

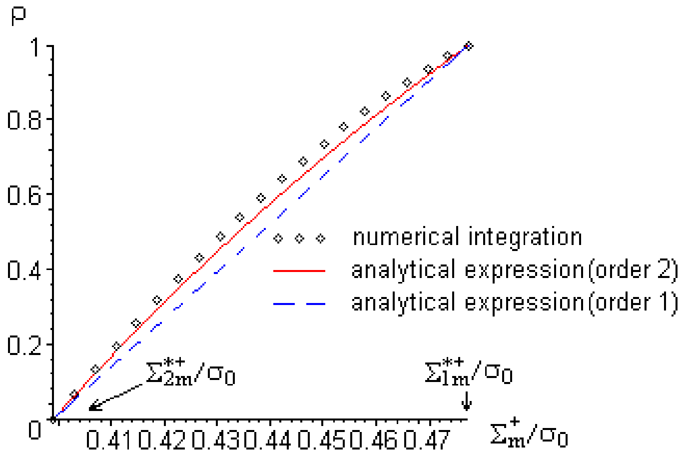

Figure 4.12: Strength in isotropic traction Σ^+_m/σ_0 as a function of ρ ($f = 0.25$, $T = 0.525$). Numerical integration and first and second order approximations.

We then substitute $\mathcal{D}_\epsilon$ in (4.65) by the above expressions (4.80) and (4.81). The analytical solutions at order 2 read:

$$\Sigma^{\pm}_m = \eta + \rho \frac{c-\eta}{\kappa(c-\eta)(1-\rho)+1} \tag{4.82}$$

with the following parameters:

isotropic compression:

$$\begin{cases} \eta = \Sigma^-_{2m} \\ \kappa = \frac{1}{2\sqrt{6}} \frac{3+2f}{(f-1)\sqrt{fhT}} \\ c = \Sigma^-_{1m} \end{cases} \tag{4.83}$$

isotropic traction:

$$\begin{cases} \eta = \Sigma^+_{2m} \\ \kappa = \frac{1}{2\sqrt{6}} \frac{3+2f}{(1-f)\sqrt{fhT}} \\ c = \Sigma^+_{1m} \end{cases} \tag{4.84}$$

The results predicted by this new analytical expression are also plotted in figure 4.11 and 4.12.

4.7 An approximate analytical macroscopic criterion

We seek an approximation of the criterion by an ellipse in the (Σ_m, Σ_d) plane. The ellipse intersects the Σ_m-axis at the points $(\Sigma^-_m, 0)$ and $(\Sigma^+_m, 0)$. The center of the ellipse is located at the middle of these points. We still have to determine the ordinate of the center of the ellipse which corresponds to the strength under pure shear ($D_m = 0$).

4.7.1 Strength under pure shear loading ($D_m = 0$)

With the condition $D_m = 0$, it is readily seen that the value of the parameter A which minimizes $\tilde{\Pi}(\mathbf{D}, A)$ is $A = 0$ (see (4.45)). Accordingly, specifying equations (4.47)-(4.53) with (4.30) and (4.40) for $D_m = 0$ and $A = 0$, closed-form expressions of the mean stress and the maximum shear stress can be obtained from (4.46):

$$\Sigma_{m,c} = -\lambda \tag{4.85}$$

$$\Sigma_{d,c} = \sigma_0 \left[\sqrt{\frac{2}{3}}(1-\rho) + \sqrt{\frac{17\alpha + 4}{15\alpha}}\rho \right] \tag{4.86}$$

where λ, σ_0 and α have been defined in (4.12) and (4.13). The subscript c recalls that this point is the center of the ellipse.
(4.86) then reads:

$$\Sigma_{d,c} = \sqrt{\frac{2}{3}}\sigma_0 \left[1 - \left(1 - \frac{1}{\sqrt{10}} \sqrt{\frac{67f - 34T^2 + 24}{3f - 2T^2}} \right) \rho \right] \tag{4.87}$$

Then, according to the criterion (4.54) together with (4.55) predicted by the variational method in [Shen,11], the maximum shear stress and the corresponding mean stress read

$$\Sigma_{m,c}^{var} = -\lambda \tag{4.88}$$

$$\Sigma_{d,c}^{var} = \sqrt{\frac{2}{3}}\sigma_0 \sqrt{1 + \frac{-4T^2 + 12f + 9}{-6T^2 + 13f + 6}\rho} \tag{4.89}$$

Comparing (4.87) and (4.89), it can be seen that the maximum shear stress predicted from (4.87) by the rigid core model is more significantly affected by the fraction volume ρ of the rigid inclusion than the one obtained from the variational method.

4.7.2 Elliptic approximate macroscopic criterion

Now let us try to approximate the criterion given in parametric form (obtained by means of kinematic approach) found in section 4.4 by an analytical elliptic criterion. Analytical expressions of the strength have been established at particular stress states, namely under isotropic loading (section 4.6.2) and under pure shear loading (with $\Sigma_m = -\lambda$, section 4.7.1). Recalling (4.82) (4.83) and (4.84) for the expressions of Σ_m^+, Σ_m^- in the case of a second order expansion, together with (4.87) for the expression of $\Sigma_{d,c}$, the macroscopic criterion can be approached by the following analytical elliptic function:

$$\left(\frac{\Sigma_m-\lambda}{\Sigma_L/2}\right)^2+\left(\frac{\Sigma_d}{\Sigma_{d,c}}\right)^2=1 \tag{4.90}$$

with $\Sigma_L=\Sigma_m^+-\Sigma_m^-$ and $\lambda=(\Sigma_m^++\Sigma_m^-)/2$. Recall that Σ_m^+, Σ_m^-, $\Sigma_{d,c}$ are quantified in (4.82),(4.87) by (4.67),(4.69),(4.70); and λ, σ_0, α are given in (4.12),(4.13).

Note that when the particles volume fraction $\rho=0$, (4.90) allows to retrieve the strength criterion (4.2) of the porous matrix with Drucker-Prager solid phase, here in the form:

$$\left(\frac{\Sigma_m-\lambda}{\Sigma_L^{\rho=0}/2}\right)^2+\left(\frac{\Sigma_d}{\Sigma_{d,c}^{\rho=0}}\right)^2=1 \tag{4.91}$$

with

$$\Sigma_L^{\rho=0}=\frac{2\sqrt{6}\sqrt{f}(1-f)Th}{3f-2T^2}\quad ;\quad \Sigma_{d,c}^{\rho=0}=\sqrt{\frac{2}{3}}\sigma_0 \tag{4.92}$$

and $\lambda=(1-f)h\frac{2T^2}{3f-2T^2}$ introduced in (4.12).

We present at figures Fig.4.13 and Fig.4.14 the comparison between the predictions of the analytical macroscopic criterion, (4.90), and that numerically obtained from the parametric equations, (4.46), together with the condition of minimization (4.45). The following values of parameters have been considered: $\rho=0.3$ and $\rho=0.6$ respectively ($f=0.25$, $h=30$, $T=0.525$). This comparison shows an excellent accuracy of (4.90).

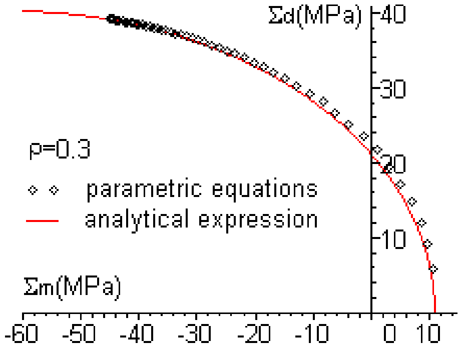

Figure 4.13: Comparison between the results of parametric equations and analytical criterion, with the parameters as $\rho=0.3$, $f=0.25$, $T=0.525$, $h=30$

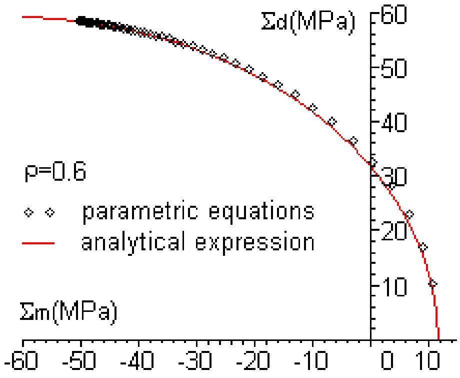

Figure 4.14: Comparison between the results of parametric equations and analytical criterion, with the parameters as $\rho = 0.6$, $f = 0.25$, $T = 0.525$, $h = 30$

4.8 Conclusion

On the basis of a limit analysis approach, we have proposed an extension of available models (devoted to the macroscopic strength of porous media). This extension concern porous materials with a Drucker-Prager solid phase, reinforced by rigid particles. The proposed model concerns in particular the Callovo Oxfordian clay as a composite material made up of rigid inclusions embedded in a porous clay matrix. The pores are assumed to be very small as compared to the rigid inclusions. This scale separation justifies to implement a two steps homogenization procedure, in which the first (dealing with the porous clay matrix, transition from micro to mesoscale) takes advantage of results by Maghous et al. (2009). The present paper has focused on the second step of the homogenization (transition meso-macro) by developing a limit analysis based kinematic approach of a spherical 'rigid core'. This delivers an upper bound of the macroscopic strength criterion of the microporous composite which has been determined by parametric equations and then in the form of an approximate closed-form criterion whose accuracy has been demonstrated. The latter has been compared to the estimate of the strength recently derived by [Shen,11] (see equations (4.54) with (4.55) in the present paper) on the basis of a variational non linear homogenization approach. A very good agreement between the two models is obtained for isotropic stress states. In contrast, a significant discrepancy between the failure envelopes is observed on the shear strength for large values of the rigid inclusions concentration. Moreover, the good accuracy of the estimate of the strength under isotropic loadings has been shown by a comparison with the results of a static (stress-based) approach of the limit analysis problem. An interesting observation is that the estimates of the isotropic strength in traction or in compression do not depend on the homogenization method (limit analysis, variational method). Furthermore, the isotropic strength proves to be only slightly affected by the rigid core volume fraction. The practical implication is that the isotropic strength properties of the clay matrix and of the Callovo Oxfordian argillite are very close, irrespective of the quartz/calcite content. Finally, we examine in Appendix the particular case of a von Mises solid phase of the porous matrix for which our results are compared to the estimates established by [Shen,11] and [Garajeu and Suquet,97].

Acknowledgements

The work presented in this paper was partly funded by ANDRA, the French national Agency for the management of radioactive wastes, which is gratefully acknowledged.

4.9 Appendix A: Reinforced porous materials with Von-Mises solid phase

We aim here at analyzing on the basis of the proposed model, the strength properties of the reinforced porous material in which the solid phase obeys now to a von Mises criterion:

$$f^s(\tilde{\boldsymbol{\sigma}}) = \tilde{\sigma}_{eq} - \sigma_0^{vm} \quad \text{with} \quad \tilde{\sigma}_{eq} = \sqrt{\frac{3}{2}\tilde{\boldsymbol{\sigma}}_d : \tilde{\boldsymbol{\sigma}}_d} \tag{4.93}$$

σ_0^{vm} is the yield stress of the solid phase. In fact, the von Mises criterion (4.93) is a limit case of the Drucker-Prager criterion (4.1) for:

$$h = \sqrt{\frac{2}{3}}\frac{\sigma_0^{vm}}{T}, \quad \text{and} \quad T \to 0 \tag{4.94}$$

4.9.1 Comparison with the result of [Shen11thesis] in the limit case of von Mises solid phase

As mentioned before, by considering a modified secant moduli approach (equivalent to a variational approach) in the two homogenization steps, [Shen,11] derived the strength criterion of reinforced porous materials having a Drucker-Prager solid phase in the form given by (4.54). The restriction of this result for the material having a von Mises solid phase is readily retrieved here by taking into account (4.94) into (4.54):

$$\frac{3}{2}\frac{1+\frac{2}{3}f+f\rho}{\frac{12f+9}{13f+6}\rho+1}\left(\frac{\Sigma_d}{\sigma_0^{vm}}\right)^2 + \frac{9}{4}f\left(\frac{\Sigma_m}{\sigma_0^{vm}}\right)^2 - \frac{3+2f+3\rho f}{3+2f}(1-f)^2 = 0 \tag{4.95}$$

In the first homogenization step of [Shen,11], the behavior of the microporous medium has been described by the elliptic criterion (4.2) proposed in [Maghous et al.,09]. For the microporous medium having a von Mises solid phase, this criterion reduces to the criterion already proposed by [PonteCastaneda,91]:

$$(\frac{3}{2}+f)\left(\frac{\sigma_d}{\sigma_0^{vm}}\right)^2+\frac{9}{4}f\left(\frac{\sigma_m}{\sigma_0^{vm}}\right)^2-(1-f)^2\leq 0 \tag{4.96}$$

which can be recast in the form (4.3) with the appropriate parameters. The resulting support function $\pi'_{\mathcal{F}}(\mathbf{d})$ derived from (4.9) reads:

$$\pi'_{\mathcal{F}}(\mathbf{d})=2k'\sqrt{\frac{L'^2}{4}d_v^2+\frac{1}{2}d_d^2}=\sigma'_0\sqrt{\frac{1}{3\alpha'}d_v^2+d_d^2} \tag{4.97}$$

with

$$\sigma'_c=0 \quad ; \quad L'^2=\frac{4(3+2f)}{9f} \quad ; \quad k'^2=\frac{(1-f)^2\sigma_0^{vm2}}{3+2f} \tag{4.98}$$

and

$$\sigma'_0=(1-f)\sigma_0^{vm}\sqrt{\frac{3}{3+2f}} \quad ; \quad \alpha'=\frac{3f}{2(3+2f)} \tag{4.99}$$

Hence, by considering the new parameters σ'_0,α' introduced in (4.99), numerical results of the macroscopic parametric criterion can be obtained following the procedure described in section 4.4.

Let us now approximate the macroscopic criterion by an analytical elliptic function as done in section 4.7.2. Applying the series expansion up to the second-order approximation (see section 4.6.4) in the von Mises limit case, leads to:

$$\left(\frac{\Sigma_m}{\Sigma'_L/2}\right)^2+\left(\frac{\Sigma_d^2}{\Sigma'_{d,c}}\right)^2=1 \tag{4.100}$$

By considering (4.94), the limits of (4.82) and (4.84) yield the expression of Σ'_L as:

$$\Sigma'_L=2\eta'+2\rho\frac{c-\eta'}{\kappa'(c-\eta')(1-\rho)+1} \tag{4.101}$$

where the parameters η',κ' and c' are given by:

$$\eta'=\frac{2\sigma_0^{vm}(1-f)}{3\sqrt{f}}; \quad \kappa'=\frac{3+2f}{4\sigma_0^{vm}(1-f)\sqrt{f}}; \quad c'=\frac{2\sigma_0^{vm}}{3}\frac{(1-f)\sqrt{5f+3}}{\sqrt{f(3+2f)}} \tag{4.102}$$

Introducing respectively σ'_0, α' (defined in (4.99)) at the places of σ_0,α in (4.86), $\Sigma'_{d,c}$ which enters in (4.100) reads:

$$\Sigma'_{d,c}=(1-f)\sigma_0^{vm}\sqrt{\frac{1}{3+2f}}\left(\sqrt{2}(1-\rho)+\rho\sqrt{\frac{67f+24}{15f}}\right) \tag{4.103}$$

Remark: *Before comparing the results of the two approaches, it is convenient to emphasize that When* $f = 0$*, the predicted strengths under shear loading and hydrostatic pressure by* (4.100) *tend to* ∞*. The main reason of such result lies in the conditions under which is performed the present limit analysis. Indeed, the consideration of the Gurson type extended velocity field to a compressible matrix was justified by the fact that no special precautions had to be taken at the inclusion-matrix interface on the velocity discontinuity, due to the elliptic character of the yield function of the porous matrix. In this case, the contribution of the interface to the dissipation is necessarily bounded. Conversely, when* f *tends to* 0 *the criterion of the matrix reduces to a von Mises one for which the condition of a purely tangential discontinuity must be fulfilled; this is not ensured by the Gurson type velocity field considered in the present study.*

The comparison between the criterion expressed by the parametric equations and the analytical criterion (4.100) is provided in Fig.4.15. As before for the general case of Drucker-Prager solid phase, a good agreement is again noted in the present case.

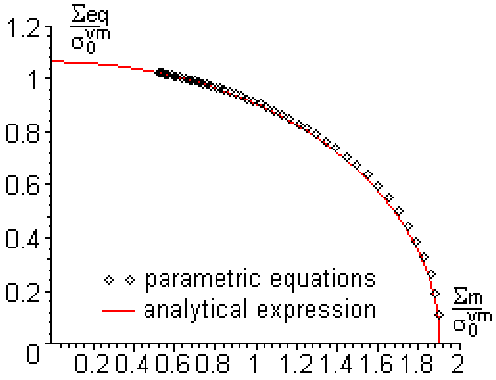

Figure 4.15: Comparison between the results of parametric equations and analytical criterion, with the parameters as $\rho = 0.1$, $f = 0.1$, $\sigma_0^{vm} = 1$

The comparison between our results (4.100) and that predicted by the variational approach (see equation (4.95))[2] is shown in Fig.4.16. The difference between the two predictions is noticeable for low stress triaxiality where the modified secant moduli approach leads to a less strengthened composite.

---

[2] *Note that the two approaches differ only in the second step of homogenization.*

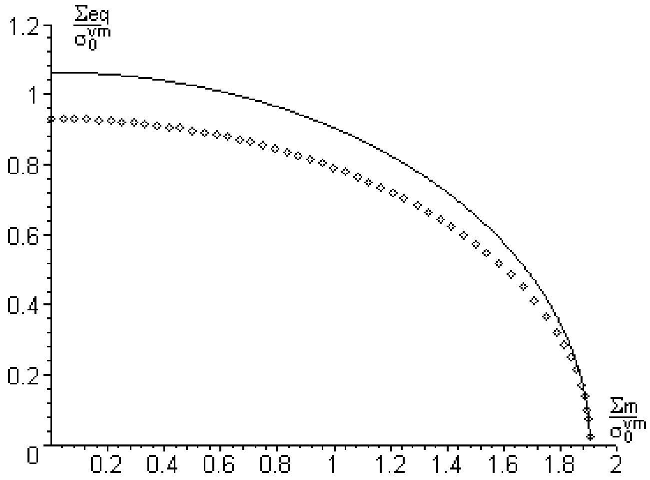

Figure 4.16: Comparison between our results (4.100) and that predicted by the variational approach, with the parameters as $f = 0.1$, $\rho = 0.1$, $\sigma_0^{vm} = 1$

-'line': criterion (4.100) considering the porous matrix described by the criterion in [PonteCastaneda,91],

-'box': criterion (4.95) obtained in the von Mises case via (4.54) proposed by [Shen,11]

4.9.2 Comparison with the results of [GarajeuSuquet97]

The strength criterion of reinforced porous materials having a von Mises solid phase, has also been investigated in [Garajeu and Suquet,97]. These authors used a Gurson model [Gurson,77] in the first homogenization step, then a variational approach in the second homogenization step[3]. Their criterion established in [Garajeu and Suquet,97] reads:

$$\begin{aligned} & S_{eq}^2 + f\cosh(S_m)\left(1 + \sqrt{1 + (1+f^2)\rho - S_{eq}^2\rho + f^2\rho}\right) - 1 - f^2 + \rho f^2 = 0 \\ & S_{eq} = \frac{\sqrt{3}\Sigma_d}{\sqrt{2}\sigma_0^{vm}} \frac{1}{\sqrt{1+\rho}} \\ & S_m = \frac{3|\Sigma_m|}{2\sigma_0^{vm}} - \sqrt{2 + (1+f^2)\rho - S_{eq}^2\rho - 2\sqrt{1 + (1+f^2)\rho - S_{eq}^2\rho + f^2\rho}} \end{aligned} \tag{4.104}$$

In order to keep the comparison meaningful, we adopt for the microporous medium (in the first homogenization step) the modified elliptic criterion proposed by [Michel and Suquet,92] and which is known to be in agreement with the Gurson criterion. This criterion reads:

$$(\frac{3}{2} + f)\left(\frac{\sigma_d}{\sigma_0^{vm}}\right)^2 + \frac{9}{4}\left(\frac{1-f}{\ln(f)}\right)^2\left(\frac{\sigma_m}{\sigma_0^{vm}}\right)^2 - (1-f)^2 = 0 \tag{4.105}$$

---

[3] *Clearly enough, this differs from our approach in which the variational approach is first considered, followed by a limit analysis based one.*

which can be recast in the form (4.3) with the appropriate parameters. The resulting support function $\pi'_{\mathcal{F}}(\mathbf{d})$ derived from (4.9) reads:

$$\pi^*_{\mathcal{F}}(\mathbf{d}) = 2k^*\sqrt{\frac{L^{*2}}{4}d_v^2 + \frac{1}{2}d_d^2} = \sigma_0^*\sqrt{\frac{1}{3\alpha^*}d_v^2 + d_d^2} \tag{4.106}$$

with

$$\sigma_c^* = 0 \quad ; \quad L^{*2} = \frac{4(3+2f)\ln(f)^2}{9(1-f)^2} \quad ; \quad k^{*2} = \frac{(1-f)^2\sigma_0^{vm2}}{3+2f} \tag{4.107}$$

and

$$\sigma_0^* = (1-f)\sigma_0^{vm}\sqrt{\frac{3}{3+2f}} \quad ; \quad \alpha^* = \frac{3(1-f)^2}{2(3+2f)\ln(f)^2} \tag{4.108}$$

As previously done in section 4.9.1, by adopting the new parameters α^*, σ_0^* of (4.108), numerical results of the macroscopic parametric criterion can be obtained by applying the procedure described in section 4.4.

Let us now approximate the macroscopic criterion by an analytical elliptic function as done in section 4.7.2. By performing the series expansion up to the second-order approximation (see section 4.6.4), the macroscopic elliptic criterion for the von Mises limit case reads:

$$\left(\frac{\Sigma_m}{\Sigma_L^*/2}\right)^2 + \left(\frac{\Sigma_d^2}{\Sigma_{d,c}^*}\right)^2 = 1 \tag{4.109}$$

with Σ_L^*, $\Sigma_{d,c}^*$ given by:

$$\Sigma_L^* = \frac{4\sigma_0^{vm}}{3}\,\frac{\eta^* c^* + \kappa^*}{\chi^* c^* + \omega^*} \tag{4.110}$$

where

$$\begin{cases} \eta^* = -18\rho\,(1-f)^2 + 3\,(\rho-1)\,(2f+3)\ln(f)^2 \\ \kappa^* = 2(\rho-1)\ln(f)\left[(2f+3)\ln(f)^2 - 6(1-f)^2\right]\sigma_0^{vm} \\ \chi^* = 3\,(\rho-1)\,(2f+3)\ln(f) \\ \omega^* = 2\left[(\rho-1)\,(2f+3)\ln(f)^2 + 6\,(1-f)^2\right]\sigma_0^{vm} \\ c^* = \dfrac{2}{3}\sqrt{\dfrac{(2f+3)\ln(f)^2 + 3(1-f)^2}{3+2f}}\sigma_0^{vm} \end{cases} \tag{4.111}$$

By adopting respectively σ_0^*, α^* at the places of σ_0, α in (4.86), $\Sigma_{d,c}^*$ which enters in (4.109) reads:

$$\Sigma_{d,c}^* = \sigma_0^{vm}\sqrt{\frac{1}{3+2f}}\left[\frac{\sqrt{51(1-f)^2 + 8(3+2f)\ln(f)^2}}{\sqrt{15}}\rho + \sqrt{2}(1-f)(1-\rho)\right] \tag{4.112}$$

The comparison between the criterion expressed by the parametric equations and the analytical criterion is provided in Fig.4.17. As expected, a good agreement is again noted in the present case.

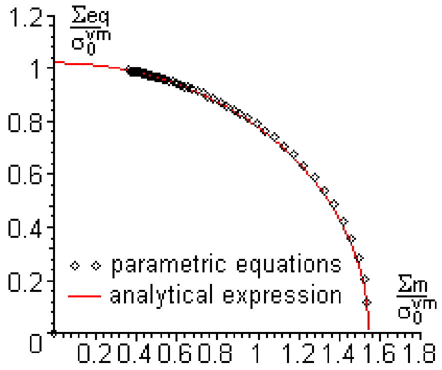

Figure 4.17: Comparison between the results of parametric equations and analytical criterion, with the parameters as $\rho = 0.1$, $f = 0.1$, $\sigma_0^{vm} = 1$

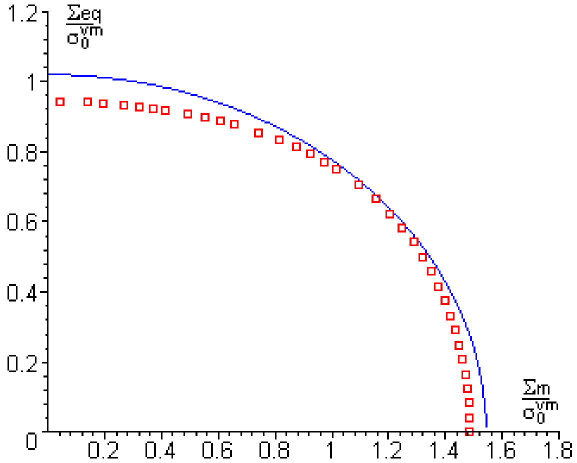

Figure 4.18: Comparison between the results predicted by the limit analysis and variational approach in the second step, with the parameters as $\rho = 0.1$, $f = 0.1$, $\sigma_0^{vm} = 1$

-'line': criterion (4.109) considering the porous matrix described by the criterion in [Michel and Suquet,92],

-'box': criterion (4.104) proposed by [Garajeu and Suquet,97]

In the case of the microporous matrix described by (4.105), the comparison between our results (see (4.109)) and that of the variational approach (4.104) is shown in Fig.4.18.

4.10 Appendix B: Comparison with the experimental data

To assess the accuracy of the proposed criterion, the numerical results are compared with the experimental data in this section. Experimental tests have been conducted on samples cored from the borehole EST 104 of the site, where the underground research laboratory for nuclear waste disposal is operated by ANDRA, at different depths ($451.4 - 466.8m$, $468.9 - 469.1m$ and $482.1 - 482.4m$). The strength data used in this study is extracted from the above test results (see also [Abou-Chakra et al.,08]) in the way that the strength is registered at the point of the stress-strain curve where the rupture occurs. The strength values of the COx argillite with respect to the volume fraction of the rigid inclusion ρ are resumed in Table 4.1.

Table 4.1: The strength values of the COx argillite with respect to the volume fraction of the rigid inclusion

ρ (%)	Σ_m(MPa)	Σ_d(MPa)	ρ (%)	Σ_m(MPa)	Σ_d(MPa)
40	8.6	22.1	49	11.6	28.7
40	19.3	35.3	51	18.0	32.0
40	24.0	34.45	53	25.0	36.9
45	25.3	37.7	56	19.6	36.1

The numerical simulations are now performed for uniaxial and triaxial compression tests at different confining pressures (0, 5 and 10MPa), and compared with the experimental data in Fig.4.19. We have to determinate 3 parameters of the proposed criterion. The parameters of $f = 0.25$ and $h = 30$ are retained as same as those in [Shen,11] to facilitate the confrontation of the two different methods. Recalling Fig.4.3, one can see that the difference between of the two failure envelopes becomes obvious with an increasing ρ. The volume fraction of the rigid inclusion ρ plays a very important role in predicting strength of COx argillite. This property revealed by the new proposed criterion are validated by the comparison illustrated in Fig.4.19, where the prediction of the criterion obtained by variational method obviously underestimates and experimental results.

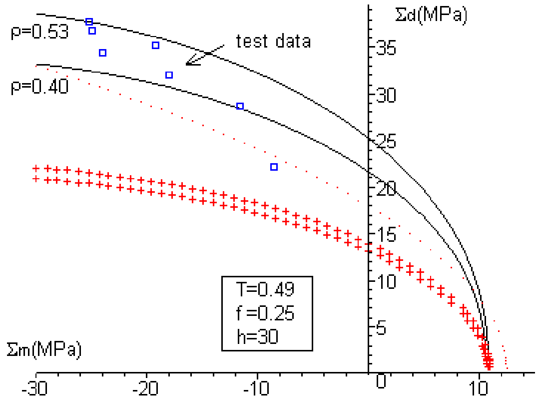

Figure 4.19: Comparisons of the numerical results obtained by limit analysis method $T = 0.49$(line) and by variational method $T = 0.49$(cross), with the experimental data (box) at different volume fraction ρ, for uniaxial tests

4.11 Appendix C: Integration

The following principe is applied in the derivation of the inequality of (4.28).

$$\int_a^b fg dx \leq \left(\int_a^b f^2 dx\right)^{\frac{1}{2}} \left(\int_a^b g^2 dx\right)^{\frac{1}{2}} \tag{4.113}$$

let us assign $G = d_{eq}^2$,

$$\mathcal{Y} = \int_0^{2\pi}\int_0^{\pi} \sqrt{G} \sin\theta d\theta d\phi = \int_0^{\pi} \sin\theta \left(\int_0^{2\pi} \sqrt{G} d\phi\right) d\theta \tag{4.114}$$

Applying the principle (4.113), we have

$$\int_0^{2\pi} \sqrt{G} d\phi = \left(\int_0^{2\pi} G d\phi\right)^{\frac{1}{2}} \left(\int_0^{2\pi} d\phi\right)^{\frac{1}{2}} \tag{4.115}$$

Then (4.114) becomes

$$\mathcal{Y} \leq \sqrt{2\pi} \int_0^{\pi} \sin\theta \left(\int_0^{2\pi} G d\phi\right)^{\frac{1}{2}} d\theta = \sqrt{2\pi} \int_0^{\pi} \sqrt{\sin\theta} \left(\int_0^{2\pi} G \sin\theta d\phi\right)^{\frac{1}{2}} d\theta \tag{4.116}$$

Bibliography

[Abou-Chakra et al.,08] A. Abou-Chakra Guery, F. Cormery, J.-F. Shao, D. Kondo, 2008. A micromechanical model of elasto-plastic and damage behavior of a cohesive geomaterial. Int. J. Solid. Struct., 45 (5), 1406–1429.

[Andra,05] Andra, 2005. Referentiel du site meuse-haute marne. Report.

[Barthélémy and Dormieux,03] J.F. Barthélémy, L. Dormieux, 2002. Détermination du critère de rupture macroscopique d'un milieu poreux par homogénéisation non linéairee. C. R. Mechanique, 331, 271–276.

[Benzerga and Besson 01] A.A. Benzerga, J.Besson, 2001. Plastic potentials for anisotropic porous solids. Eur. J. Mech. A/Solids., 20, 397–434.

[Cazacu and Stewart,09] O. Cazacu, J. B. Stewart, 2009. Plastic potentials for porous aggregates with the matrix exhibiting tension-compression asymmetry. Journal of the Mechanics and Physics of Solids, 57 : 325-341.

[Dormieux et al.,06b] L. Dormieux, D.Kondo, F-J. Ulm,, 2006. Microporomechanics, Wiley.

[Dormieux et al.,10] L. Dormieux, D. Kondo, 2010. An extension of gurson model incorporating interface stresses effects. International Journal of Engineering Science, 48(6), 575–581.

[Garajeu and Suquet,97] M. Garajeu, P. Suquet, 1997, Effective properties of porous ideally plastic or viscoplastic materials containing rigid particles. Journal of the Mechanics and Physics of Solids., 45(6), 873-902.

[Garajeu et al.,00] M. Garajeu, J.C. Michel, P. Suquet, 2000. A micromechanical approach of damage in viscoplastic materials by evolution in size, shape and distribution of voids, Comput. Methods Appl. Mech. Engrg., 183, 223–246.

[Gologanu et al.,93] M. Gologanu, J.-B. Leblond, J. Devaux, 1993. Approximate models for ductile metals containing non-spherical voids-case of axisymmetric prelate ellipsoidal cavities, J. Mech. Phys. Solids, 41(11), 1723–1754.

[Gologanu et al.,94] M. Gologanu, J.-B. Leblond, J. Devaux, 1994. Approximate models for ductile metals containing non-spherical voids-case of axisymmetric oblate ellipsoidal cavities, J. Engrg. Mater. Tech. 116, 290–297.

[Gologanu et al.,97] M. Gologanu, J.-B. Leblond, G. Perrin, J. Devaux, 1997. Recent extensions of Gurson's model for porous ductile metals, in: P. Suquet Ed. Continuum Micromechanics, Springer-Verlag, Berlin/New York, 61–130.

[Guo et al.,08] T.F. Guo, J. Faleskog, C.F. Shih., 2008. Continuum modeling of a porous solid with pressure-sensitive dilatant matrix., J. Mech. Phys. Solids, 56, 2188–2212.

[Gurson,77] A.L. Gurson, 1977. Continuum theory of ductile rupture by void nucleation and growth: Part I–Yield criterion and flow rules for porous ductile media, J. Engrg. Mat. Technol. 99, 2–15.

[Jeong and Pan,95] H.-Y. Jeong, J.Pan., 1995. A macroscopic constitutive law for porous solids with pressure-sensitive matrices and its implications to plastic flow localization., International Journal of Solids and Structures, 32, 3669–3691.

[Jeong,02] H.-Y. Jeong, 2002. A new yield function and a hydrostatic stress-controlled void nucleation model for porous solids with pressure-sensitive matrices, International Journal of Solids and Structures, 39, 1385–1403.

[Keralavarma and Benzergar,10] S.M. Keralavarma, A. A. Benzerga, 2010. A constitutive model for plastically anisotropic solids with non-spherical voids. Journal of the Mechanics and Physics of Solids, 58 : 874-901.

[Leblond et al.,94] J.-B. Leblond, G. Perrin, P. Suquet., 1994. Exact results and approximate models for porous viscoplastic solids. International Journal of Plasticity, 10(3):213–235.

[Lee and Oung,00] J. H. Lee, J. Oung, 2000. Yield Functions and Flow Rules for Porous Pressure-Dependent Strain-Hardening Polymeric Materials., Journal Applied Mechanics., 67, 288–297.

[Liao et al.,97] K. Liao, J. Pan, S. Tang, 1997. Approximate yield criteria for anisotropic porous ductile sheet metals. Mech. Mater., 26, 213–226.

[Maghous et al.,09] S. Maghous, L. Dormieux, J. Barthelemy, 2009. Micromechanical approach to the strength properties of frictional geomaterials. European Journal of Mechanics A/Solids., 28(1), 179–188.

[Michel and Suquet,92] J.-C. Michel, P. Suquet, 1992, The constitutive law of nonlinear viscous and porous materials. Journal of the Mechanics and Physics of Solids., 40, 783-812.

[Monchiet et al.,07] V. Monchiet, E. Charkaluk, D. Kondo, 2007. An improvement of Gurson-type models of porous materials by using Eshelby-like trial velocity fields. Comptes Rendus Mecanique., 335(1), Pages 32–41

[Monchiet et al.,08] V.Monchiet, O.Cazacu, E.Charkaluk, D.Kondo, 2008. Macroscopic yield criteria for plastic anisotropic materials containing spheroidal voids. International Journal of Plasticity, 24, 1158–1189

[Monchiet et al.,11] V. Monchiet, E. Charkaluk, D. Kondo, 2011. A Micromechanics-based modification of the Gurson criterion by using Eshelby-like velocity fields. European J. Mech. A/solids. 30, 940-949.

[PonteCastaneda,91] P.Ponte Castaneda, 1991. The effective mechanical properties of non-linear isotropic composites. J. Mech. Phys. Solids, 39, 45–71.

[Robinet,12] J-C. Robinet, P. Sardini, D. Coelho, J-C. Parneix, D. Pret, S. Sammartino, E. Boller and S. Altmann., 2012. Effects of mineral distribution at mesoscopic scale on solute diffusion in a clay-rich rock: Example of the Callovo-Oxfordian mudstone (Bure, France). Water Resources Research, 48, W05554, doi:10.1029/2011WR011352.

[Salencon,90] J. Salencon, 1990. An introduction to the yield theory and its applications to soil mechanics. European Journal of Mechanics A/Solids, 9(5),477–500.

[Shen,11] W.Q. Shen, 2011. Modelisations micro-macro du comportementmecanique des materiaux poreux ductiles: application a l'argilite du Callovo-Oxfordien, Phd. thesis, Universite de Lille 1, France.

[Shen et al.,12] W.Q. Shen, J.F. Shao, D. Kondo, B. Gatmiri., 2012. A micro-macro model for clayey rocks with a plastic compressible porous matrix, International Journal of Plasticity, 36, 64–85

[Shen et al.,12b] W.Q. Shen, J-F. Shao, L. Dormieux, D. Kondo, 2012. Approximate criteria for ductile porous materials having a Green type matrix: Application to double porous media, Comput Mater Sci., 62, 189–194.

[Thore et al.,09] Ph. Thoré, F. Pastor, J. Pastor, D. Kondo, 2009. Closed form solutions for the hollow sphere model with Coulomb and Drucker-Prager materials under isotropic loadings, C. R. Mécanique, Acad. Sc. Paris, 337, 260–267.

[Thore et al.,11] Ph. Thoré, F. Pastor, J. Pastor, 2011. Hollow sphere models, conic programming and third stress invariant. European J. Mech. A/solids. 30, 63-71.

[Trillat et al.,06] M. Trillat, J. Pastor, P. Thoré., 2006. Limit analysis and conic programming: 'porous Drucker-Prager' material and Gurson's model., C.R. Mécanique. 334, 599–604.

[Vincent et al.,09] P.-G. Vincent, Y. Monerie, P. Suquet, 2009. Porous materials with two populations of voids under internal pressure : I. instantaneous constitutive relations. International Journal of Solids and Structures, 46, 480–506.

Conclusion

Conclusion

L'objectif de ce travail est de mettre en place des outils de modélisation micromécanique permettant d'étudier le comportement de l'argilite du Callovo-Oxfordien. Le matériau était abordé à trois échelles d'espace distinctes. L'échelle microscopique révèle l'hétérogénéité de la phase argileuse de l'argilite. A L'échelle microscopique, il est décrit comme un polycristal poreux. Le cristal élémentaire est l'agrégat d'argile structuré (grain feuilleté). Le volume complémentaire des cristaux de la phase argileuse est l'espace poreux observé sous forme de micropores. Ces micropores constituent le volume principal de pores de l'argilite et affectent de façon sensible le comportement de l'argilite. A l'échelle mésoscopique, le matériau se présente comme un composite composé une matrice argileuse homogène et des inclusions (quartz, calcite etc.). L'homogénéisation de ce composite débouche sur la caractérisation de l'argilite à l'échelle macroscopique.

Au point de départ de la thèse, nous avons proposé une description des propriétés élastiques isotropes transverses de la phase argileuse sur laquelle s'est appuyé le model morphologique sythetisé comme un polycristal poreux (cristaux + pores). En revisitant le problème d'Eshelby généralisé, l'interaction mécanique entre des cristaux a été prise en compte en supposant un motif de grain feuilleté entouré par une interface. La mise en place d'un schéma auto-cohérant généralisé dans le cadre d'une approche incrémentale a permis d'obtenir des prédictions numériques du comportement de la phase argileuse.

Pour comprendre les effets d'interface sur les propriétés mécaniques effectives des géomatériaux, des interfaces de type Mohr-Coulomb cohésif ont été considérés. Sur cette base, on a proposé tout d'abord un modèle poro-élastique pour les matériaux granulaires saturés avec effets d'interface imparfaite. Ensuite, sur la base de ce modèle poroélastique et s'appuyant sur le cadre de l'homogénéisation nonlinéaire, nous avons pu quantifier le rôle joué par les interfaces imparfiates de type Mohr-Coulomb cohésif entre des grains rigides sur le critère de résistance macroscopique d'un milieu granulaire.

Enfin, nous avons proposé un modèle complet pour la prédiction de la résistance de l'argilite du Callovo-Oxfordien sous l'hypothèse que la matrice argileuse est un matériau poreux avec la phase solide décrite par un critère Drucker-Prager parfaitement plastique. Il importante de noter que le mécanisme de rupture explorée inclut la possibilité d'une concentration de déformation à l'interface de noyau rigide -matrice qui peut être décrite mathématiquement à l'aide d'une discontinuité de vitesse. Ce modèle a été analysé en détail et ses prédictions apparaissent tout à fait probantes.

Perspectives

Les perspectives de ce travail sont diverses.

> Pour suite du developpement du modèle de matériau polycristallin en vue du parcours complet d'échelles requis pour l'argilite du Callovo-Oxfordien. Il conviendra de realiser la mise en oeuvre de ce modèle et de le confronter à son homologue qui sera issu des résultats du chapitre 4.
>
> Investigation des comportements couplés hydromécaniques prenant en compte la microstructure multiéchelle de l'argilite.
>
> A moyen terme, il sera opportun d'étudier la réponse différée de l'argilite en adjoignant au modèle les mécanismes de viscosité dans la matrice argileuse.

Résumé

Ce travail porte sur la mise en place des outils de modélisation micromécanique permettant d'étudier le comportement de l'argilite du Callovo-Oxfordien. Ce géomatériau poreux est modélisé comme un milieu hétérogène à trois échelles d'espace distinctes. L'échelle microscopique révèle l'hétérogénéité de la phase argileuse sur laquelle s'est appuyé le modèle morphologique synthétisé comme un polycristal poreux. Des prédictions numériques du comportement élasto-plastique et isotrope transverse de la phase d'argile tenant compte d'interactions mécaniques entre des cristaux sont effectuées à l'aide d'une approche incrémentale de Hill. Ensuite, un modèle poroélastique pour matériaux granulaires saturés avec effets d'interface imparfaite est proposé. Sur la base de ce modèle poroélastique et s'appuyant sur le cadre de l'homogénéisation non linéaire, on met en évidence l'impact des interfaces imparfaites de type Mohr-Coulomb cohésif sur le critère de résistance de géomatériaux granulaires. Enfin, nous avons propose un modèle complet pour la prédiction de la résistance de l'argilite du Callovo-Oxfordien sous l'hypothèse que la matrice argileuse est un matériau poreux avec la phase solide décrite par un critère Drucker-Prager parfaitement plastique. Il est important de noter que le mécanisme de rupture exploré inclut la possibilité d'une concentration de déformation à l'interface de noyau (rigide)-matrice. Ce modèle est analysé en détail et ses prédictions apparaissent tout à fait probantes.

Mot-clés**:** *micromécanique, homogénéisation, non linéaire, multi-échelles, calcul à la rupture, résistance, poroélasticité, Mohr-Coulomb, Drucker-Prager, interface, polycristal, milieu poreux,*

Abstract

This work focuses on the development of micromechanical modeling tools to study the behavior of the Callovo-Oxfordian argillite. This geomaterial is modeled as a porous heterogeneous medium at three distinct spatial scales. The microscopic scale reveals the heterogeneity of the clay phase on which the morphological model synthesized as a porous polycrystal was based. Numerical predictions of the elastoplastic and transversely isotropic clay phase considering mechanical interactions between the crystals are performed by using an incremental approach. Then, a poroelastic model for saturated granular materials with imperfect interface effects is proposed. On the basis of this poroelastic model and the nonlinear homogenization, we showcase the impact of the cohesive Mohr-Coulomb imperfect interfaces on the strength criterion of granular geomaterials. Finally, we propose a complete model for the prediction of the strength of Callovo-Oxfordian argillite under the assumption that the clay matrix is a porous material with the solid phase described by a perfectly plastic Drucker-Prager criterion. It is important to note that the explored failure mechanism includes the possibility of a strain concentration at the (rigid) inclusion-matrix interface. This model is analyzed in detail and its predictions appear quite convincing.

Keywords: *micromechanics, homogenization, nonlinear, multi-scale, limit analysis, strength, poroelasticity, Mohr-Coulomb, Drucker-Prager, interface, polycrystal, porous medium*